Predicting Infrared Luminosity Functions of High-Redshift Galaxies with 3D Radiative Transfer Calculations

Mana Ito, Hidenobu Yajima, Kenta Soga
(University of Tsukuba)

December 3, 2025

Outline

1. **Introduction**
2. Method
3. Results
4. Discussion
5. Summary

Universal evolution and first galaxy

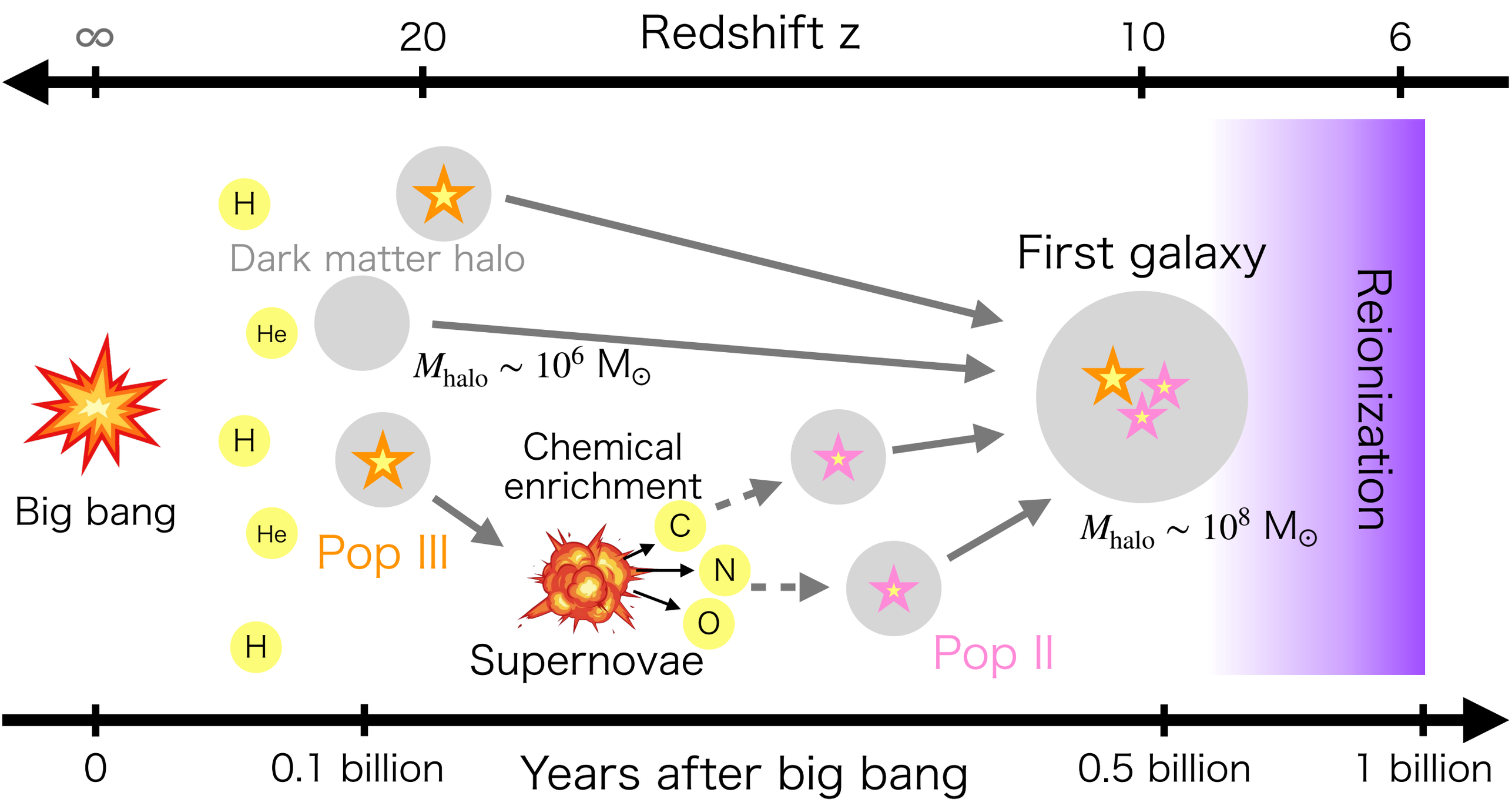

Diversity of first galaxies

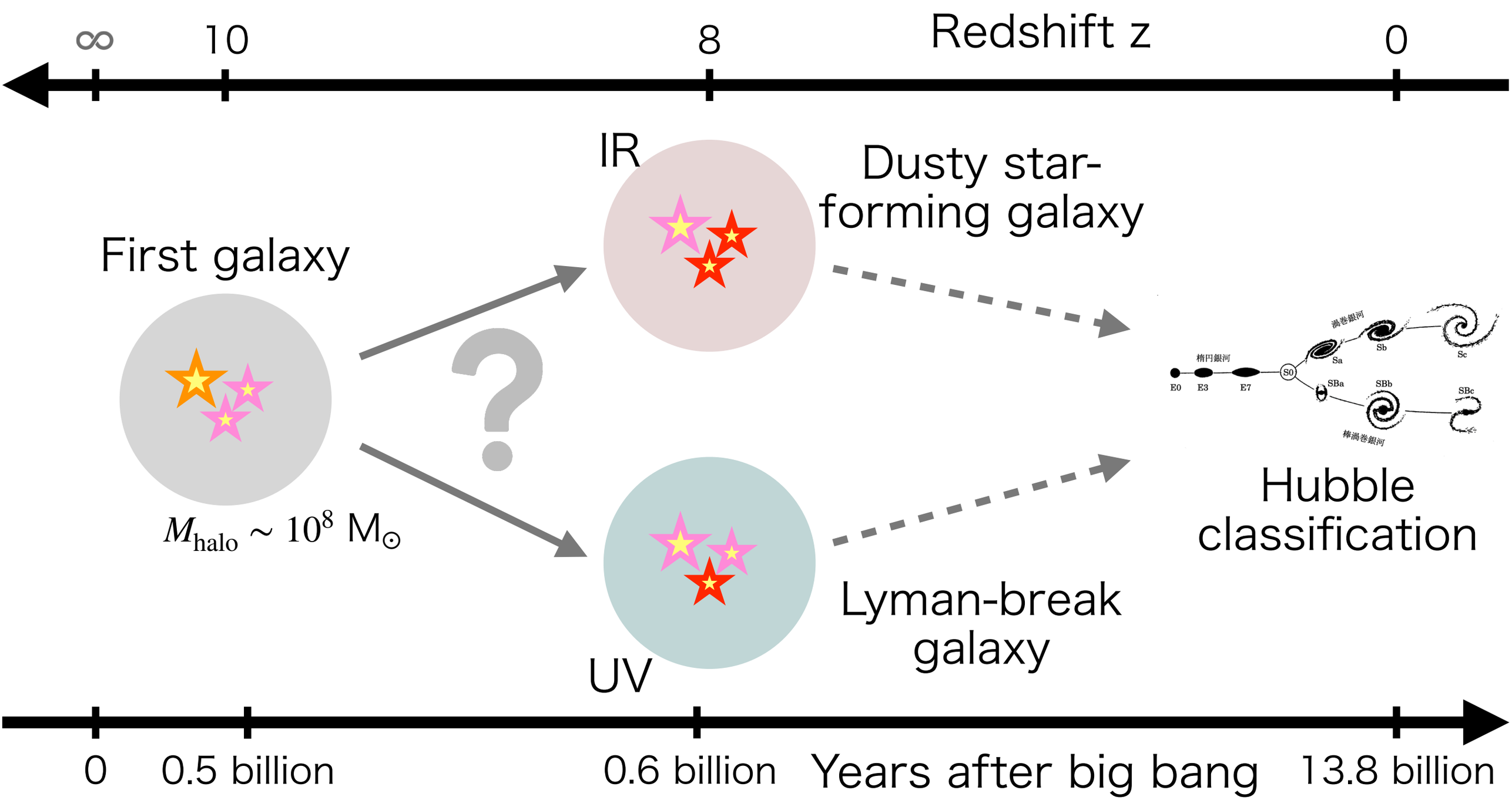

Motivation and Objective

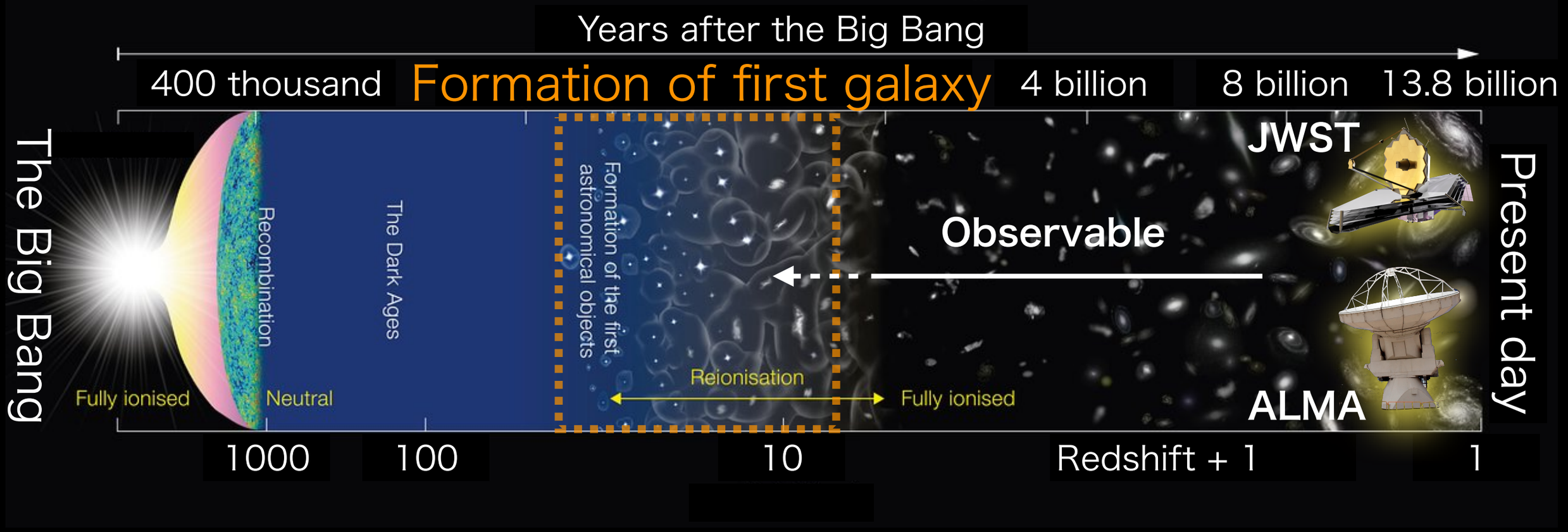

Motivation and Objective

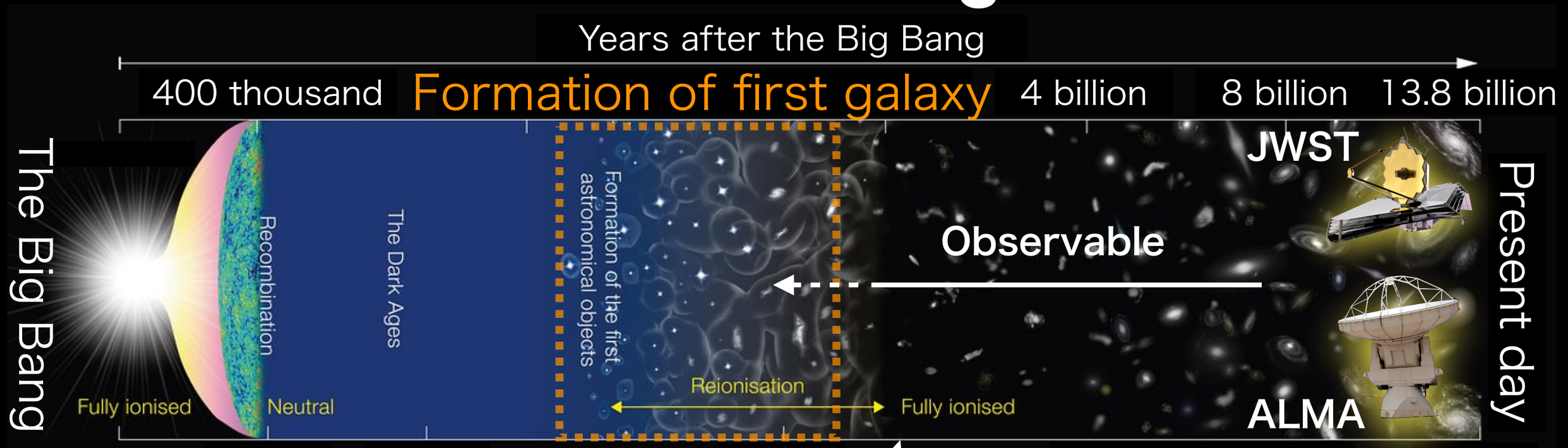

ALMA & JWST's observation ($z = 8.3$)

Harshan et al. (2024)

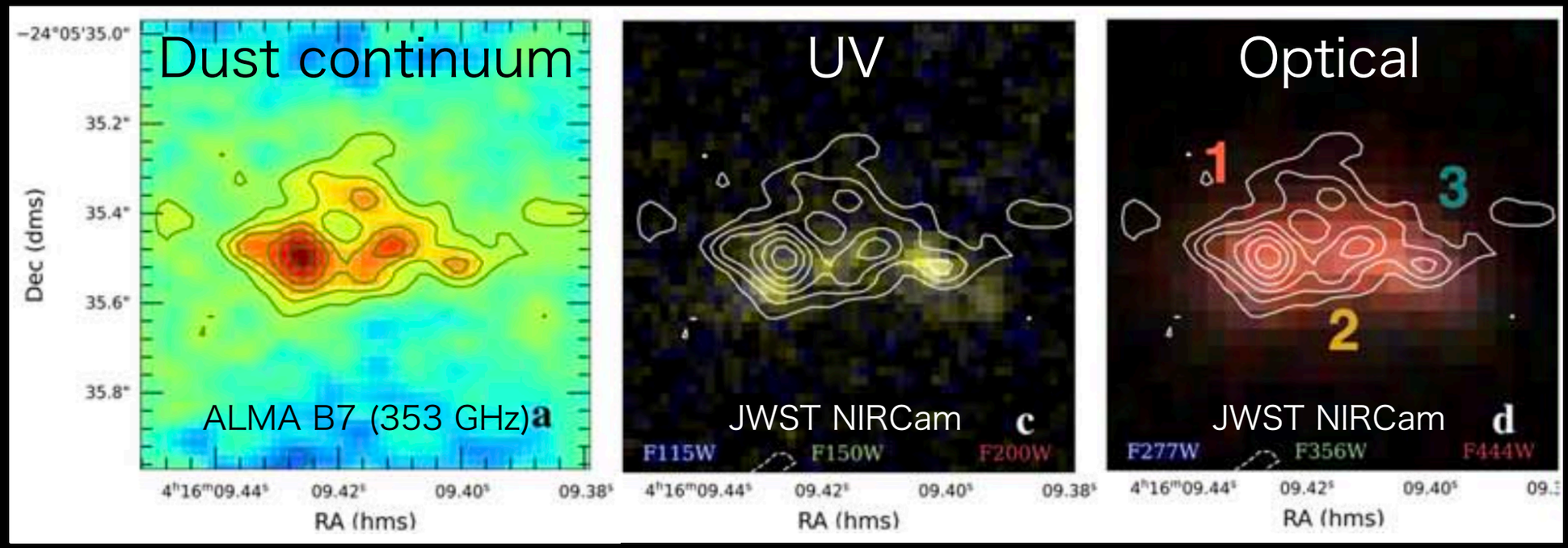

Motivation and Objective

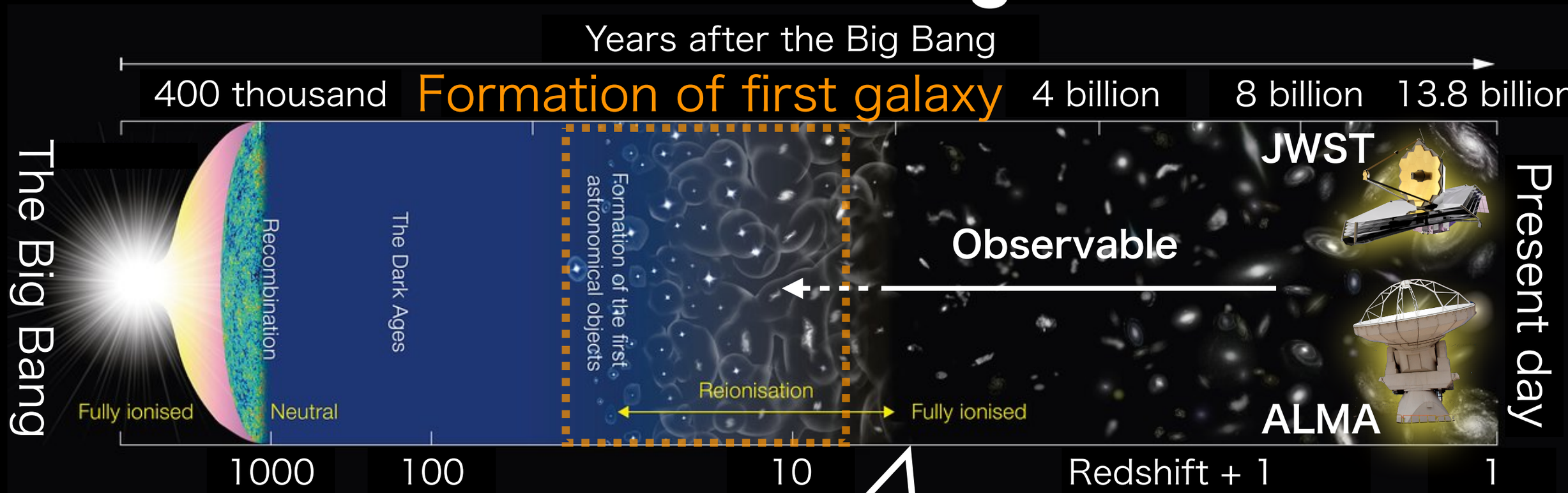

ALMA & JWST's observation ($z = 8.3$)

Harshan et al. (2024)

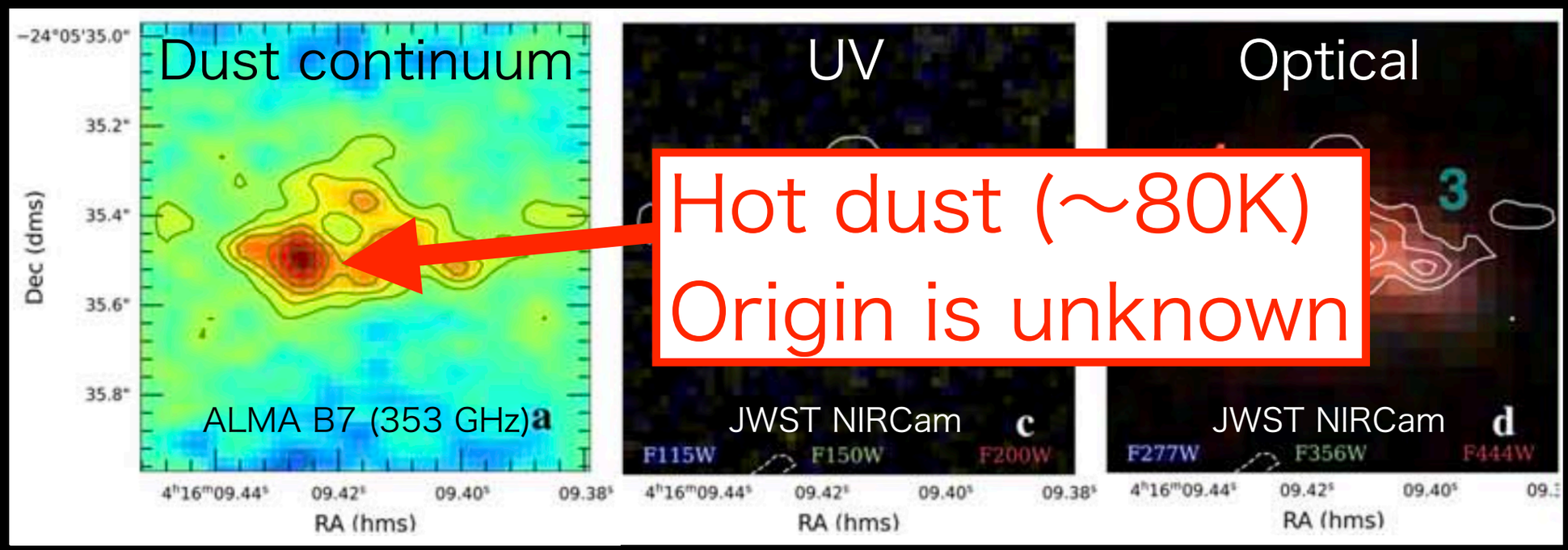

Motivation and Objective

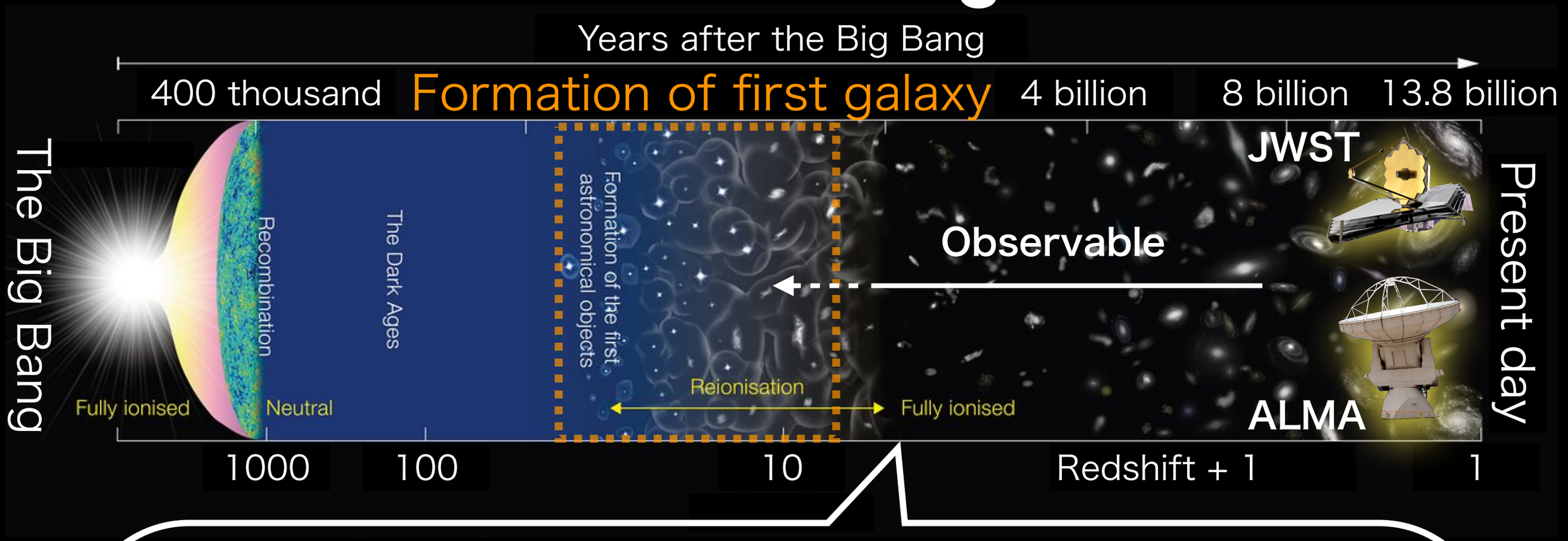

ALMA & JWST's observation ($z = 8.3$) Harshan et al. (2024)

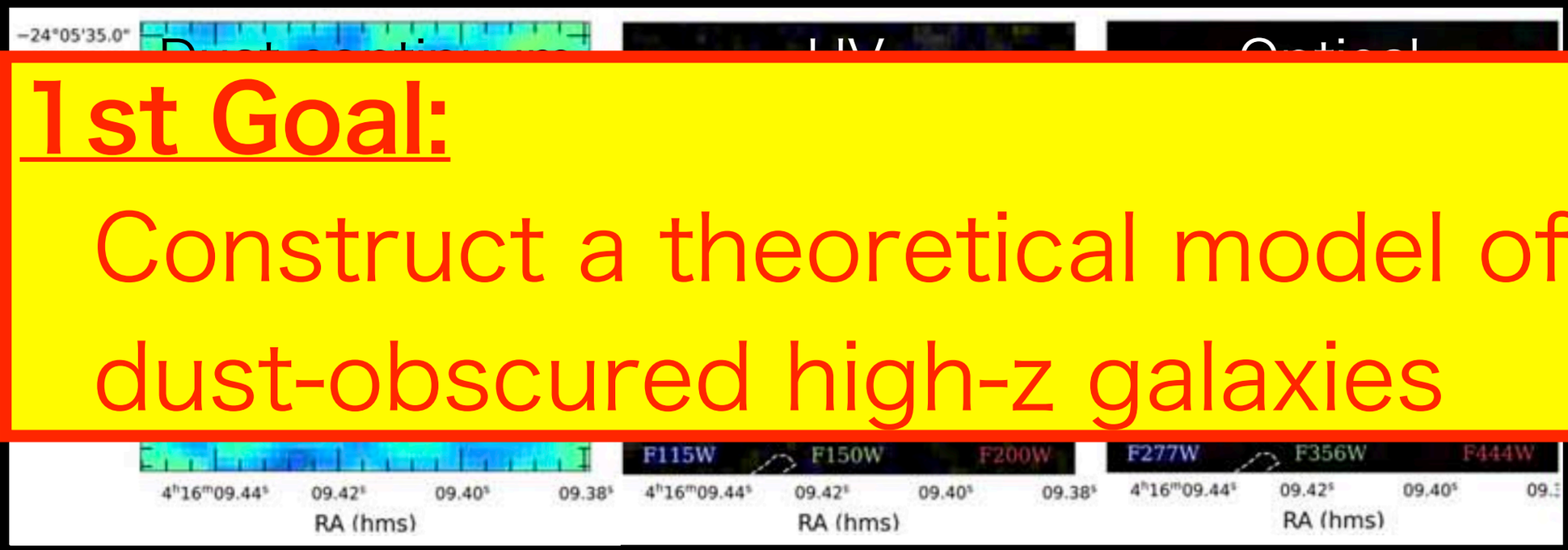

1st Goal:

Construct a theoretical model of dust-obscured high-z galaxies

Motivation and Objective

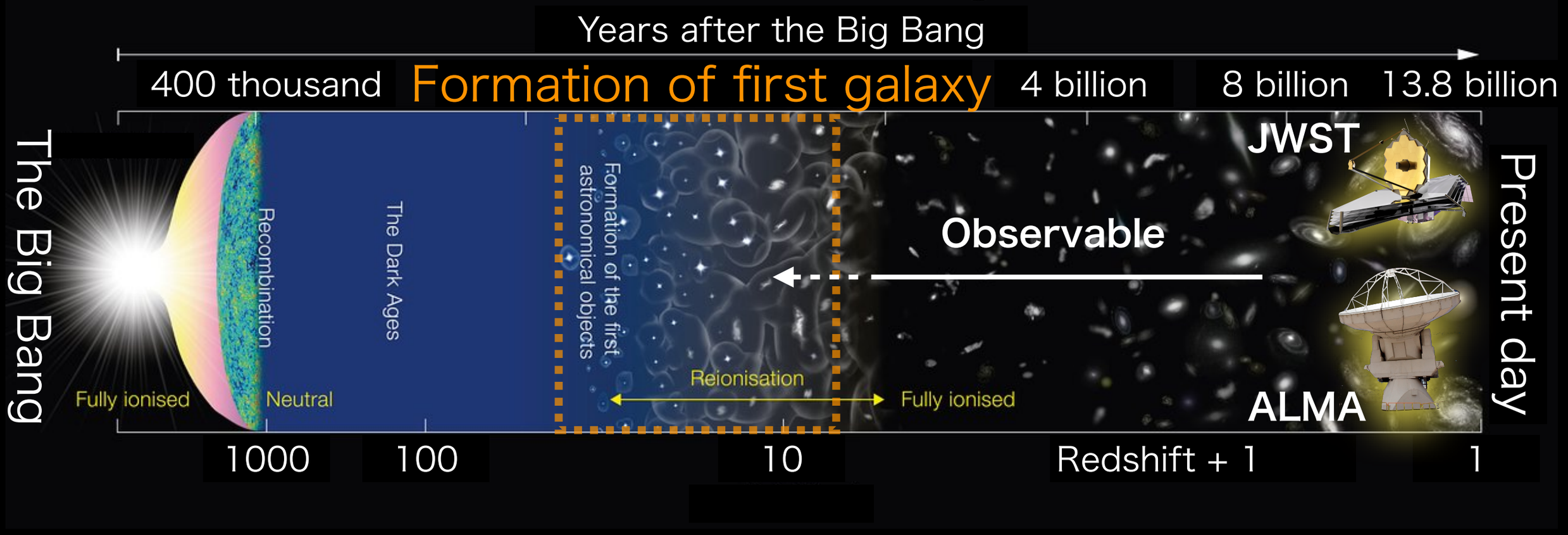

Antarctica 12-m THz Telescope (ATT12)

- Observing frequencies：200 GHz - 1.5 THz
- Field of view：～1°
- Survey observations covering the entire southern sky, approximately 10,000 square degrees
- Scheduled for operation from 2033

Motivation and Objective

Antarctica 12-m THz Telescope (ATT12)

- Observing frequency: 300 GHz – 1.5 THz
- Scheduled for operation from 2023

2nd Goal:

How far into the universe can the ATT12 observe?

Outline

1. Introduction
2. **Method**
3. Results
4. Discussion
5. Summary

Calculation Method

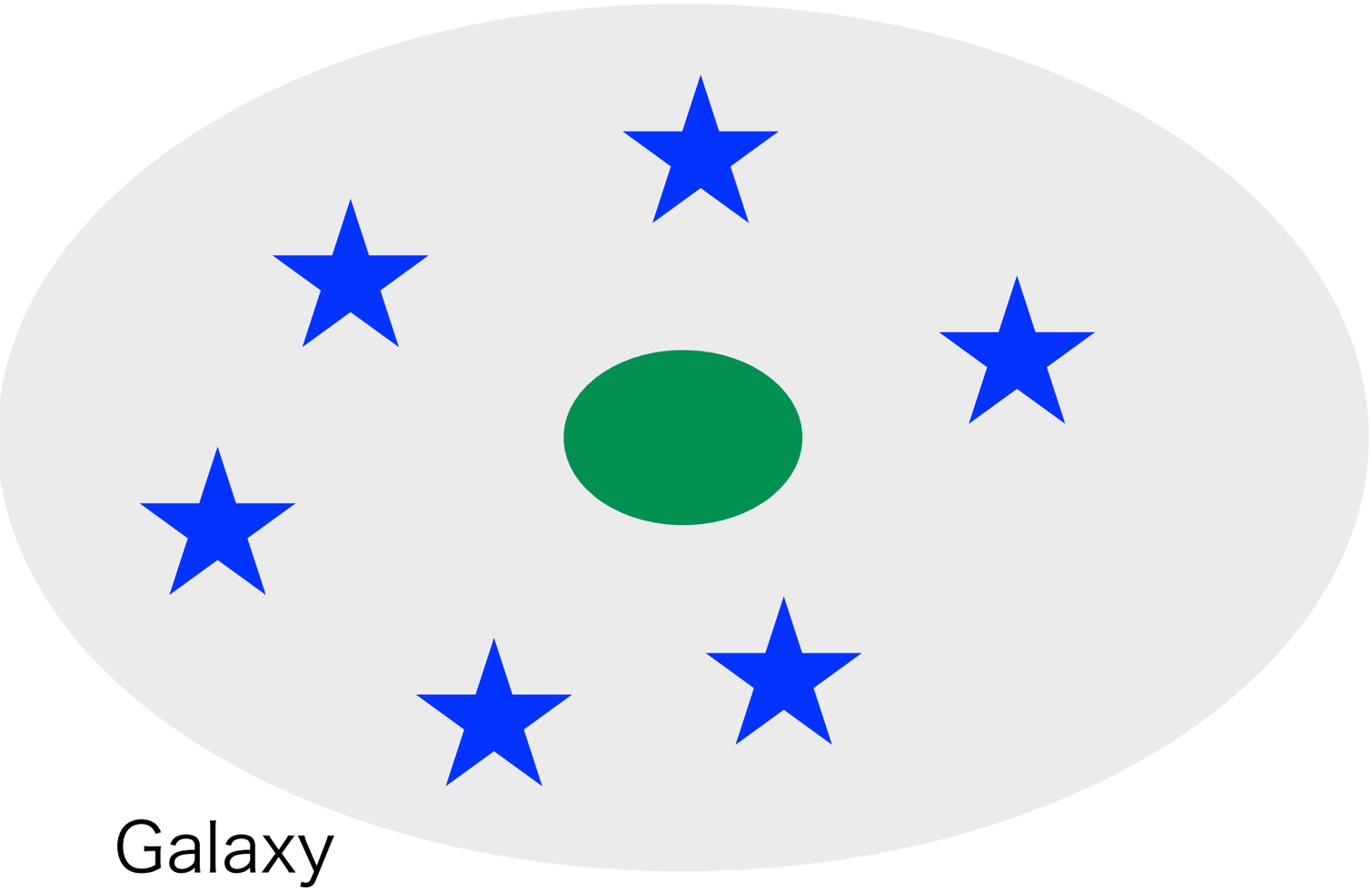

Galaxy

Calculation Method

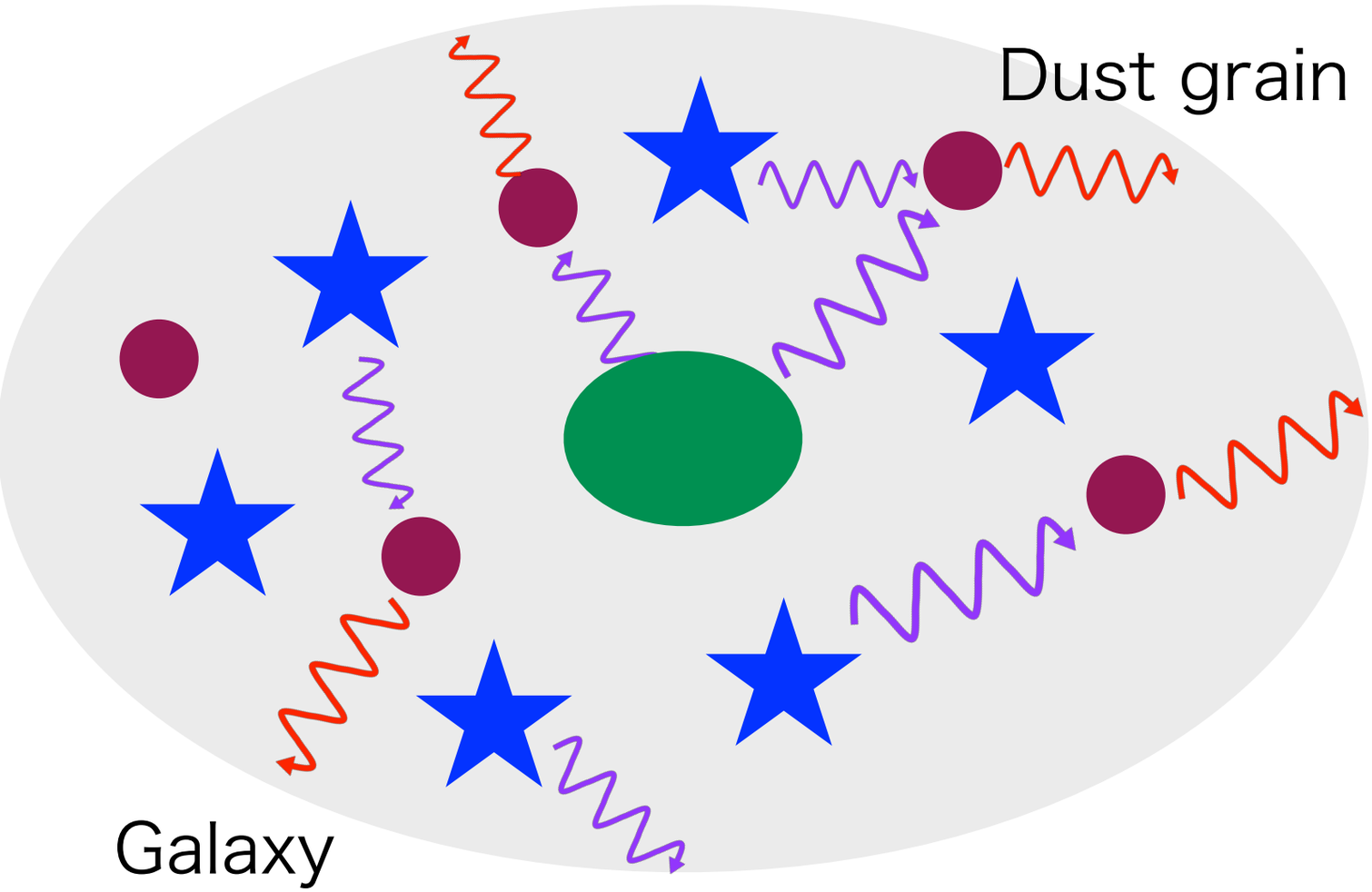

AGN

Stars

Radiation from stars and AGN

Radiation from dust grain

Calculation Method

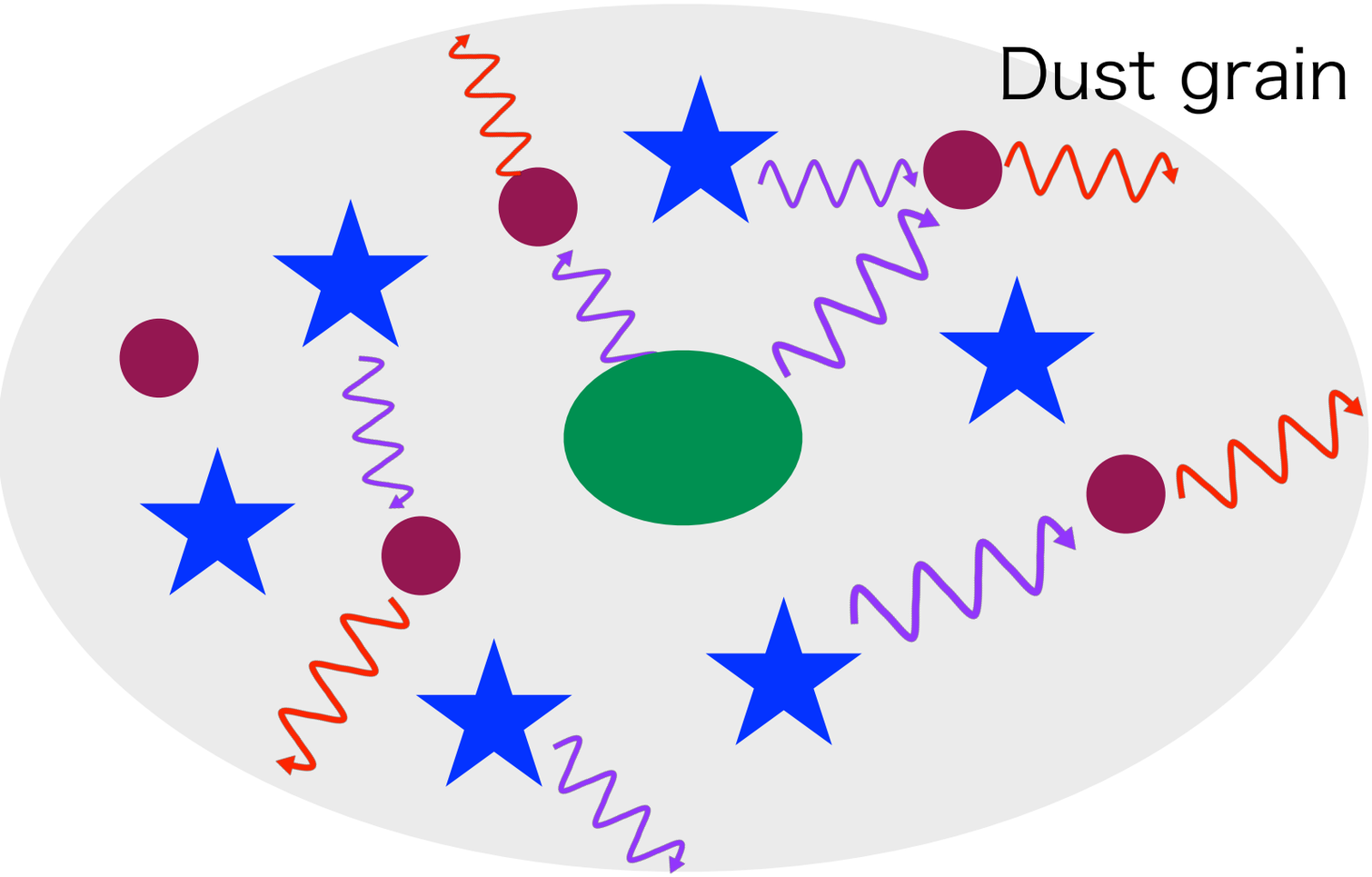

How does the surface of the galaxy appear in infrared?

<u>INPUT</u>: Forever22

AGN

Stars

Radiation from stars and AGN

properties of gas

<u>Radiative transfer</u>: ART2

Radiation from stars and AGN

Radiation from dust grain

Input: FOREVER22

"FORmation and EVolution of galaxies in Extremely overdense Regions motivated by SSA22" (Yajima et al. 2022)

- A large-scale cosmological hydrodynamic simulation
- Proto-Cluster Region: $V = (28.6\ \mathrm{cMpc})^3$, $m_{\mathrm{SPH}} = 4.1 \times 10^6\ \mathrm{M}_\odot$

STEP1: Run a DM-only N-body simulation in the parent box $V = (714.2\ \mathrm{cMpc})^3$ from $z_{\mathrm{start}} = 100$ to $z_{\mathrm{end}} = 2$

STEP2: Choose the top 10 most massive halos at $z_{\mathrm{end}} = 2$

STEP3: For each selected halo, perform a zoom-in hydrodynamic simulation in $V = (28.6\ \mathrm{cMpc})^3$ centered on the halo, using a modified SPH code based on GADGET-3 (Springel 2005), evolving from $z_{\mathrm{start}} = 100$ to $z_{\mathrm{end}} = 2$

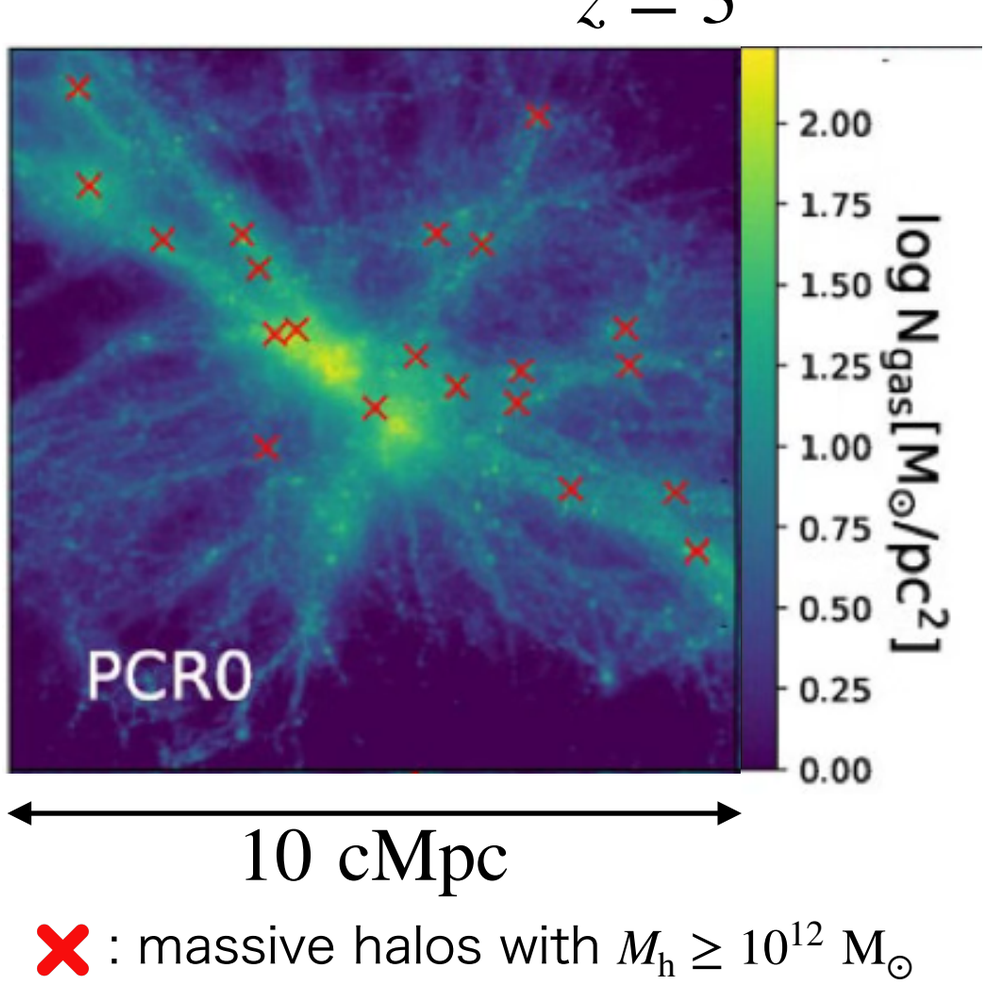

✖ : massive halos with $M_{\mathrm{h}} \geq 10^{12}\ \mathrm{M}_\odot$

Code: ART2

"All-wavelength Radiative Transfer with Adaptive Refinement Tree" (Yajima et al. 2012, Li et al. 2008)

photon packet: equal energy, monochromatic, same direction

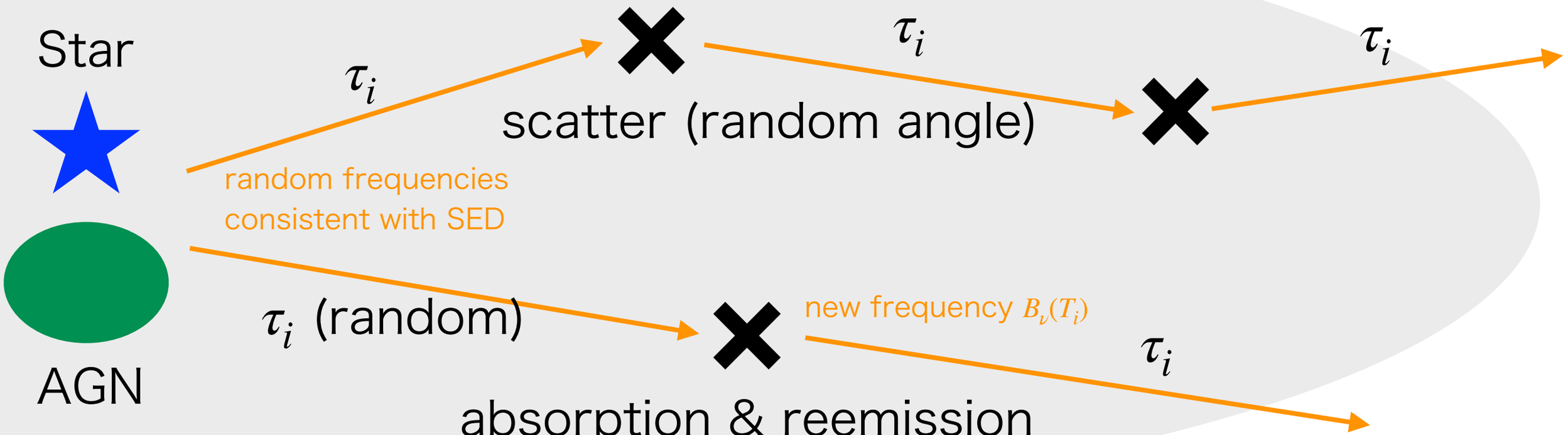

$$\sigma T_i^4 = \frac{N_i L}{4 N_\gamma \kappa_{\rm P}(T_i) m_i}$$

N_i : number of photon packets absorbed by i th grid cell

N_γ : total number of photon packet

L : total source luminosity

T_i : temperature

$\kappa_{\rm P}(T_i)$: Planck mean opacity

m_i : dust mass in the cell

Outline

1. Introduction
2. Method
3. **Results**
4. Discussion
5. Summary

Spectral Energy Distribution

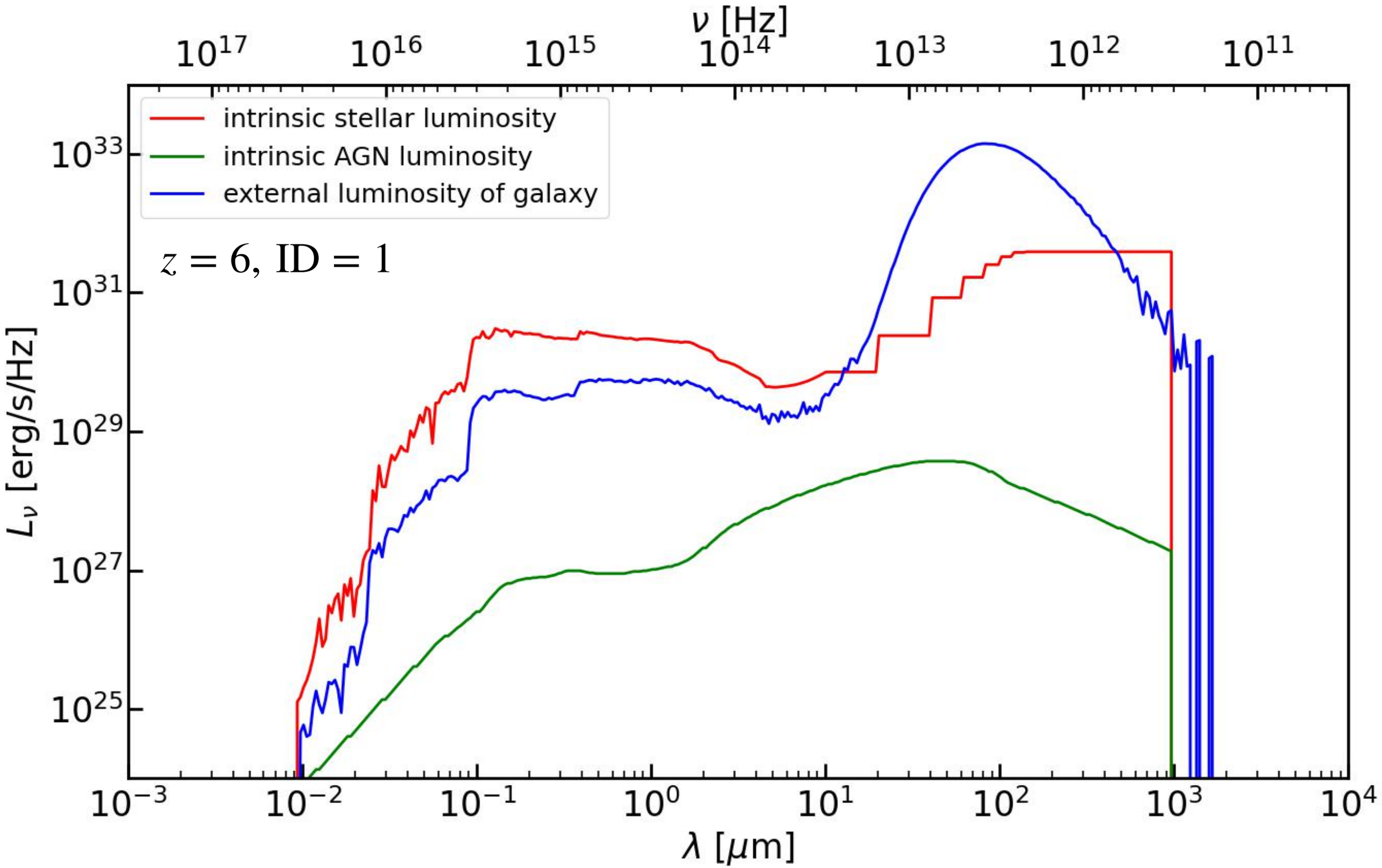

Spectral Energy Distribution

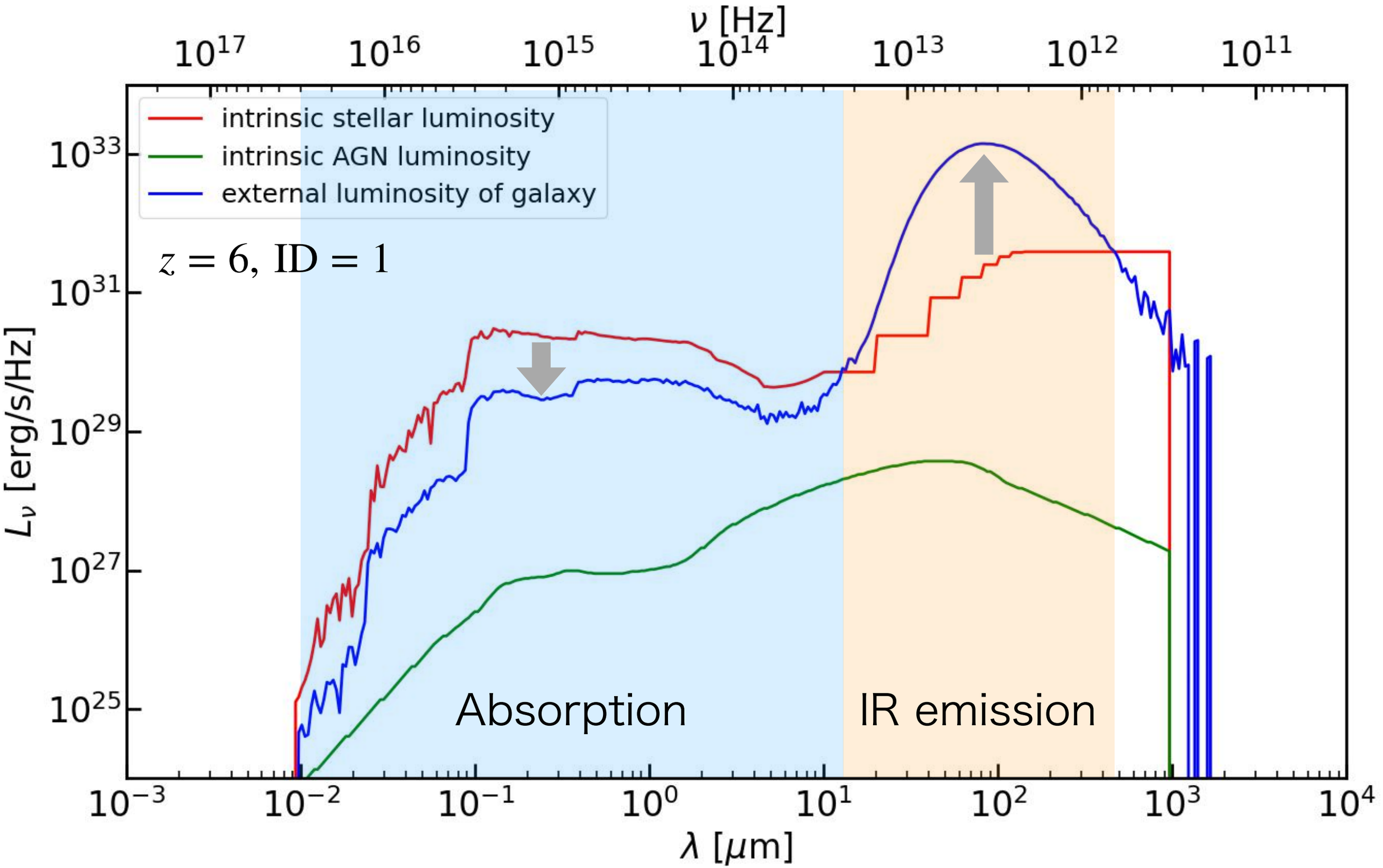

Spectral Energy Distribution

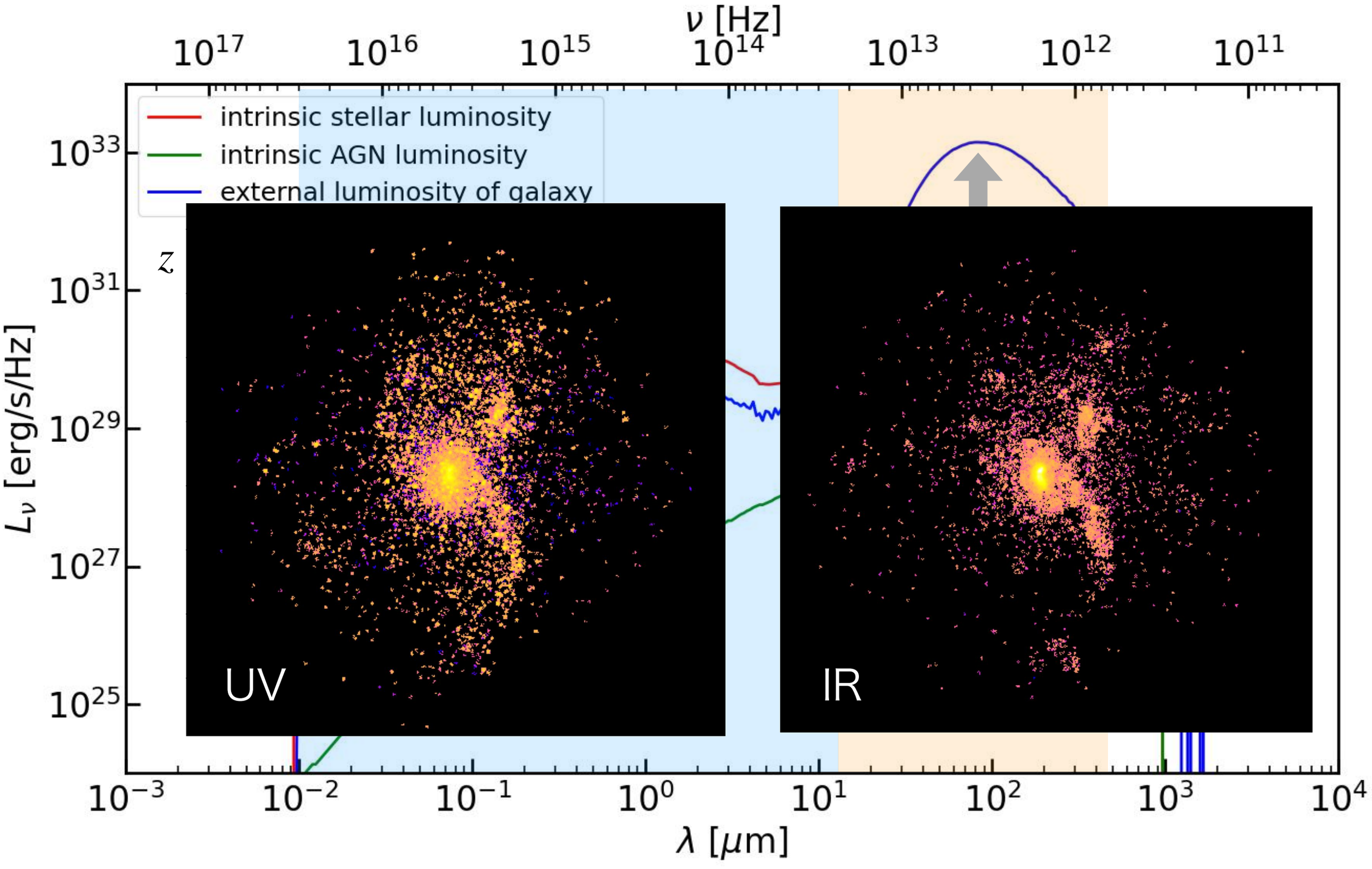

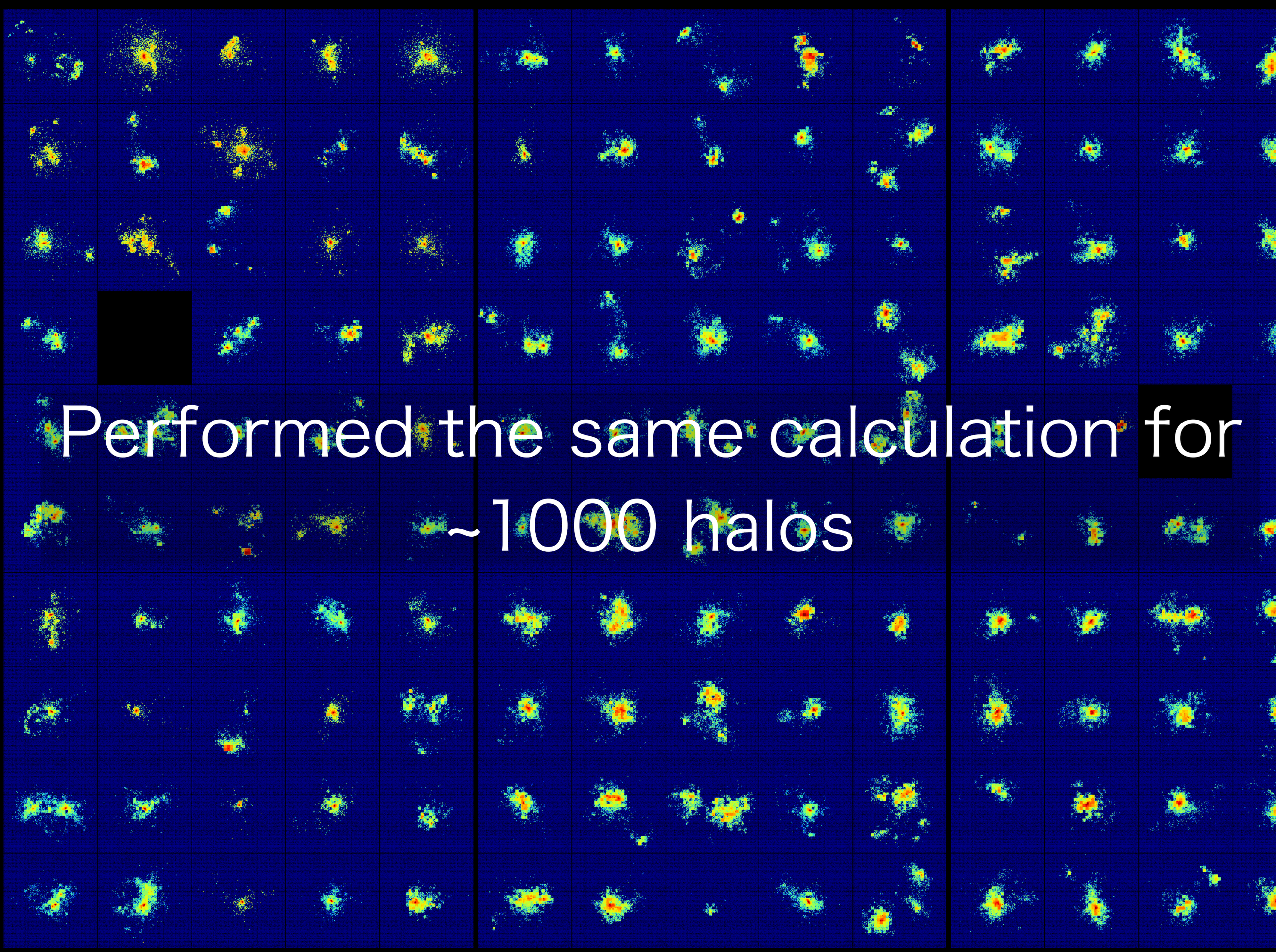
Performed the same calculation for
~1000 halos

Halo Mass v.s. IR Luminosity

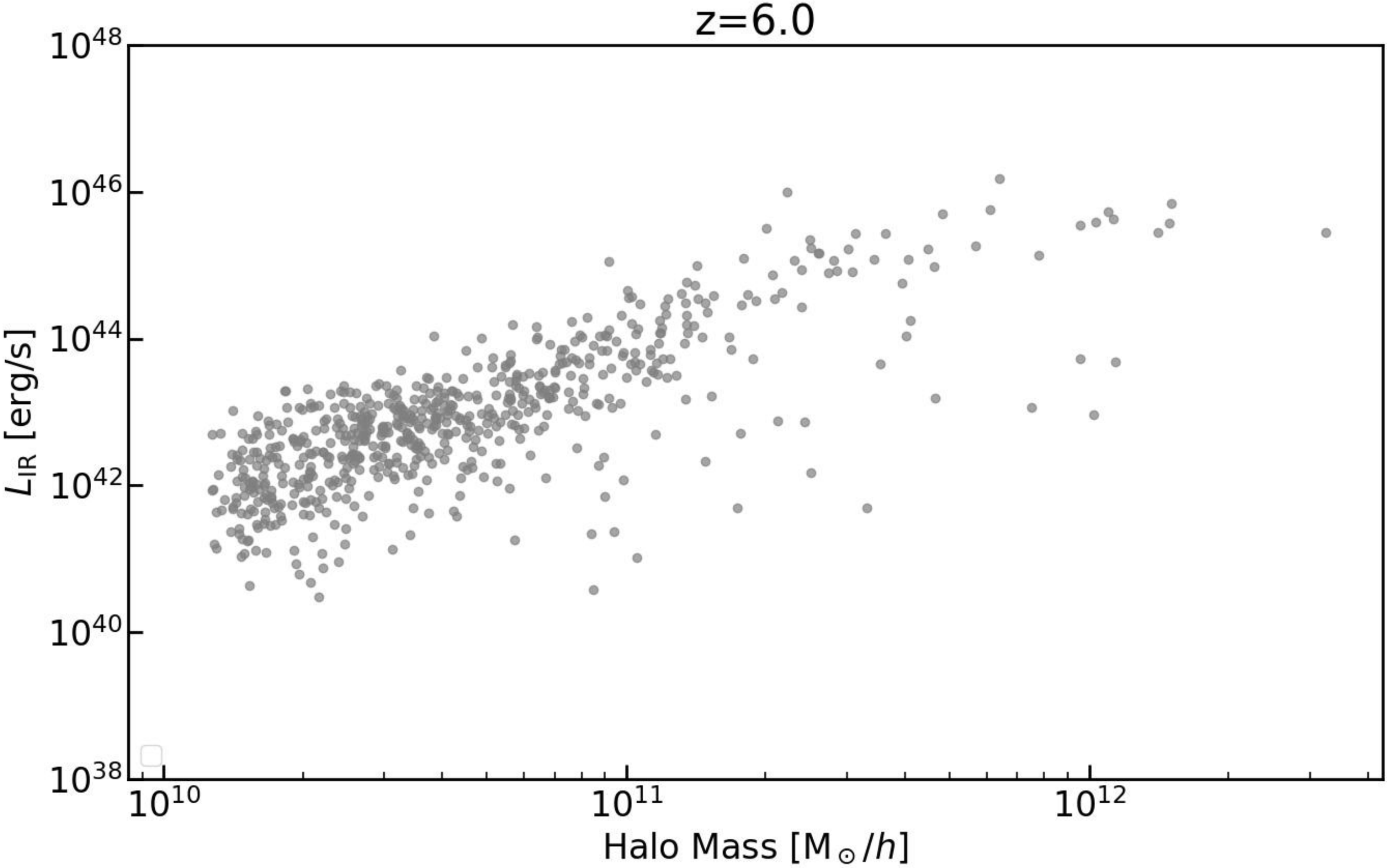

Halo Mass v.s. IR Luminosity

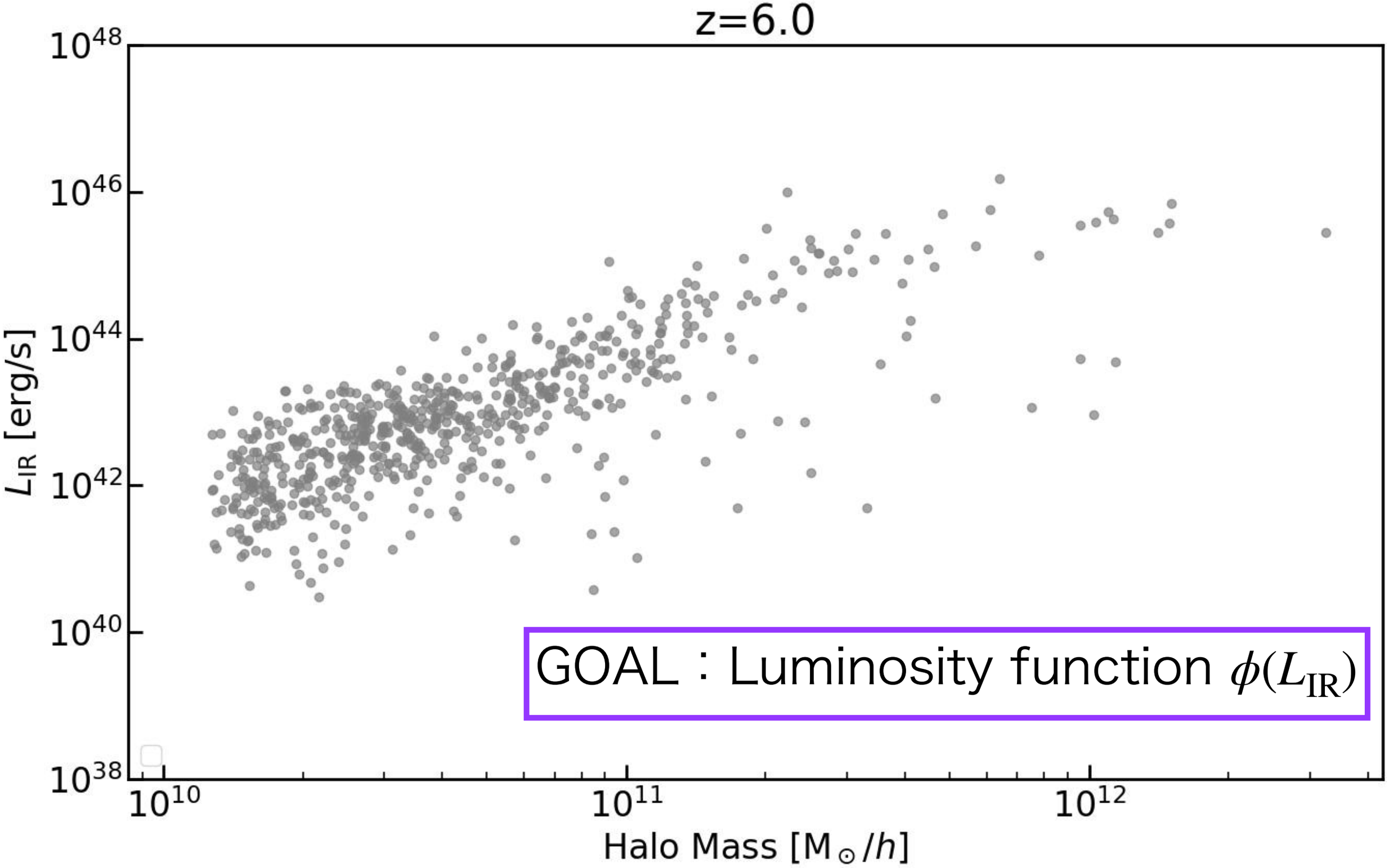

Halo Mass v.s. IR Luminosity

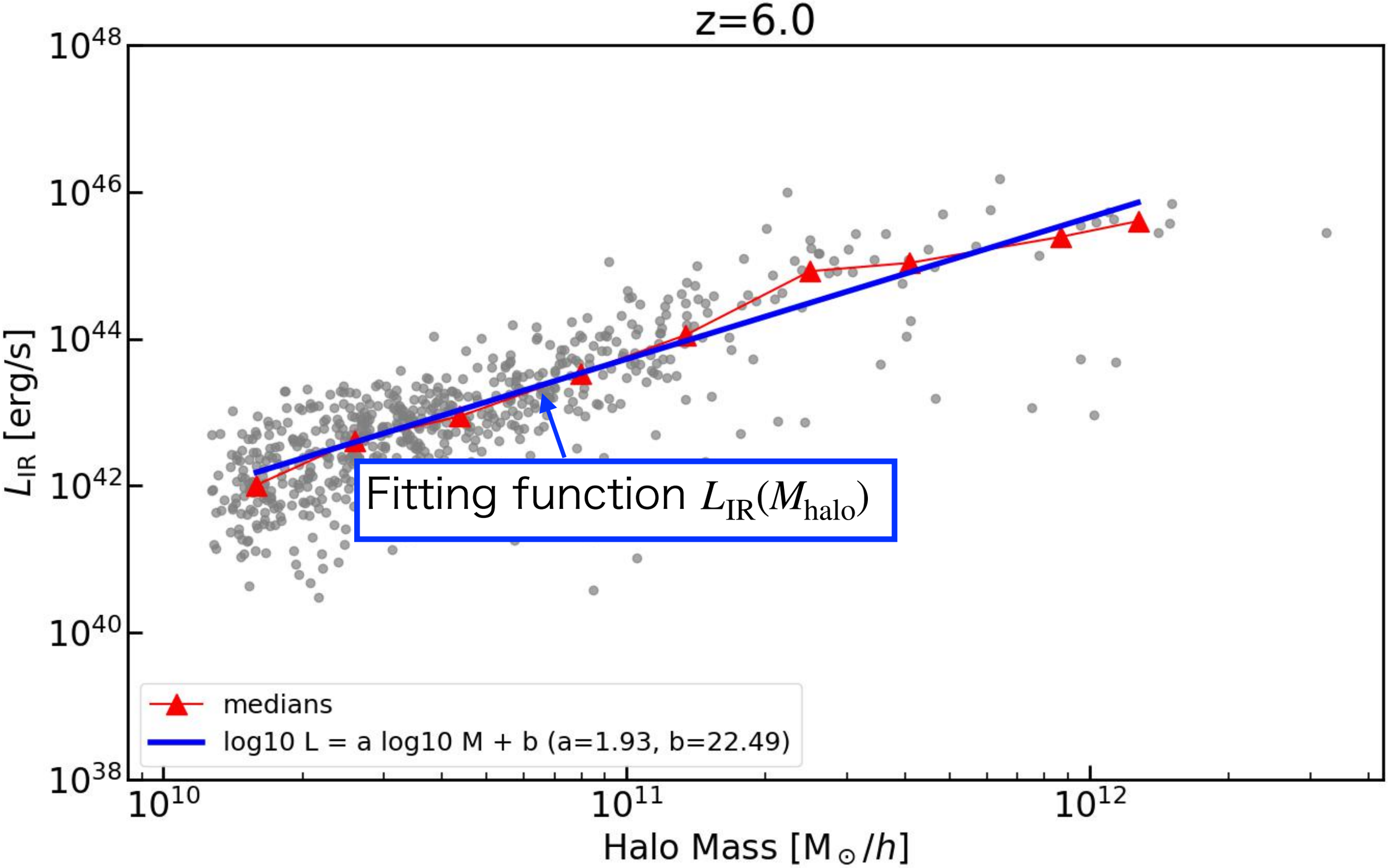

Halo Mass v.s. IR Luminosity

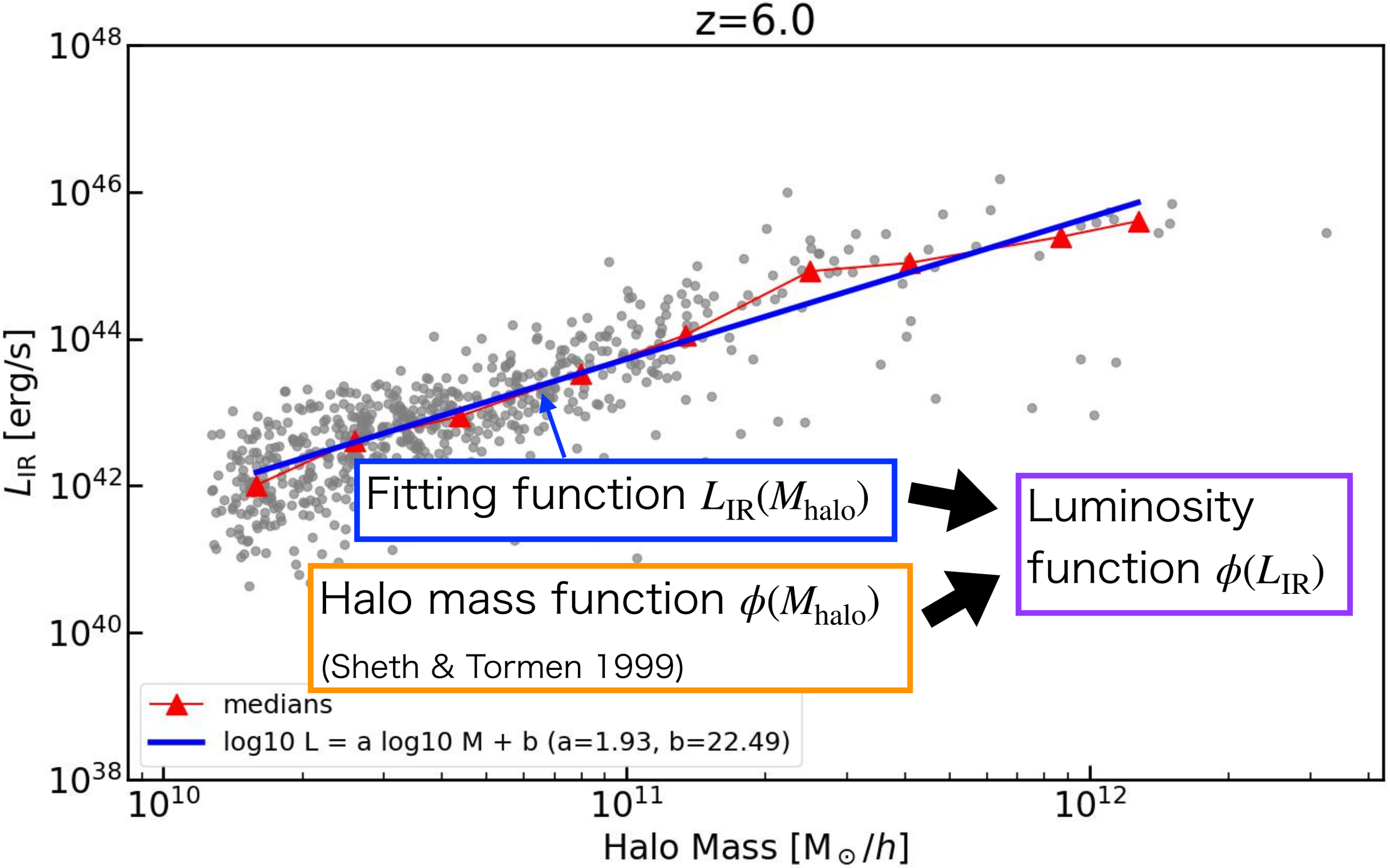

Luminosity Function

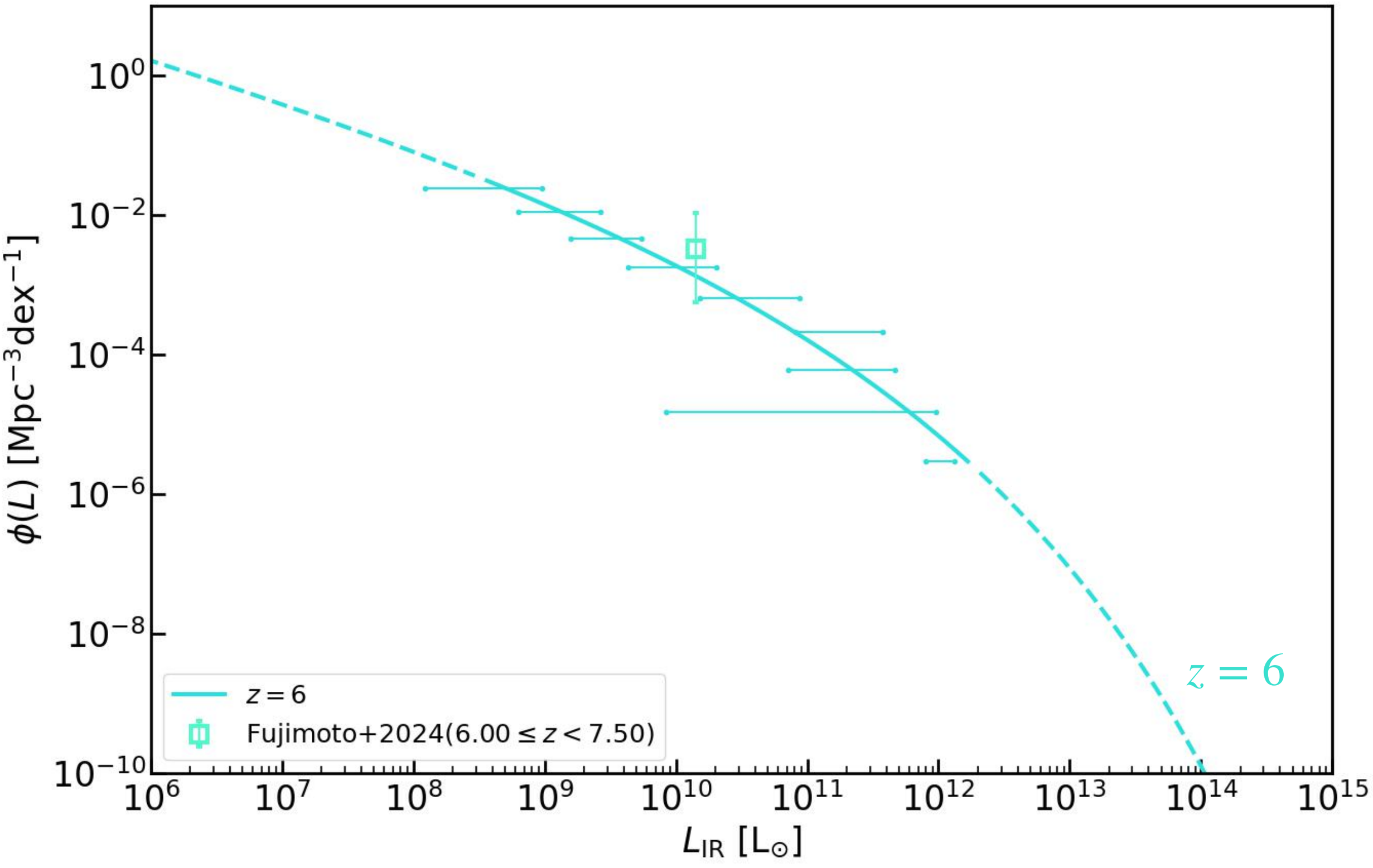

Luminosity Function

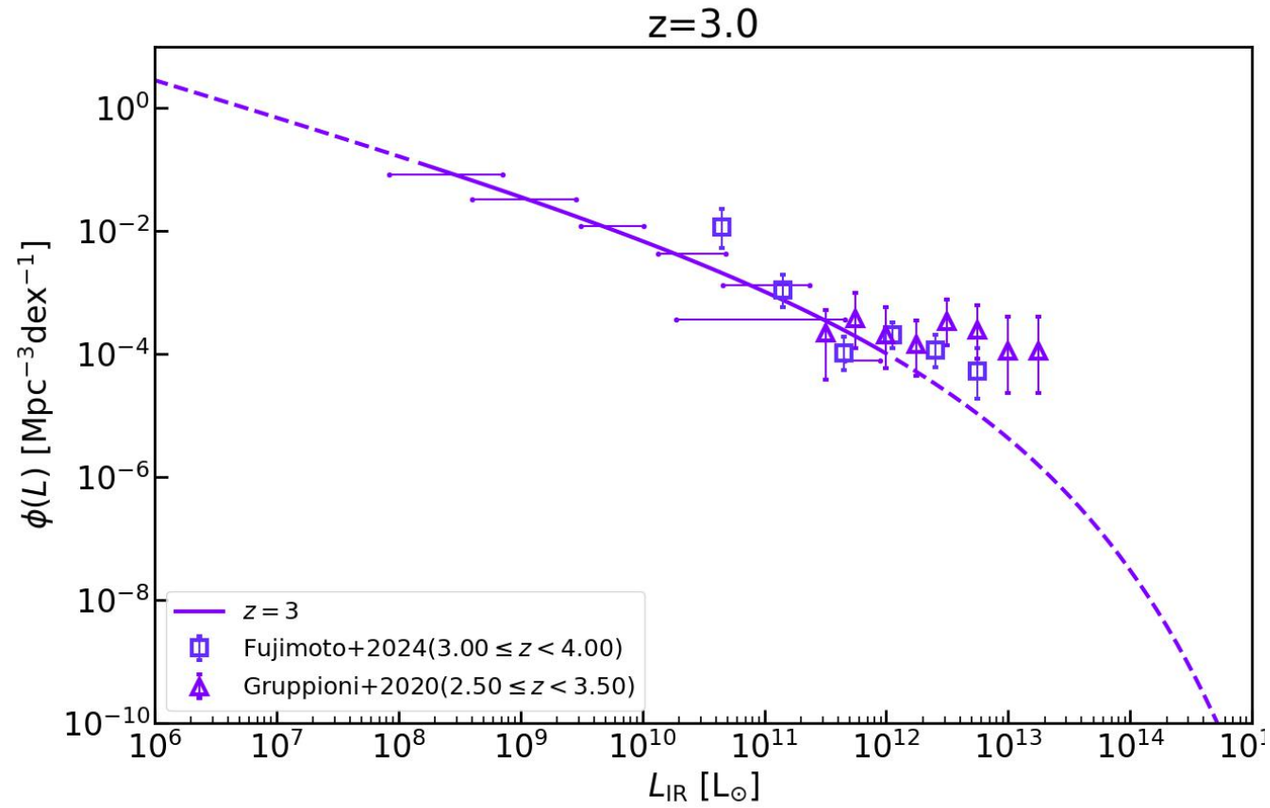

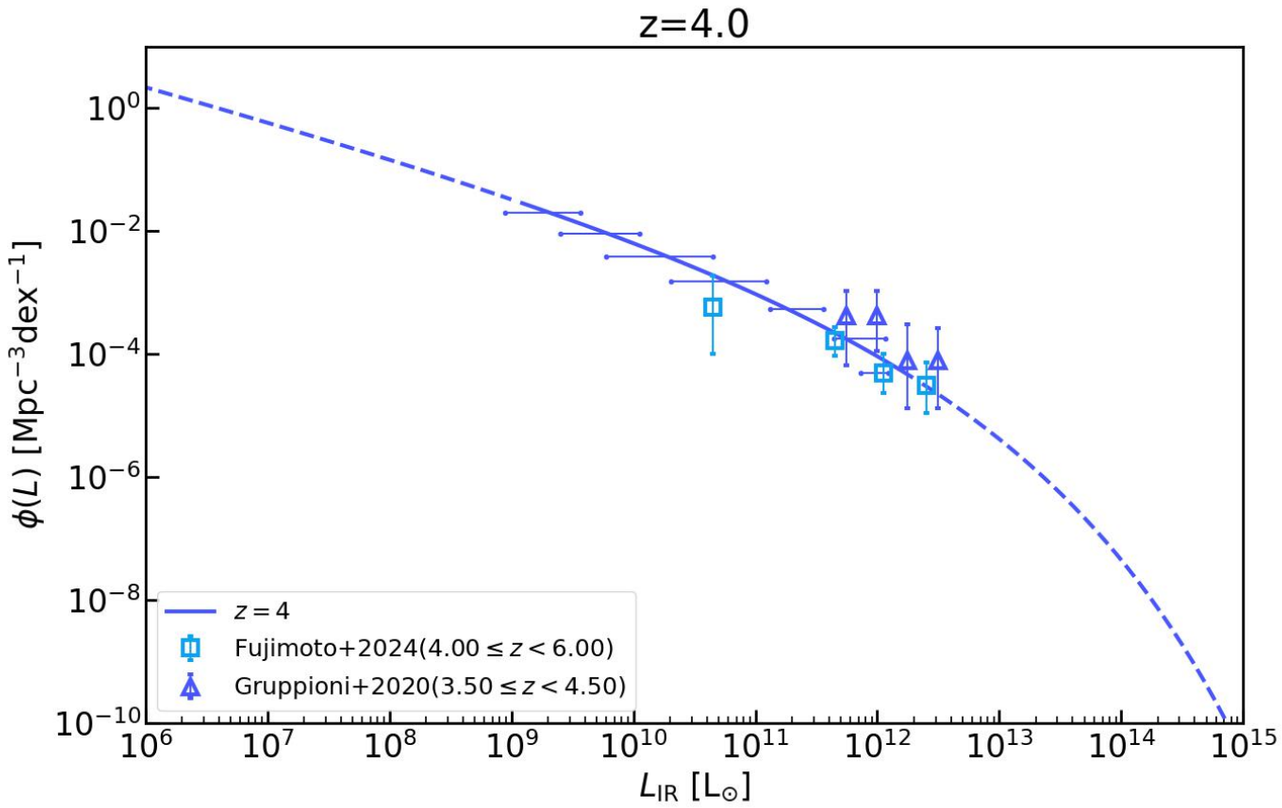

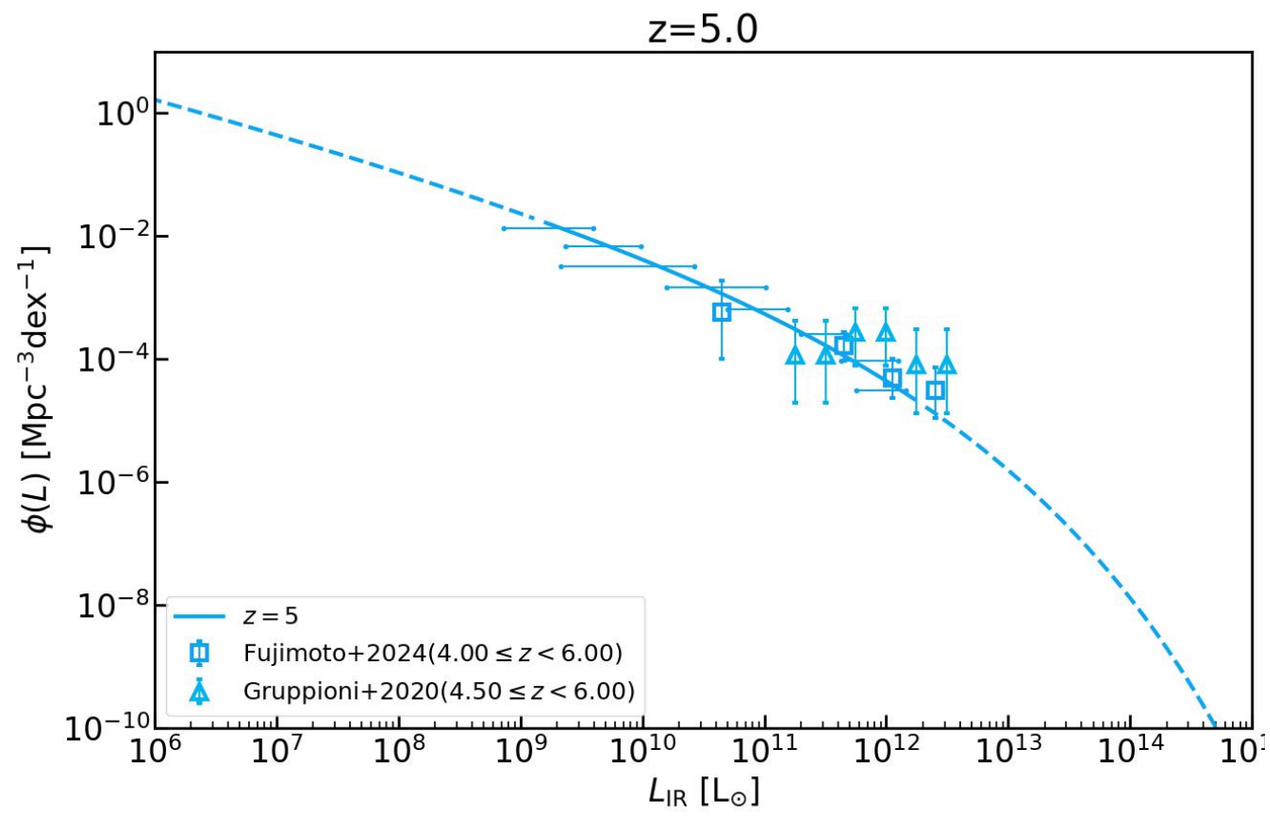

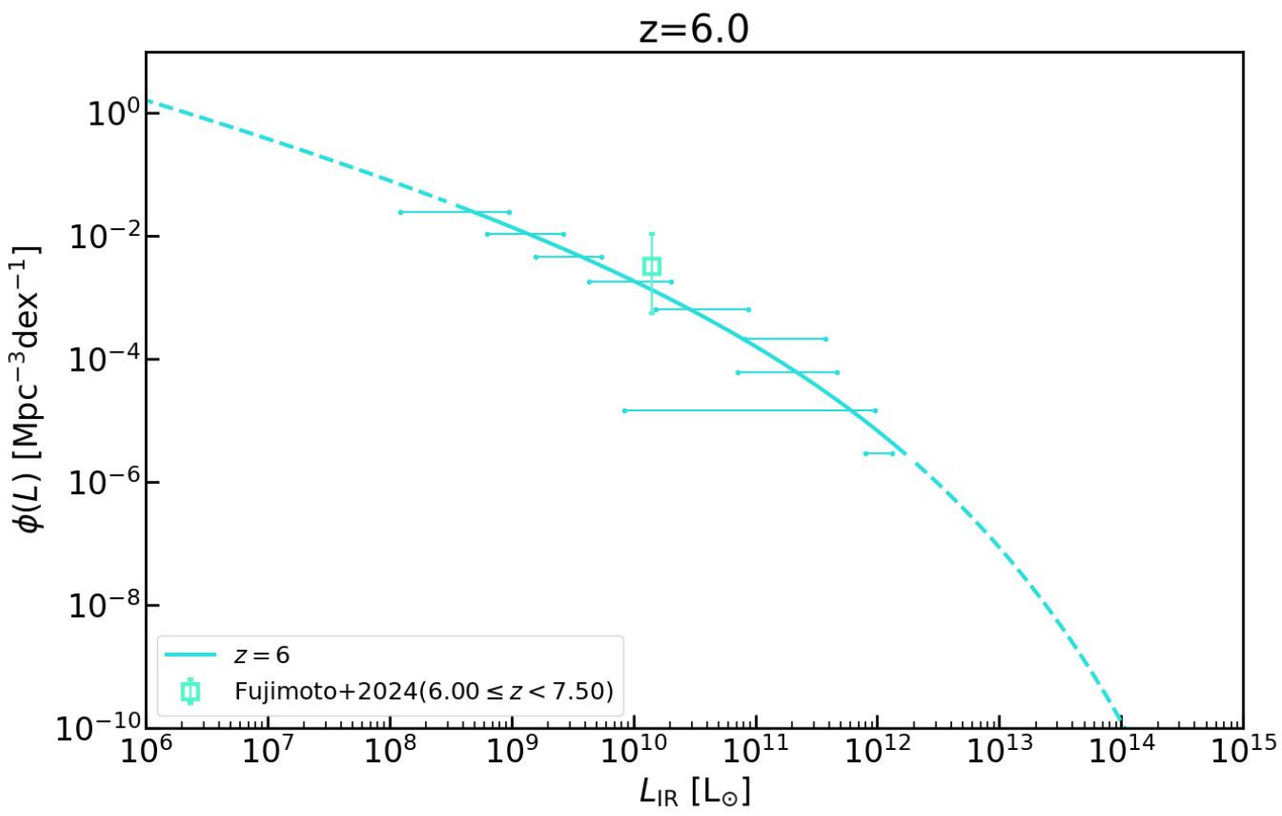

Luminosity Function

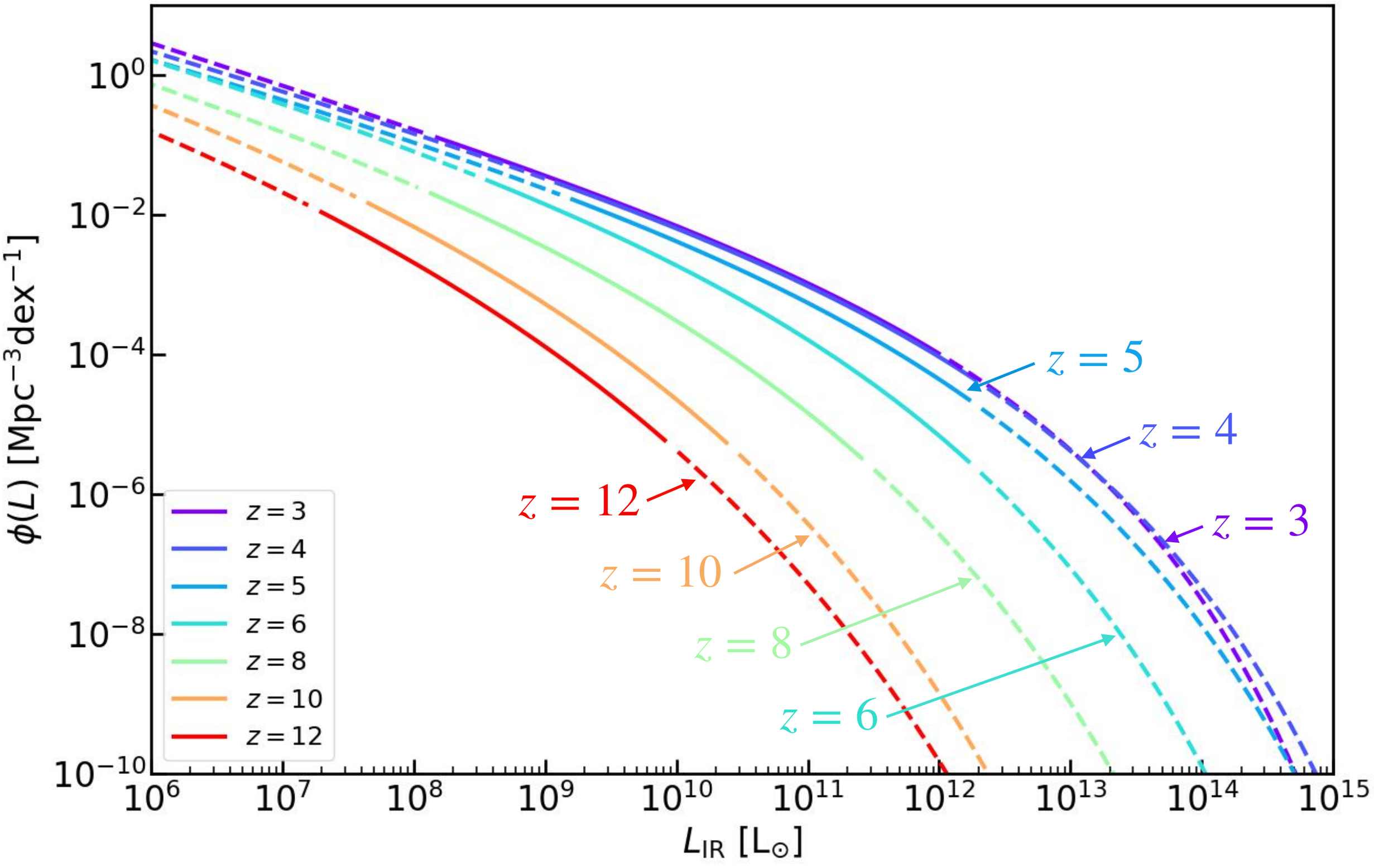

Luminosity Function

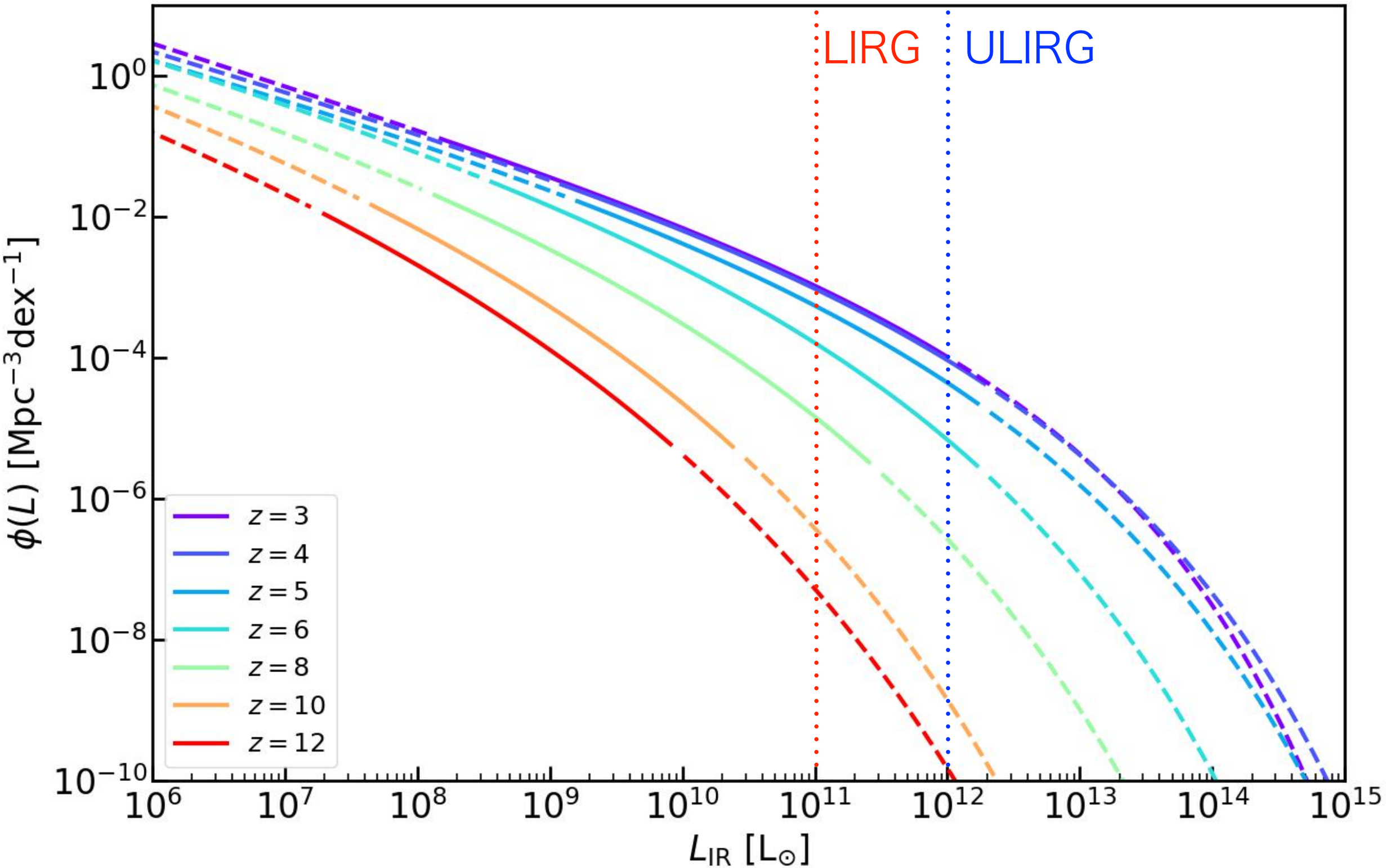

Number density of LIRG & ULIRG

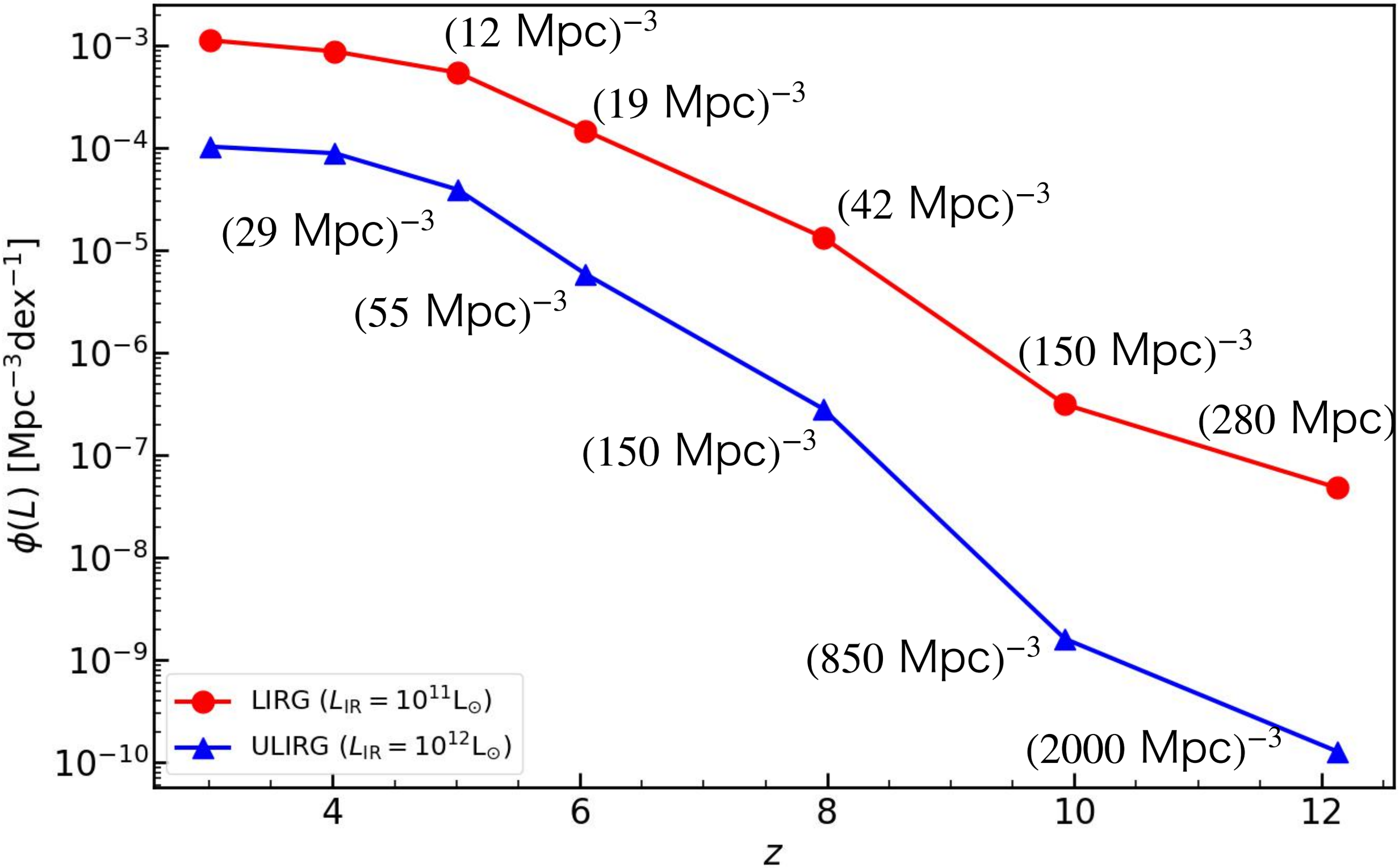

Number density of LIRG & ULIRG

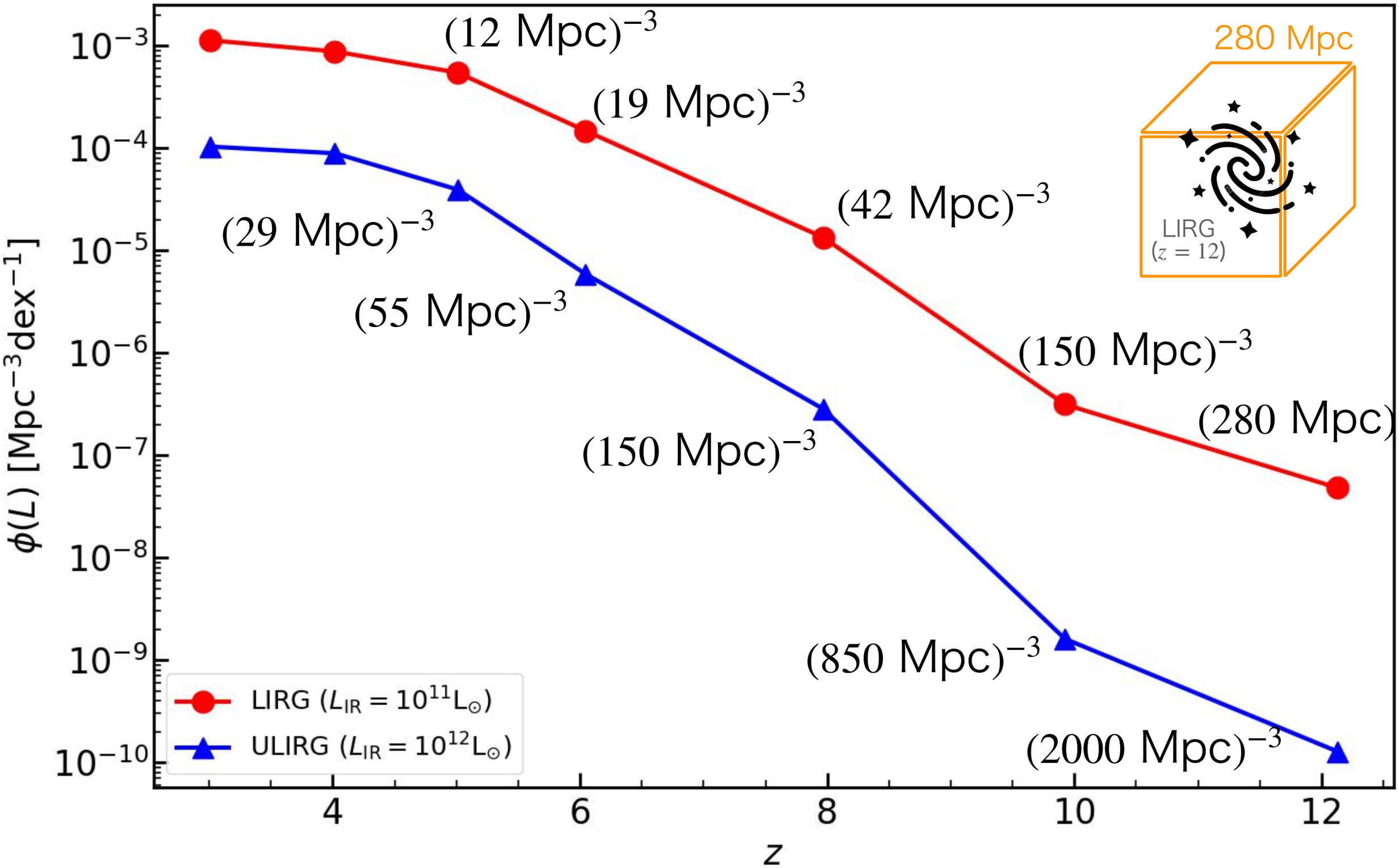

Number density of LIRG & ULIRG

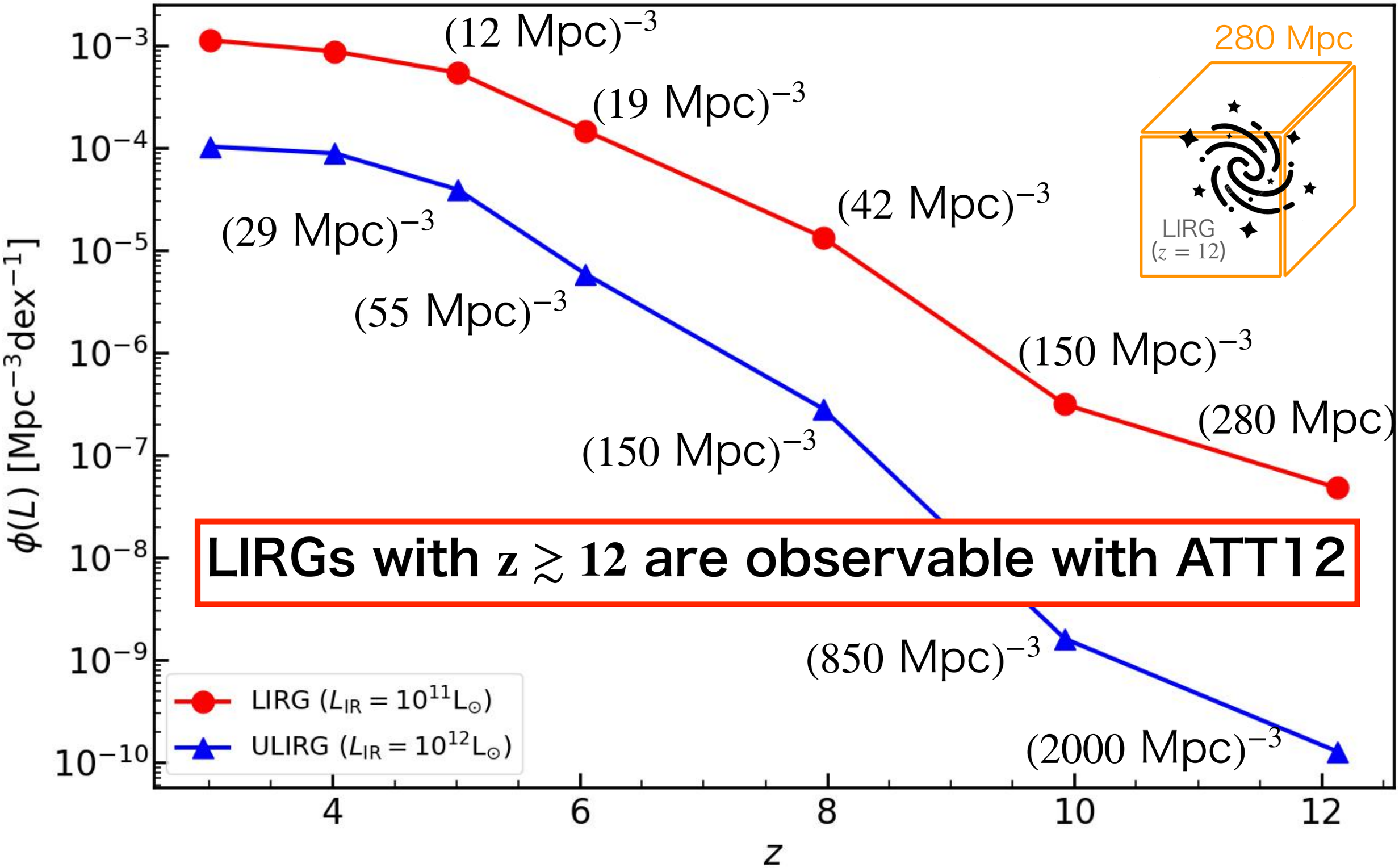

LIRGs with $z \gtrsim 12$ are observable with ATT12

1st Goal

Construct a theoretical model of dust-obscured high-z galaxies

2nd Goal

How far into the universe can the ATT12 observe?

Outline

1. Introduction
2. Method
3. Results
4. **Discussion**
5. Summary

Estimating Dust Temperatures

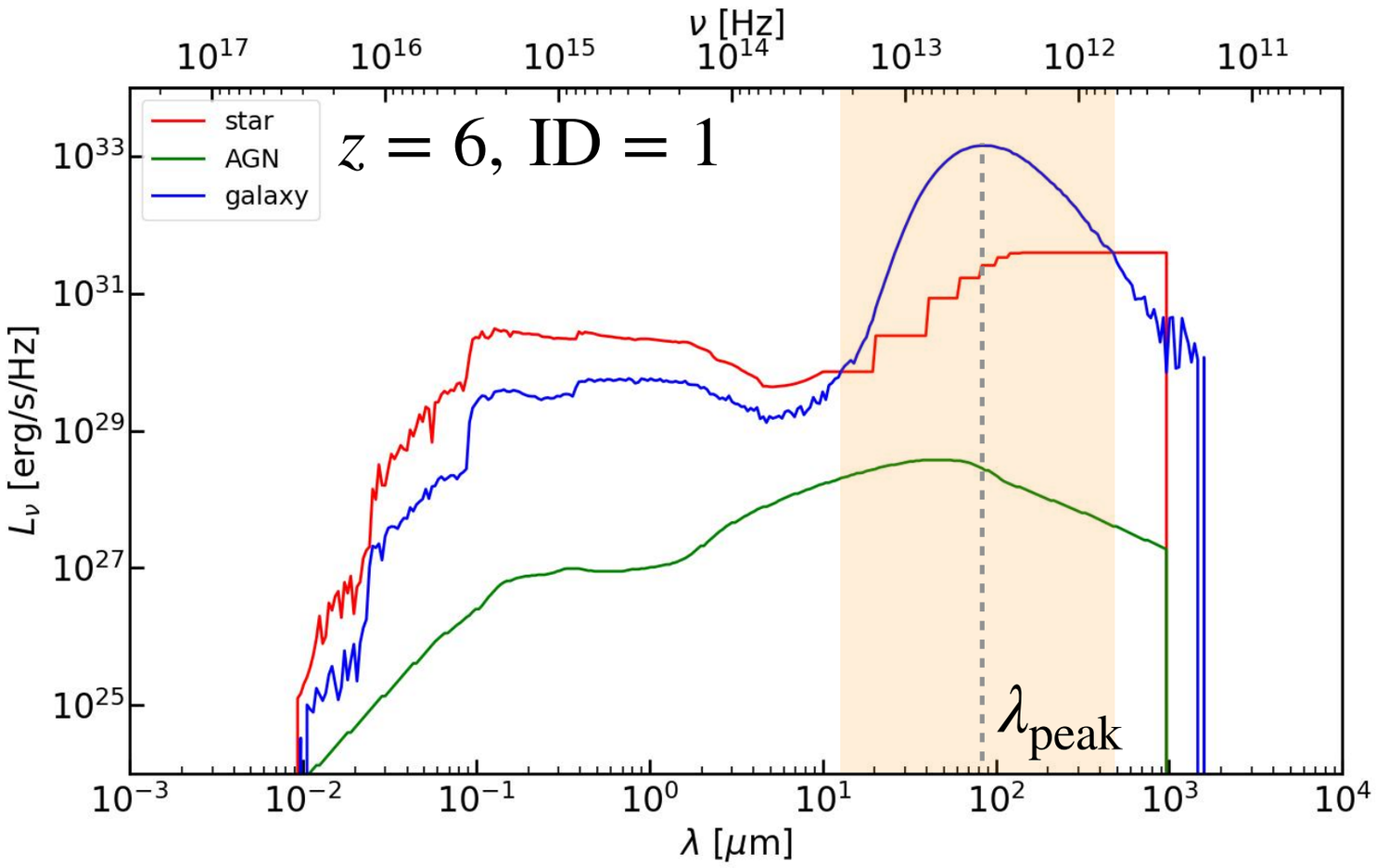

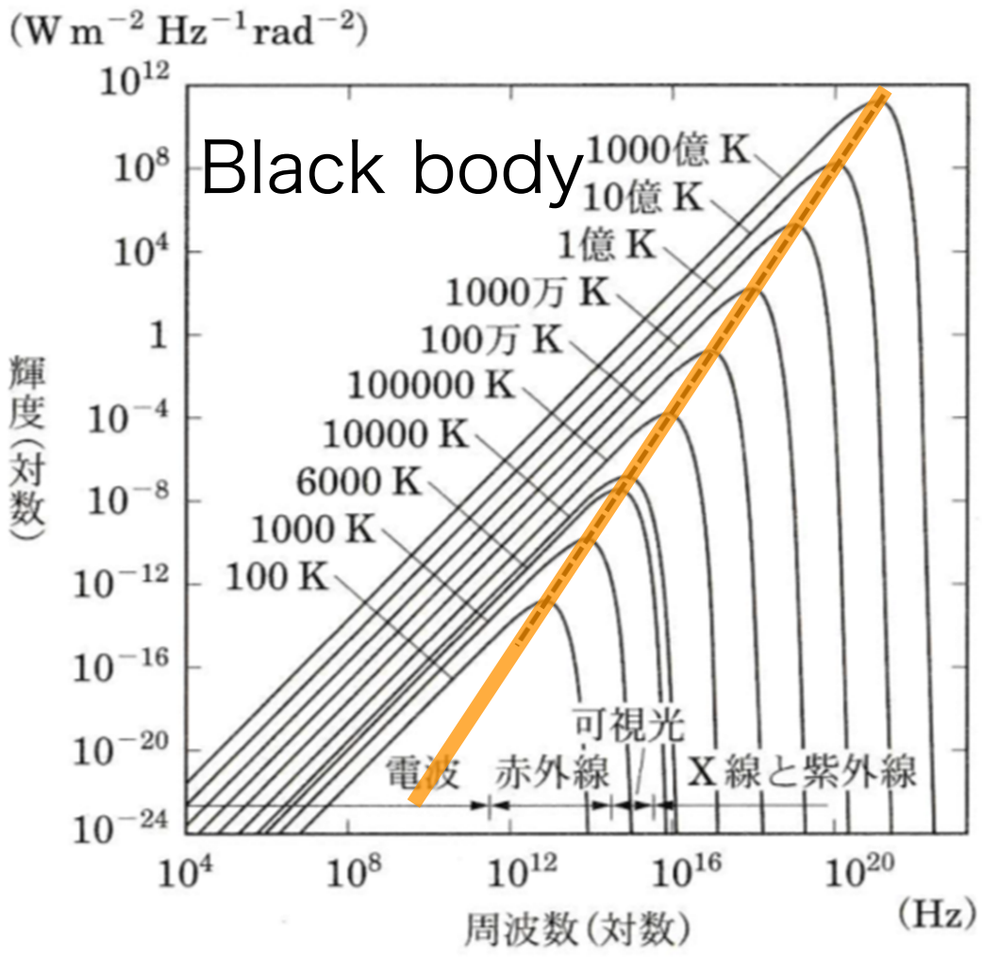

IR emission from dust grain

$\simeq$ Black body $B_\nu(T)$

Wien's displacement law

$$\nu_{\rm peak} = 5.879 \times 10^{10}\ T\ [\rm Hz]$$

Dust Temperature

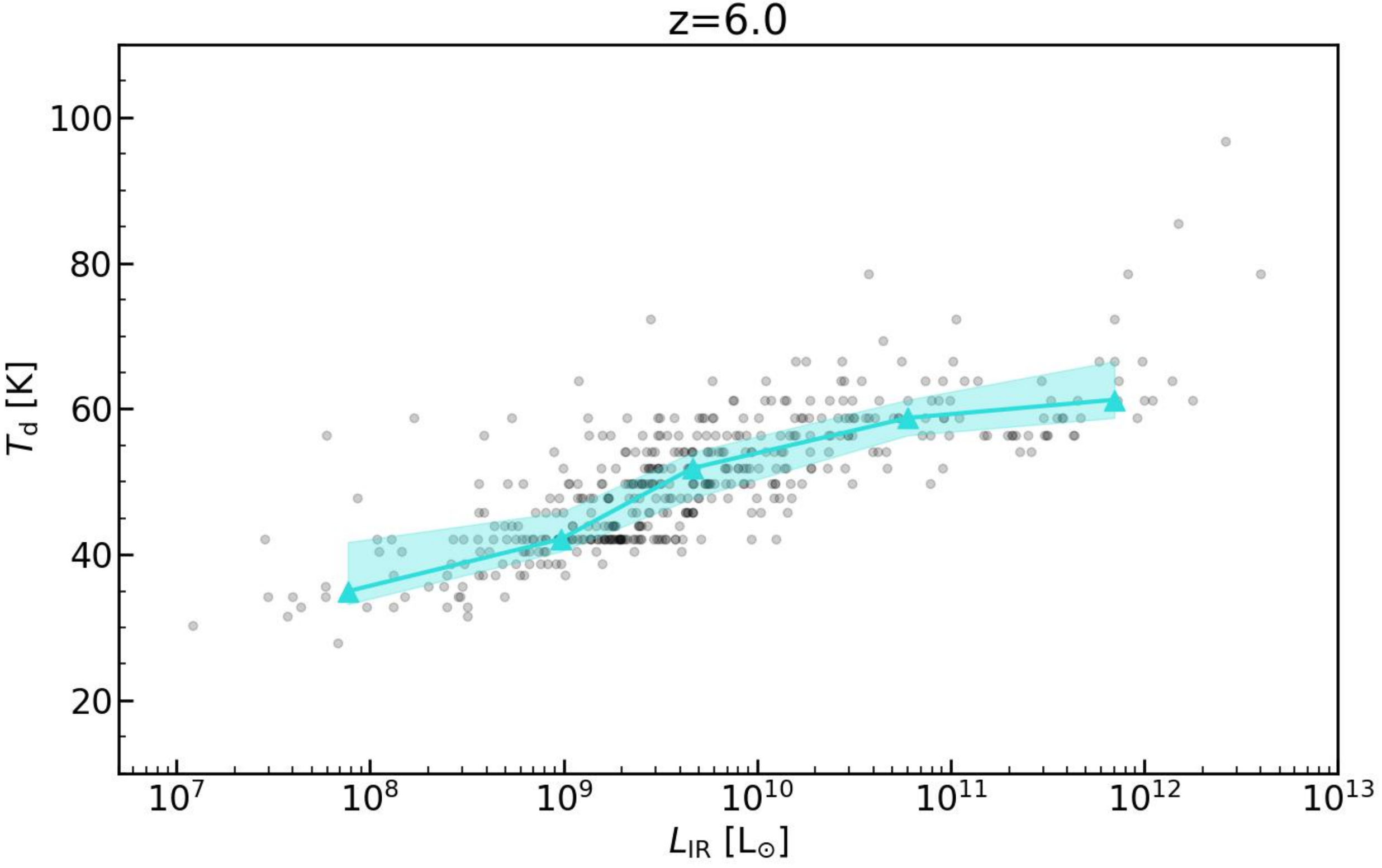

Dust Temperature

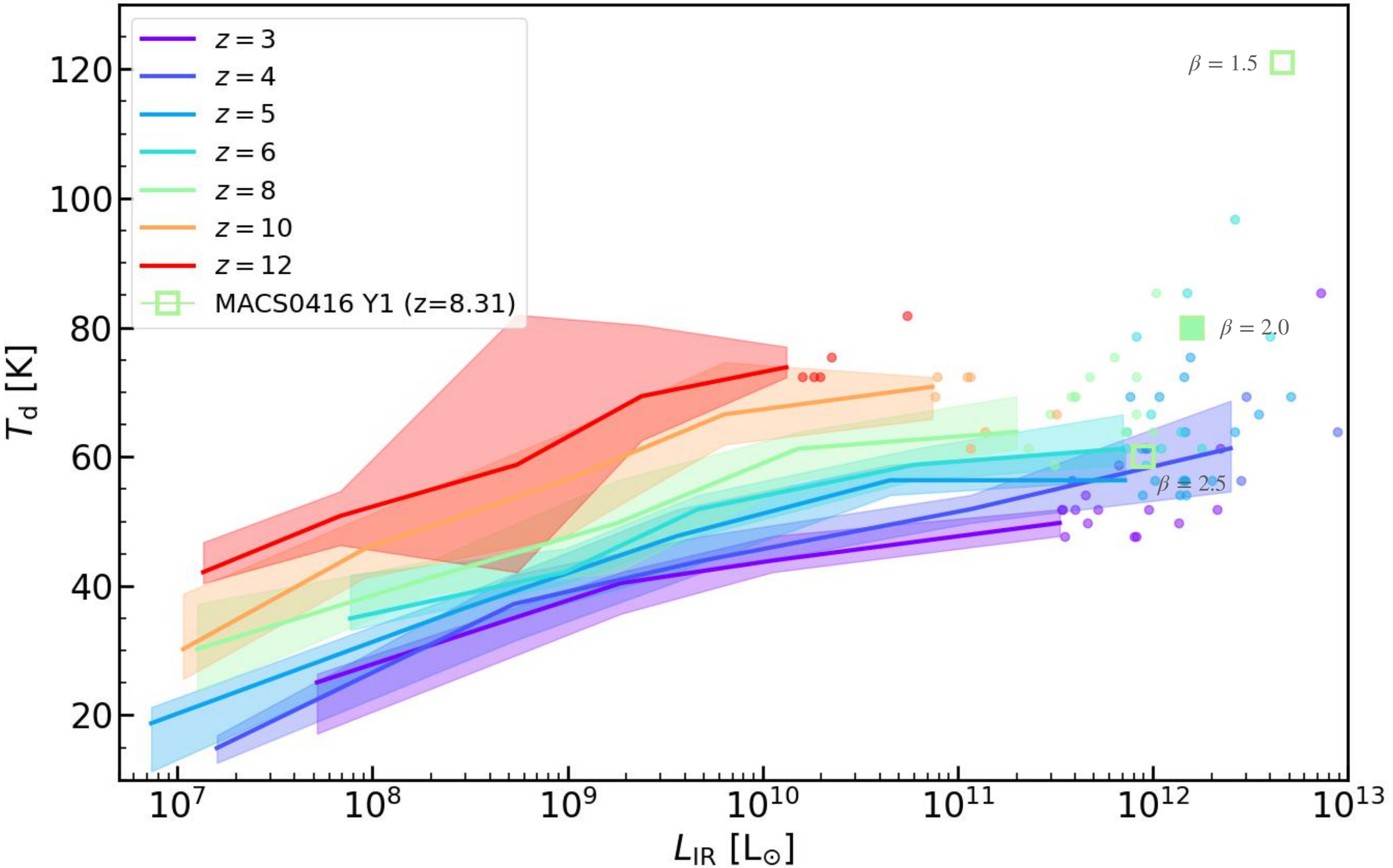

Dust Temperature

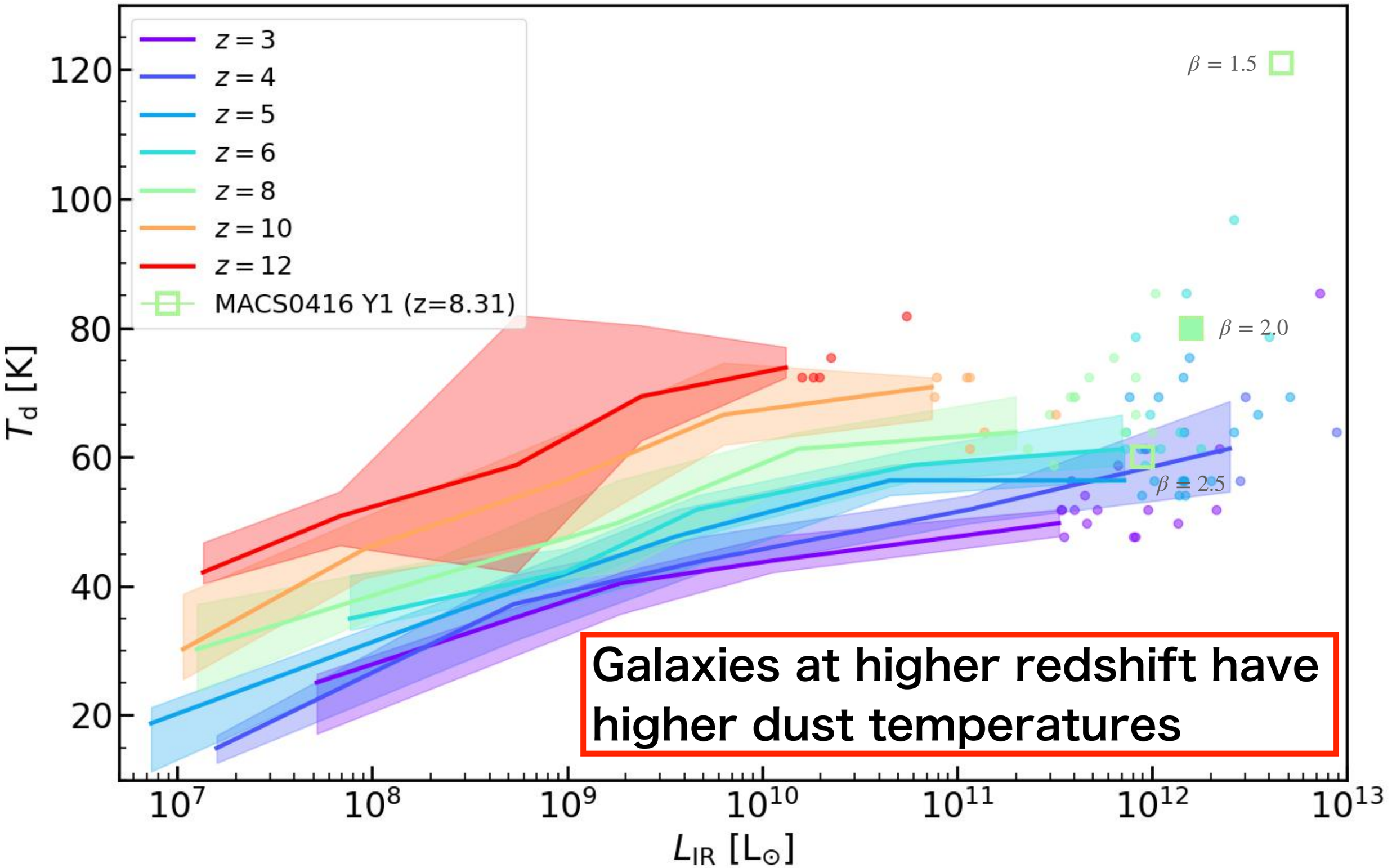

Galaxies at higher redshift have higher dust temperatures

Dust Temperature

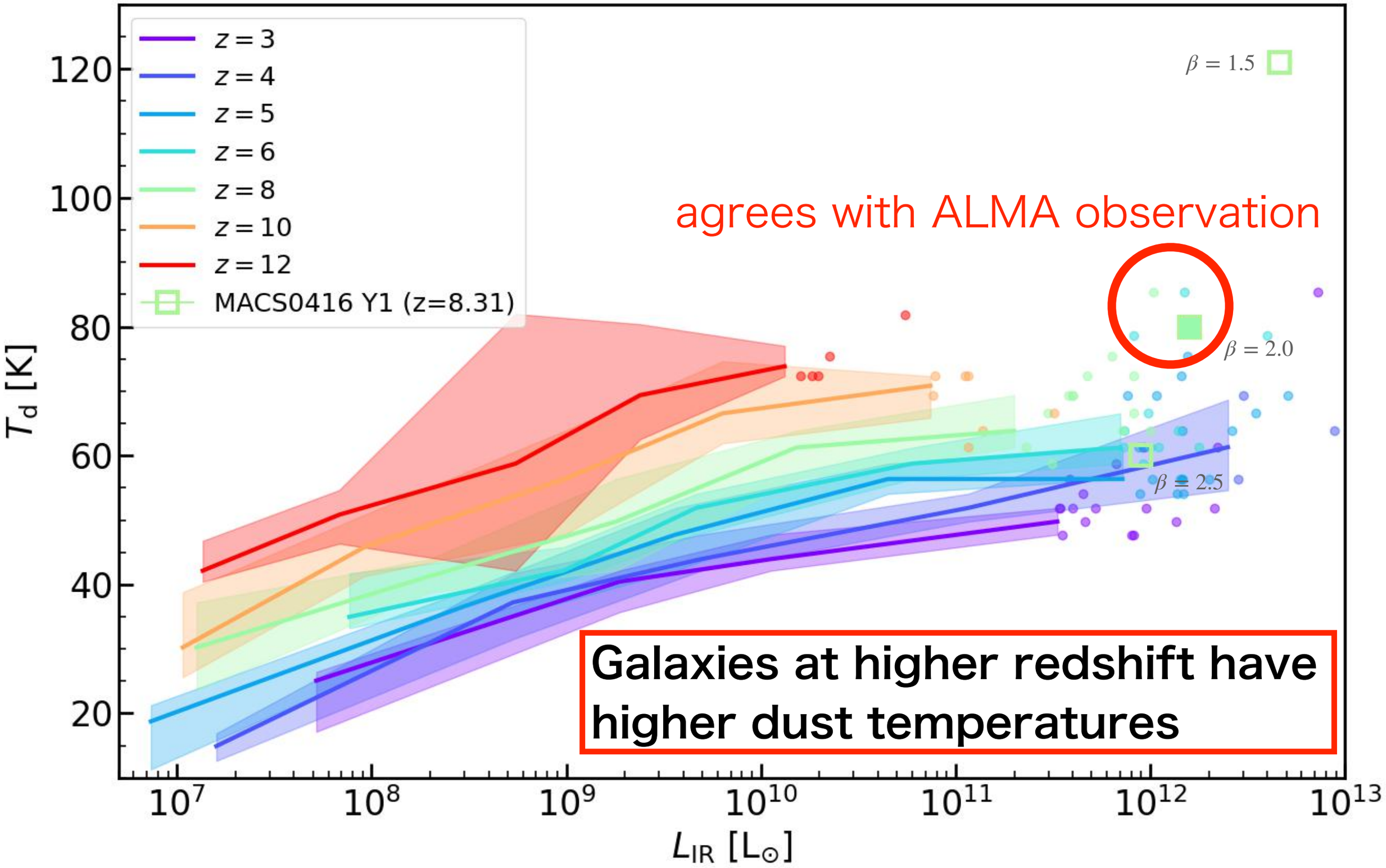

What Causes Hot Dust?

Dust temperature is determined by the balance between the absorption of stellar radiation and the infrared emission from dust grains.

$$\langle Q_{\rm abs} \rangle_\star \pi a^2 \int \frac{L_\nu}{4\pi R^2} d\nu = 4\pi a^2 \langle Q_{\rm abs} \rangle_{T_{\rm d}} \sigma T_{\rm d}^4$$

absorption　　IR emission

$\langle Q_{\rm abs} \rangle_\star$: spectrum-averaged absorption cross section

a : radius of dust grain

L_ν : stellar luminosity per unit frequency

σ : Stefan–Boltzmann constant

$\langle Q_{\rm abs} \rangle_{T_{\rm d}}$: Planck-averaged emission efficiency

$$\rightarrow \quad T_{\rm d} = \left(\frac{1}{16\pi\sigma} \frac{\langle Q_{\rm abs} \rangle_\star}{\langle Q_{\rm abs} \rangle_{T_{\rm d}}} \right) L_{\rm bol}^{1/4} \, R^{-1/2}$$

Suggests a relation with galaxy compactness

Half-light Radius

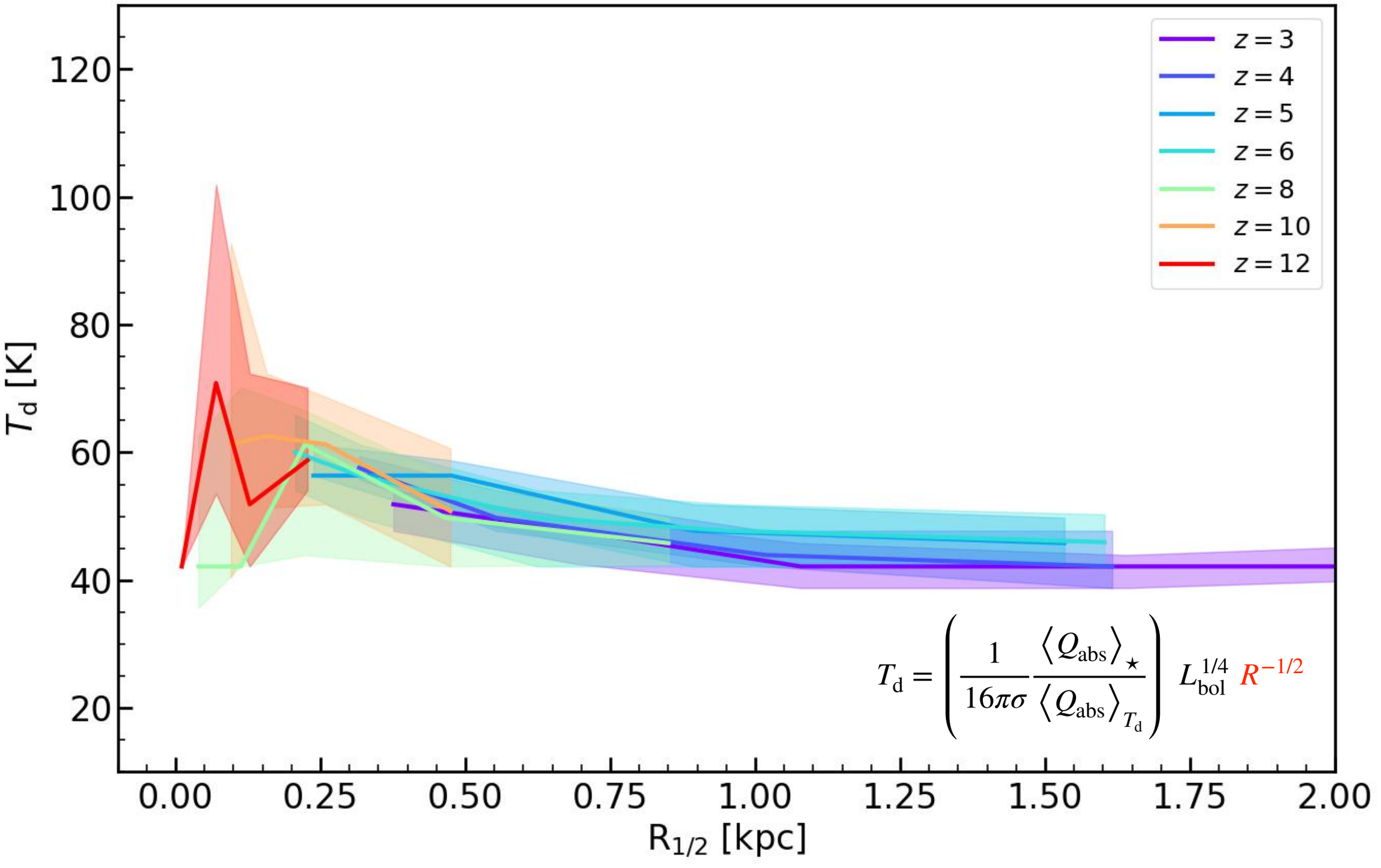

Half-light Radius

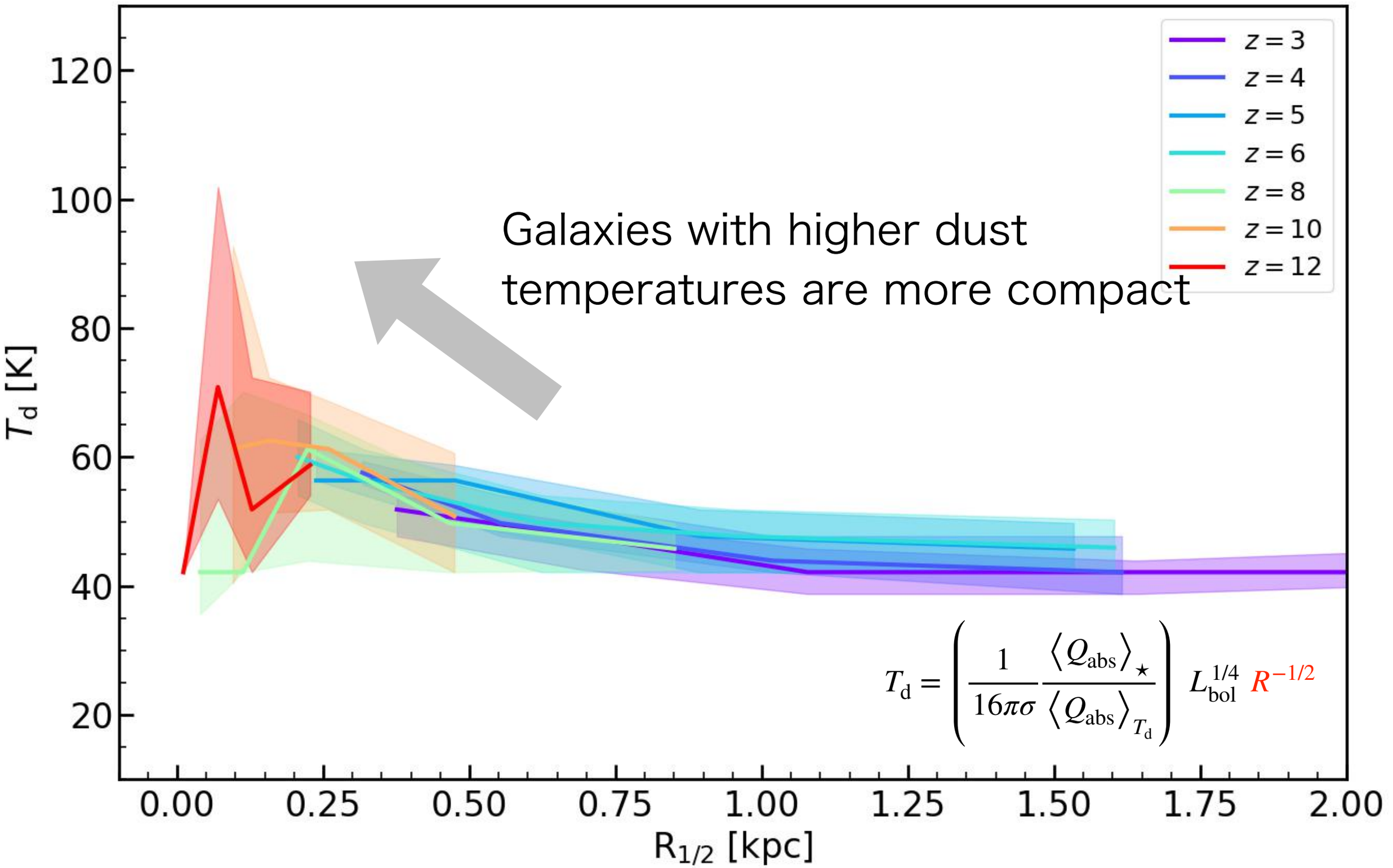

Half-light Radius

$$T_{\rm d} = \left(\frac{1}{16\pi\sigma} \frac{\langle Q_{\rm abs} \rangle_{\star}}{\langle Q_{\rm abs} \rangle_{T_{\rm d}}} \right) L_{\rm bol}^{1/4} \, R^{-1/2}$$

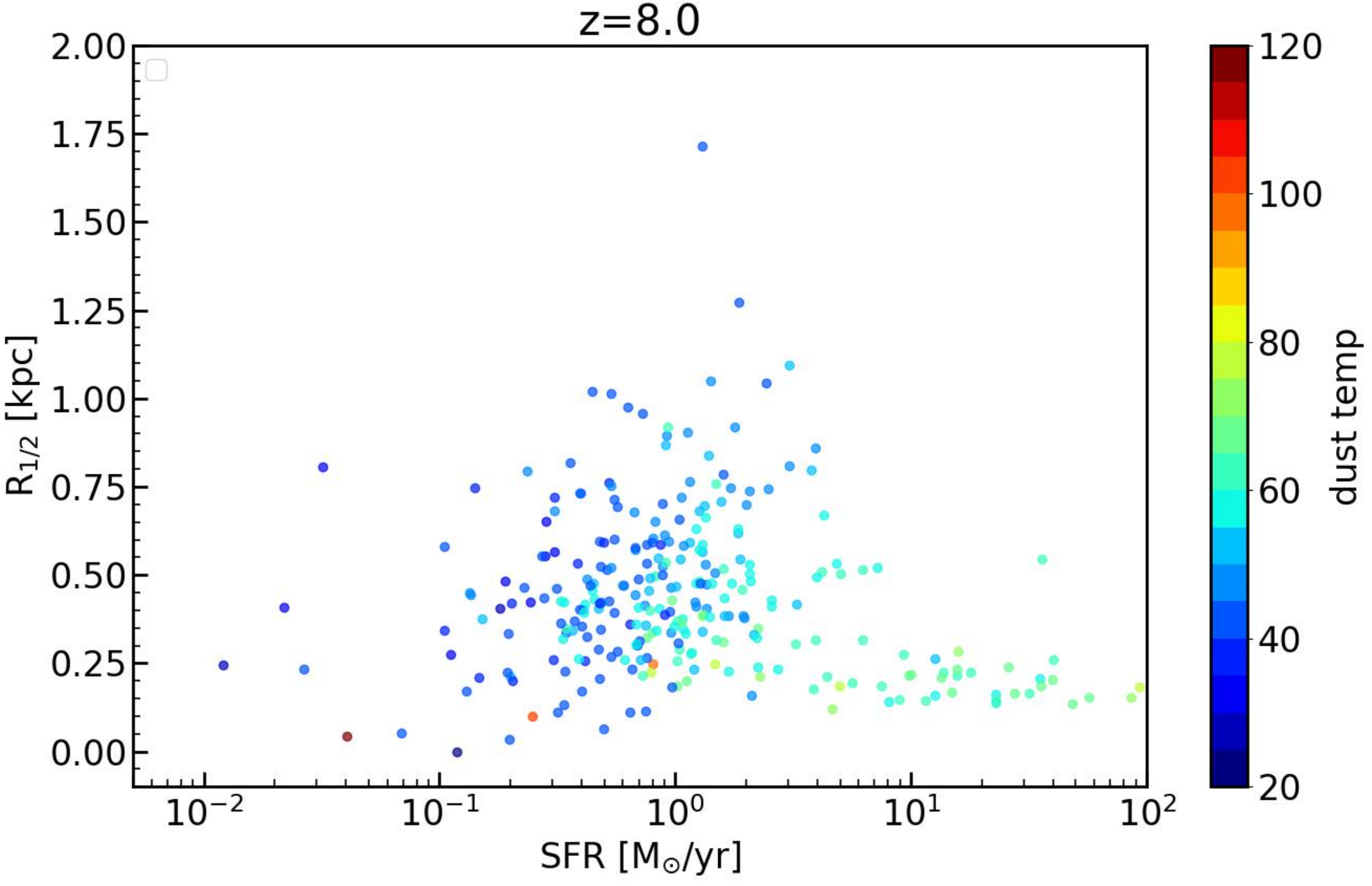

Half-light Radius

$$T_{\rm d} = \left(\frac{1}{16\pi\sigma} \frac{\langle Q_{\rm abs} \rangle_{\star}}{\langle Q_{\rm abs} \rangle_{T_{\rm d}}} \right) L_{\rm bol}^{1/4} \; R^{-1/2}$$

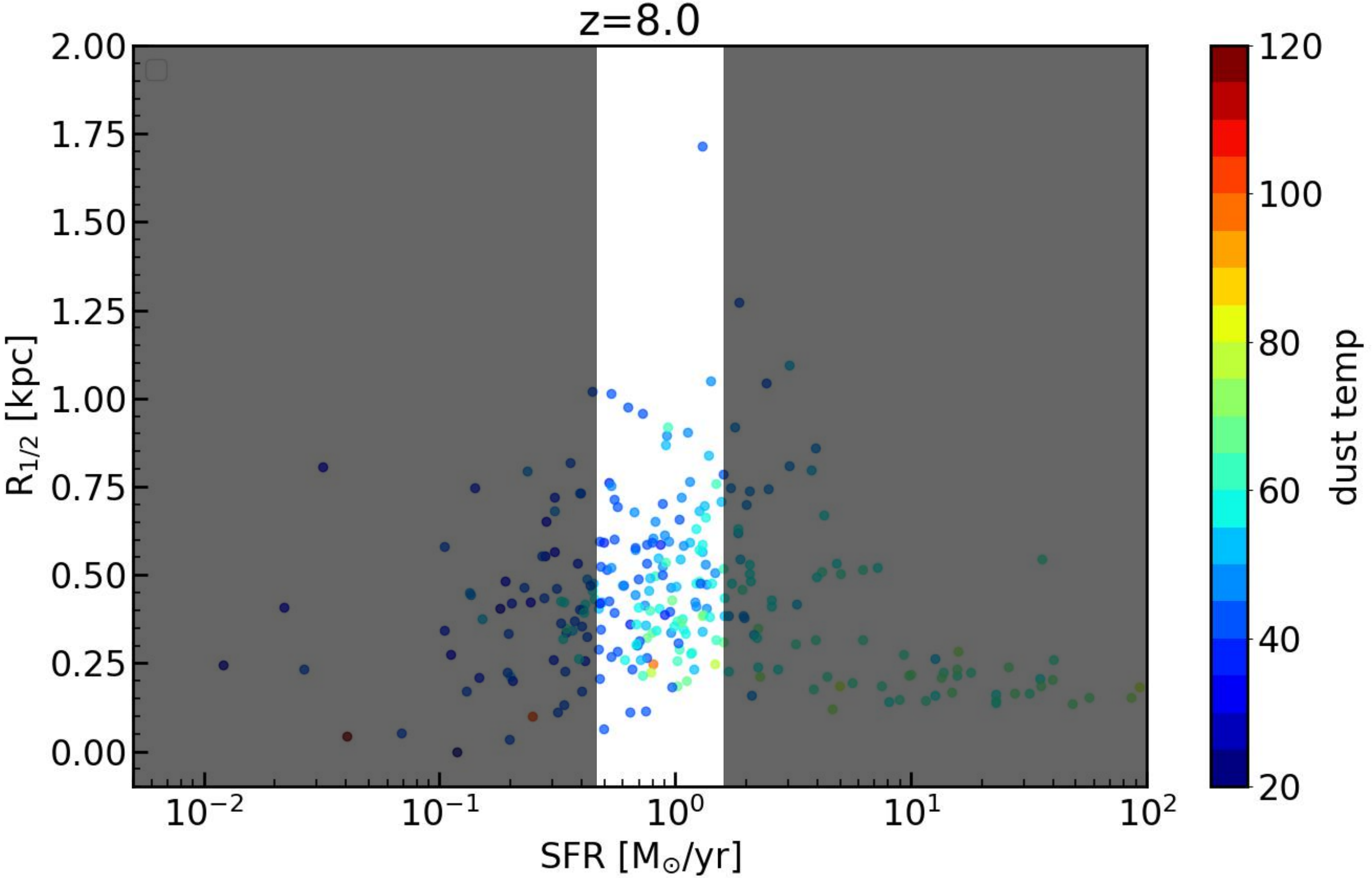

Half-light Radius

$$T_{\rm d} = \left(\frac{1}{16\pi\sigma} \frac{\langle Q_{\rm abs} \rangle_{\star}}{\langle Q_{\rm abs} \rangle_{T_{\rm d}}} \right) L_{\rm bol}^{1/4} \; R^{-1/2}$$

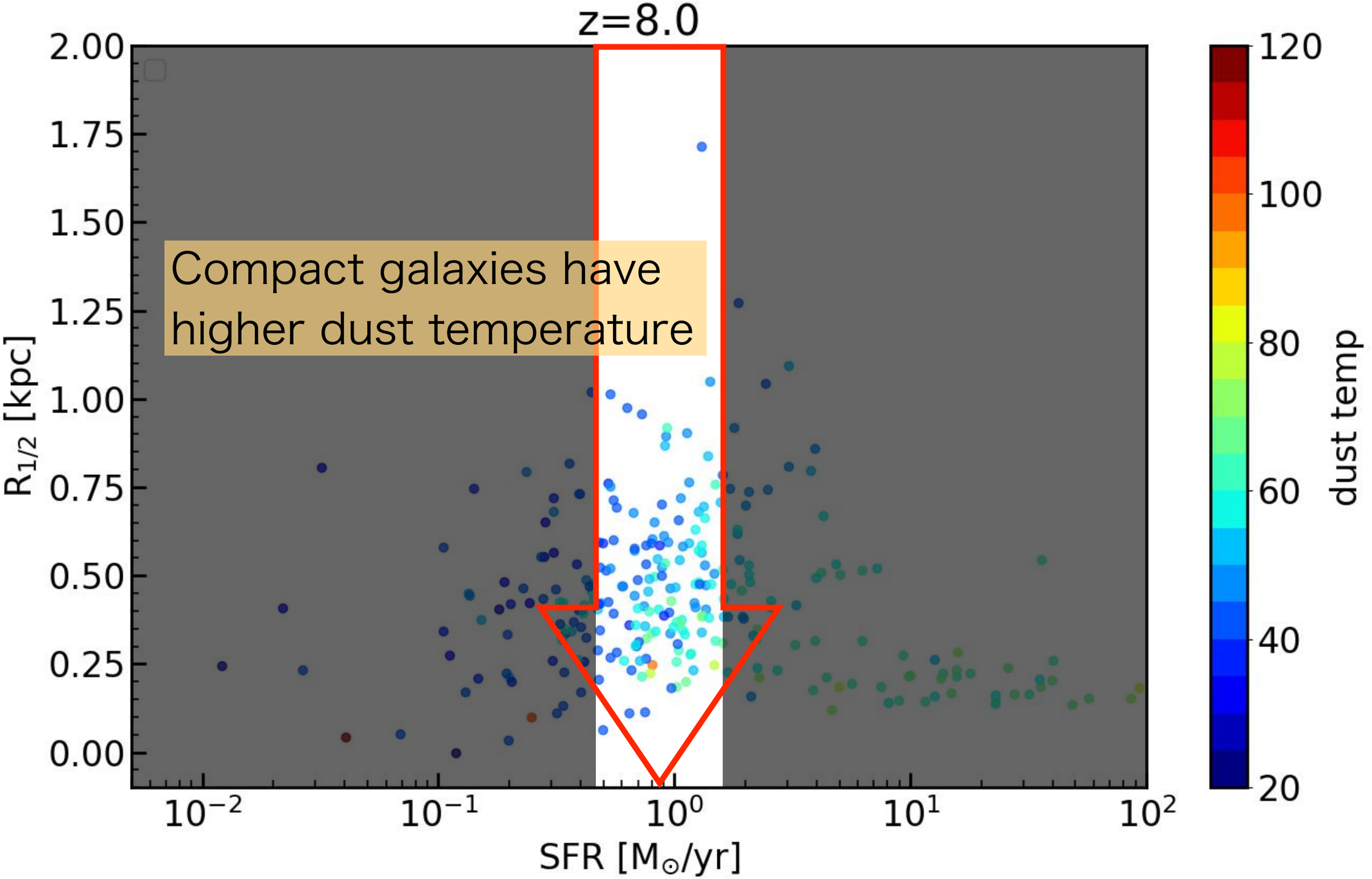

Half-light Radius

$$T_{\rm d} = \left(\frac{1}{16\pi\sigma} \frac{\langle Q_{\rm abs} \rangle_{\star}}{\langle Q_{\rm abs} \rangle_{T_{\rm d}}} \right) L_{\rm bol}^{1/4} \, R^{-1/2}$$

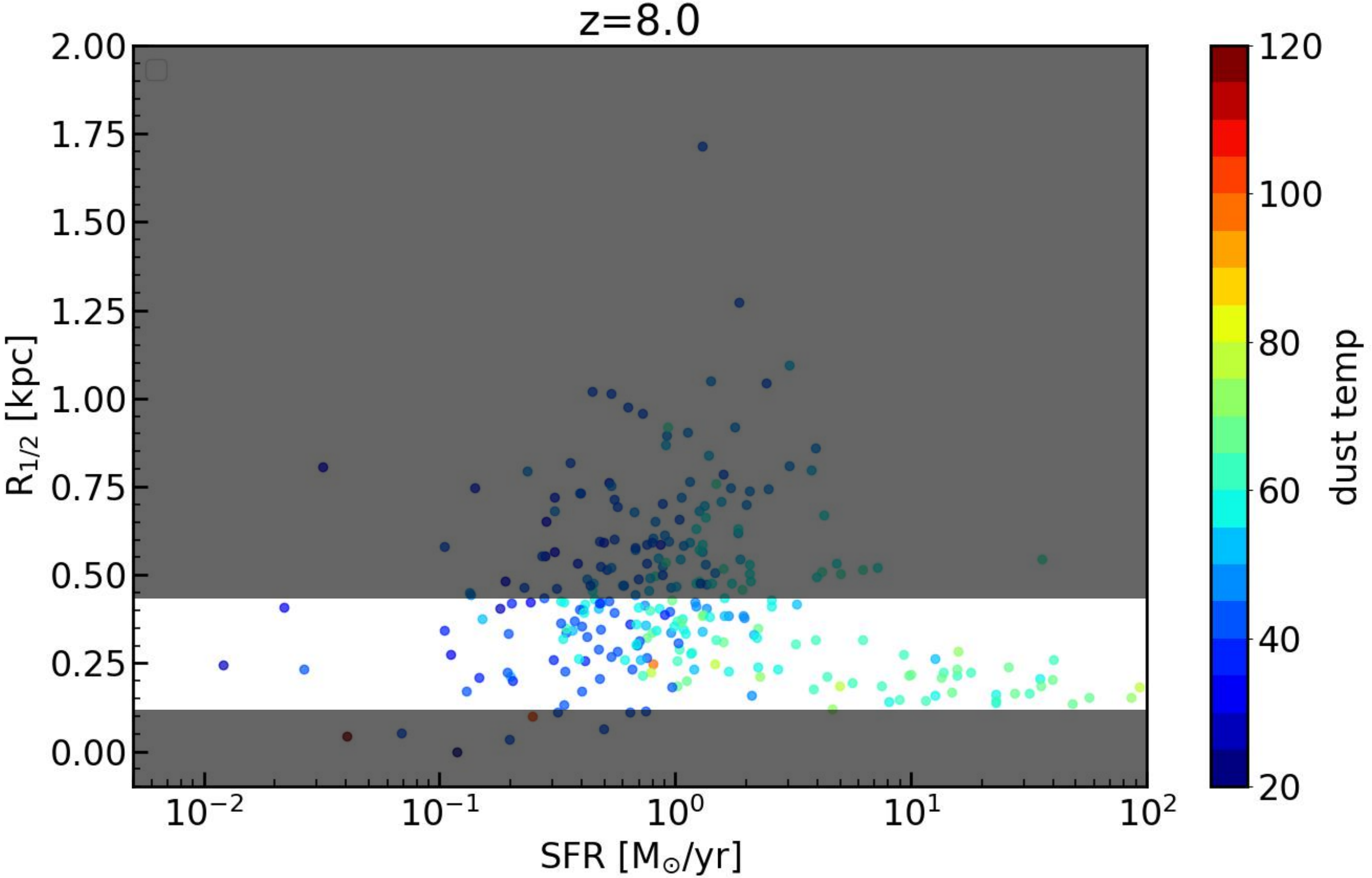

Half-light Radius

$$T_{\rm d} = \left(\frac{1}{16\pi\sigma} \frac{\langle Q_{\rm abs} \rangle_{\star}}{\langle Q_{\rm abs} \rangle_{T_{\rm d}}} \right) L_{\rm bol}^{1/4} \, R^{-1/2}$$

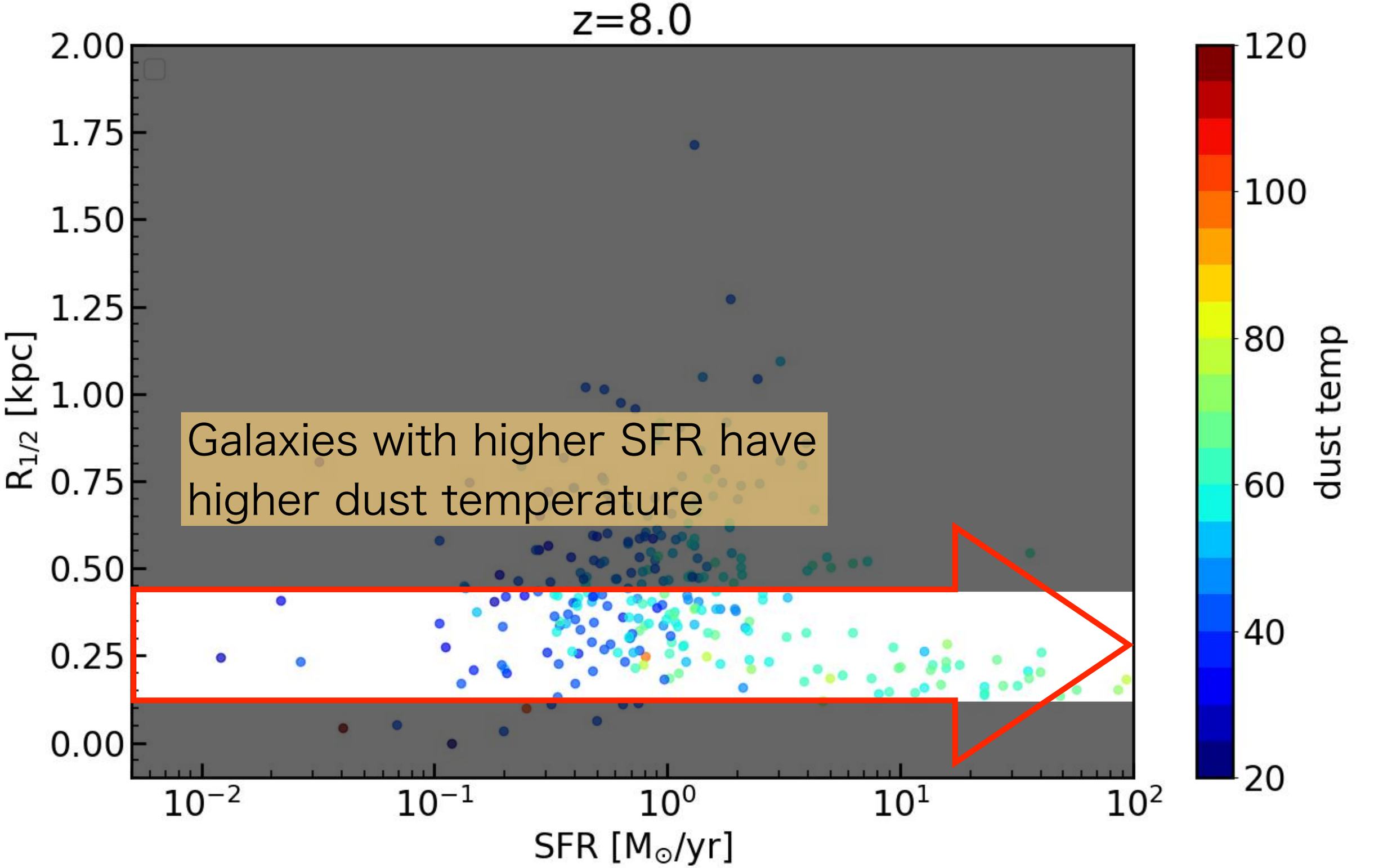

Half-light Radius

$$T_{\rm d} = \left(\frac{1}{16\pi\sigma} \frac{\langle Q_{\rm abs} \rangle_{\star}}{\langle Q_{\rm abs} \rangle_{T_{\rm d}}} \right) L_{\rm bol}^{1/4} \, R^{-1/2}$$

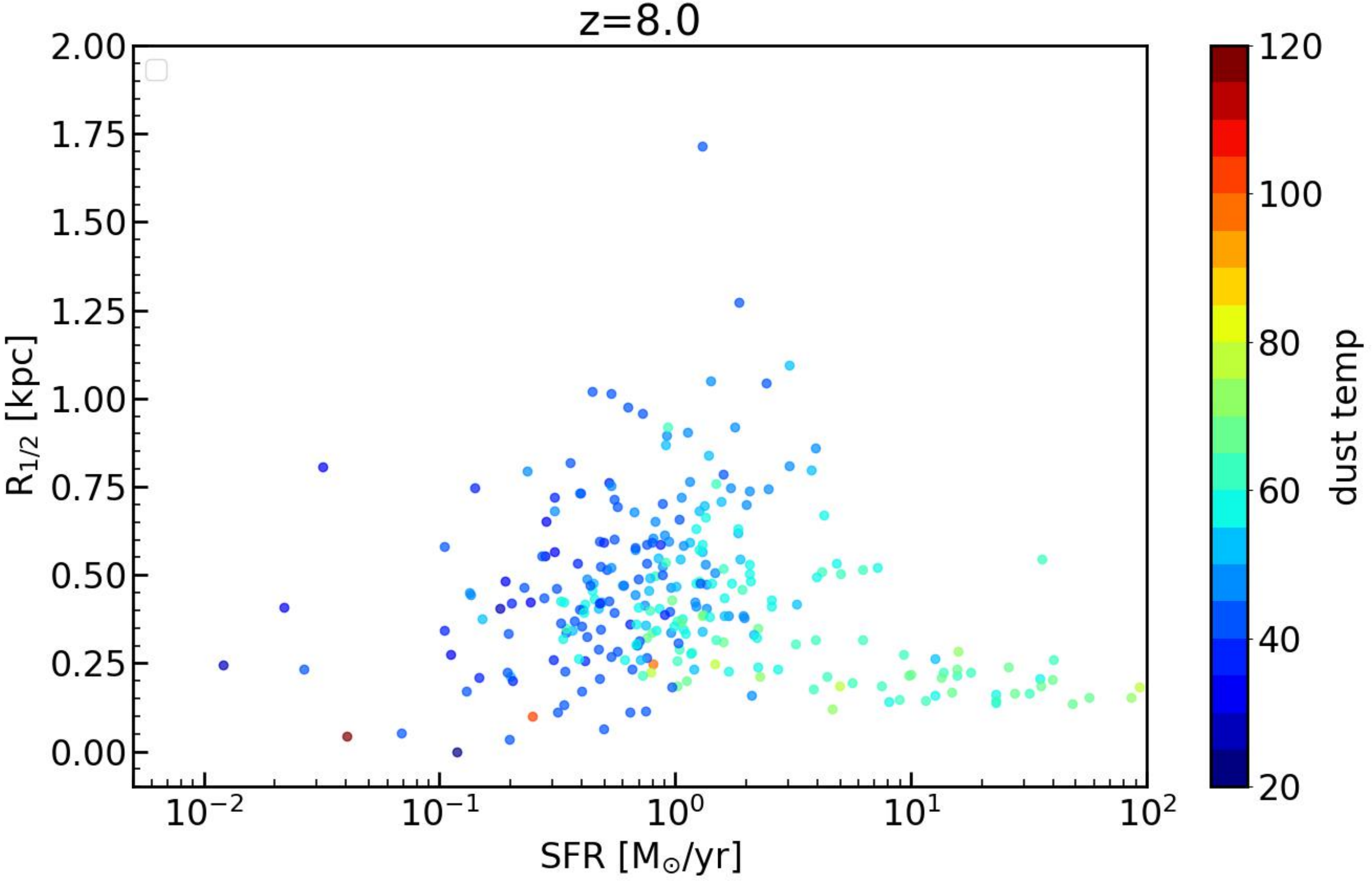

Outline

1. Introduction
2. Method
3. Results
4. Discussion
5. **Summary**

Summary

- Performed 3D Monte Carlo radiative transfer simulations with **ART2** for ~1000 galaxies from the cosmological simulation dataset **FOREVER22**
- Predicted luminosity functions at $z = 6 - 12$
- Simulations reproduce ALMA-observed hot-dust galaxies with $T_{\rm d} \gtrsim 80$ K
- High dust temperature mainly originates from compact galaxy structure

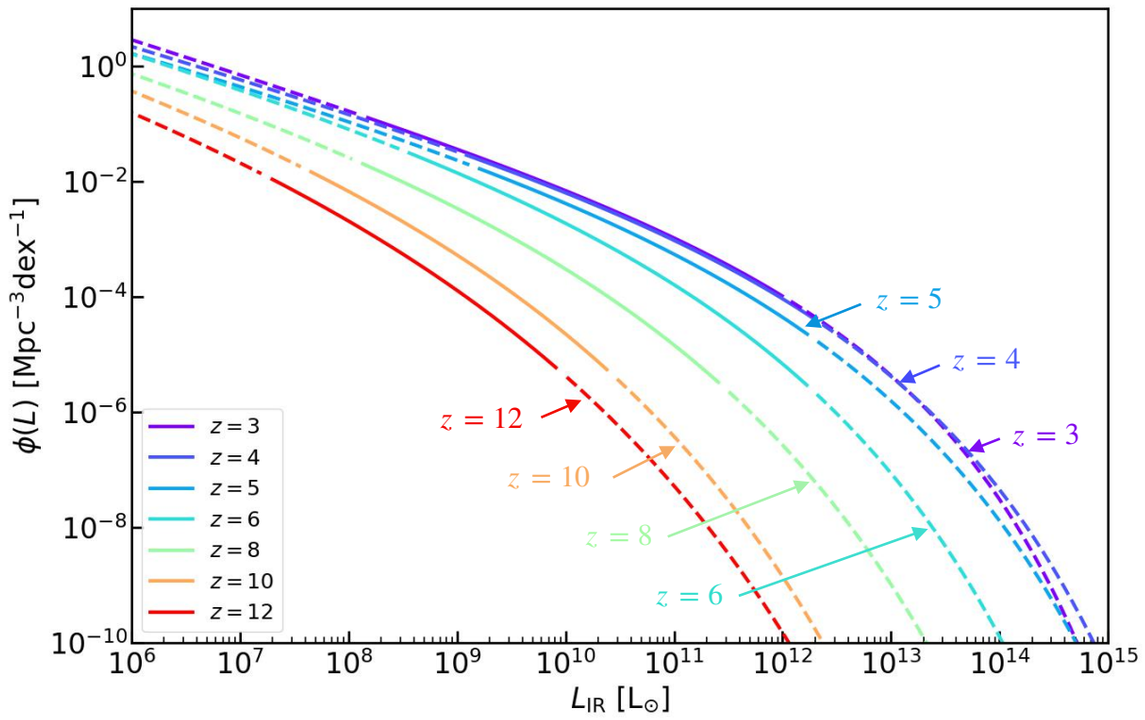

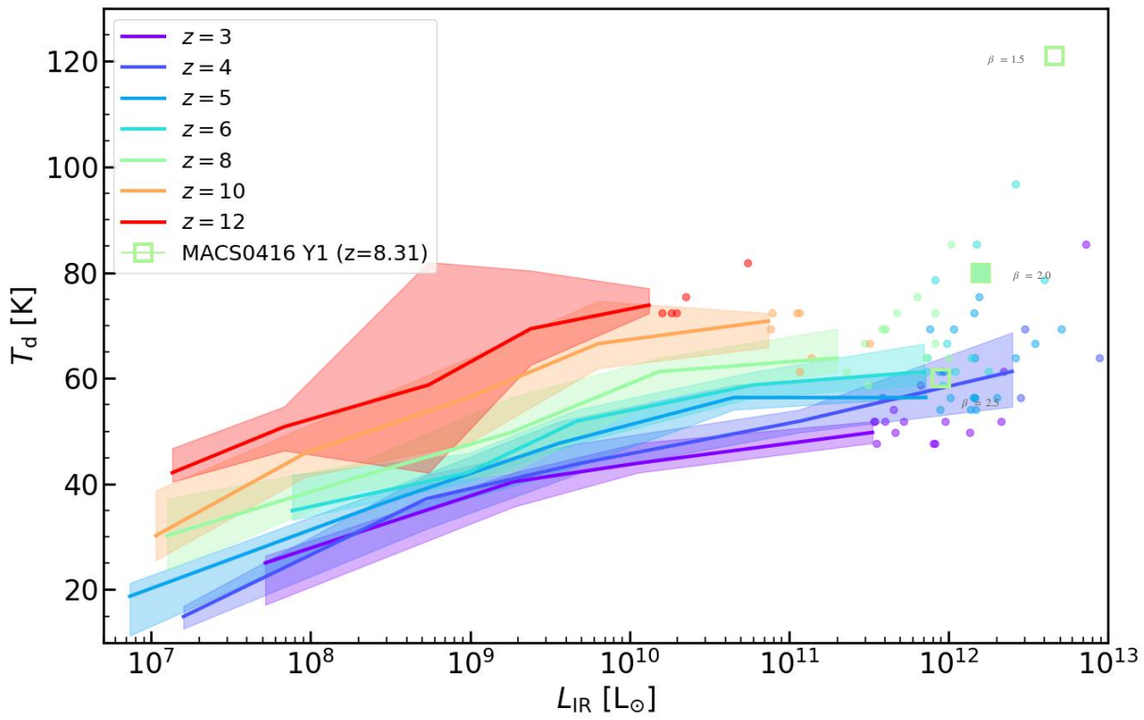

Appendix

Data & Code

Forever22

“FORmation and EVolution of galaxies in Extremely overdense Regions” (Yajima et al. 2022)

- A large-scale cosmological hydrodynamic simulation
- Proto-Cluster Region: $V = (28.6\ \mathrm{cMpc})^3$, $m_{\mathrm{SPH}} = 4.1 \times 10^6\ \mathrm{M}_\odot$

ART2

“All-wavelength Radiative Transfer with Adaptive Refinement Tree” (Yajima et al. 2012, Li et al. 2008)

- A 3D Monte Carlo radiative transfer code
- Includes Lyα from recombination and collisional excitation, and continuum absorption, scattering, and thermal emission

Simulation setup

10^6 photons,　1362 (948) halos in total,　redshift：6, 8, 10, 12

Input: FOREVER22

Modification to GADGET-3

- Update the star formation and supernova (SN) feedback models (OWLS project, EAGLE project)
- Add formation of Pop III stars, Lyman-Werner feedback and non-equilibrium primordial chemistry (FiBY project)
- Consider metal line cooling based on the equilibrium state with the UV background (FiBY project)
- NEW: Add models to calculate the radiative feedback from young stars and kinetic feedback from massive black holes and the growth/destruction of dust grains (FOREVER22 project)

Input: FOREVER22

Table 1. Parameters of zoom-in cosmological hydrodynamic simulations: (1) $M_{\rm h}$ is the halo mass at the final redshift ($z_{\rm end}$). (2) $m_{\rm gas}$ is the initial mass of gas particles. (3) $m_{\rm DM}$ is the dark matter particle mass. (4) $\epsilon_{\rm min}$ is the gravitational softening length in comoving units.

Halo ID	$M_{\rm h}$ ($\rm M_\odot\ h^{-1}$) at $z_{\rm end}$ ($z = 0, 3$)	$m_{\rm gas}$ ($\rm M_\odot\ h^{-1}$)	$m_{\rm DM}$ ($\rm M_\odot\ h^{-1}$)	$\epsilon_{\rm min}$ ($\rm kpc\ h^{-1}$)	$z_{\rm end}$
PCR0	1.9×10^{14} (1.4×10^{15}, 8.1×10^{13})	2.9×10^{6}	1.6×10^{7}	2.0	2

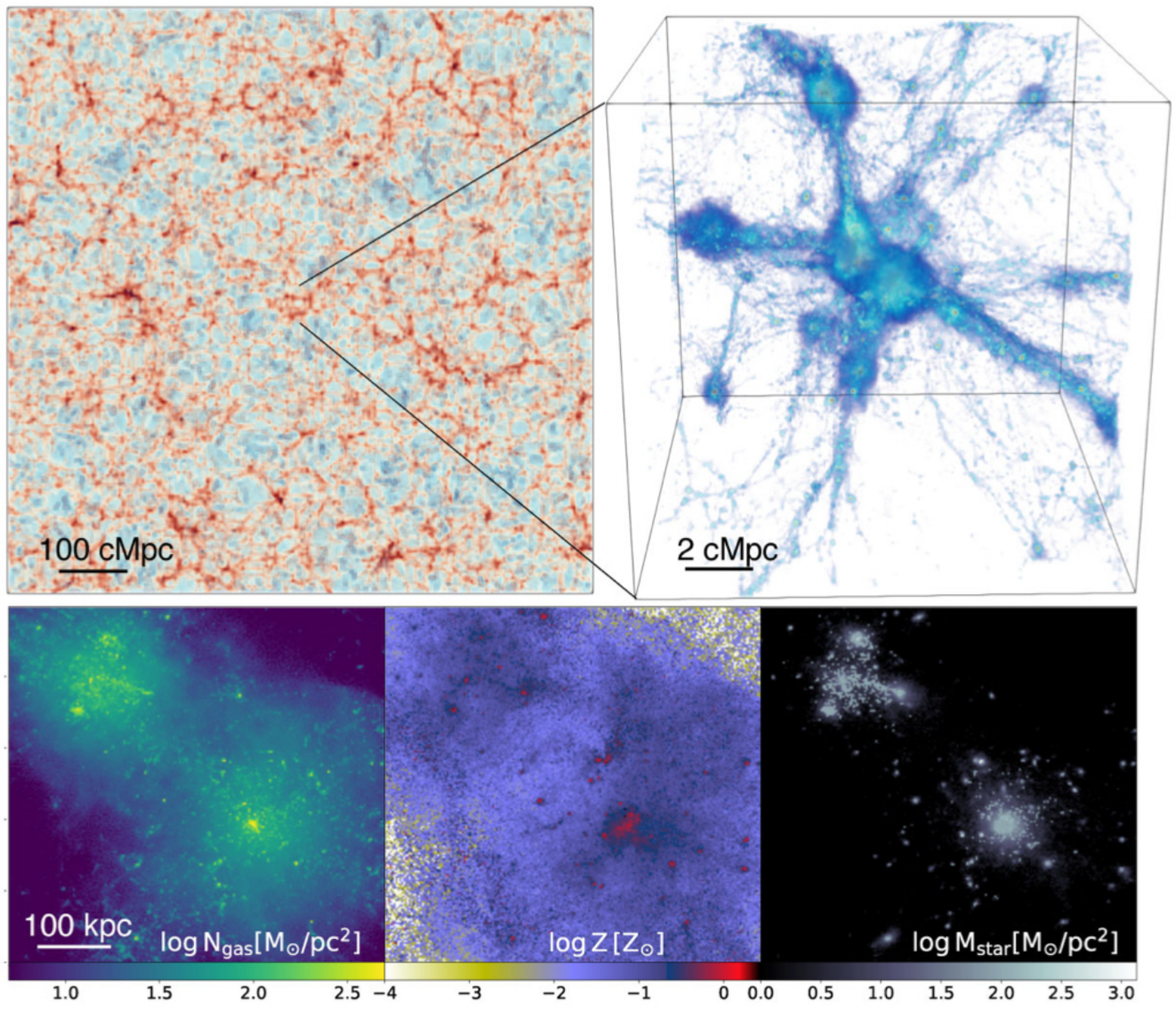

Figure 2. Upper left-hand panel: The large scale structure of matter in the entire calculation box with $L = 714$ cMpc. Upper right-hand panel: 3D gas structure of the PCR0 region at $z = 3$. Lower panels: Gas column density (left-hand panel), density-weighted metallicity (middle), and stellar surface density (right-hand panel) of the most massive halo in PCR0.

Input: FOREVER22

Table 1. Parameters of zoom-in cosmological hydrodynamic simulations: (1) $M_{\rm h}$ is the halo mass at the final redshift ($z_{\rm end}$). (2) $m_{\rm gas}$ is the initial mass of gas particles. (3) $m_{\rm DM}$ is the dark matter particle mass. (4) $\epsilon_{\rm min}$ is the gravitational softening length in comoving units.

Halo ID	$M_{\rm h}$ ($\rm M_\odot\ h^{-1}$) at $z_{\rm end}$ ($z = 0, 3$)	$m_{\rm gas}$ ($\rm M_\odot\ h^{-1}$)	$m_{\rm DM}$ ($\rm M_\odot\ h^{-1}$)	$\epsilon_{\rm min}$ ($\rm kpc\ h^{-1}$)	$z_{\rm end}$
PCR0	1.9×10^{14} (1.4×10^{15}, 8.1×10^{13})	2.9×10^{6}	1.6×10^{7}	2.0	2
PCR1	1.5×10^{14} (1.2×10^{15}, 5.9×10^{13})	2.9×10^{6}	1.6×10^{7}	2.0	2
PCR2	1.2×10^{14} (5.2×10^{14}, 5.6×10^{13})	2.9×10^{6}	1.6×10^{7}	2.0	2
PCR3	1.2×10^{14} (8.1×10^{14}, 2.0×10^{13})	2.9×10^{6}	1.6×10^{7}	2.0	2
PCR4	1.1×10^{14} (1.1×10^{15}, $\times 10^{13}$)	2.9×10^{6}	1.6×10^{7}	2.0	2
PCR5	1.0×10^{14} (6.7×10^{14}, 3.5×10^{13})	2.9×10^{6}	1.6×10^{7}	2.0	2
PCR6	9.9×10^{13} (5.9×10^{14}, 4.6×10^{13})	2.9×10^{6}	1.6×10^{7}	2.0	2
PCR7	9.6×10^{13} (6.3×10^{14}, 3.3×10^{13})	2.9×10^{6}	1.6×10^{7}	2.0	2
PCR8	9.1×10^{13} (5.6×10^{14}, 5.1×10^{13})	2.9×10^{6}	1.6×10^{7}	2.0	2
PCR9	9.1×10^{13} (1.2×10^{15}, 2.0×10^{13})	2.9×10^{6}	1.6×10^{7}	2.0	2

Code: ART2

“All-wavelength Radiative Transfer with Adaptive Refinement Tree” (Yajima et al. 2012, Li et al. 2008)

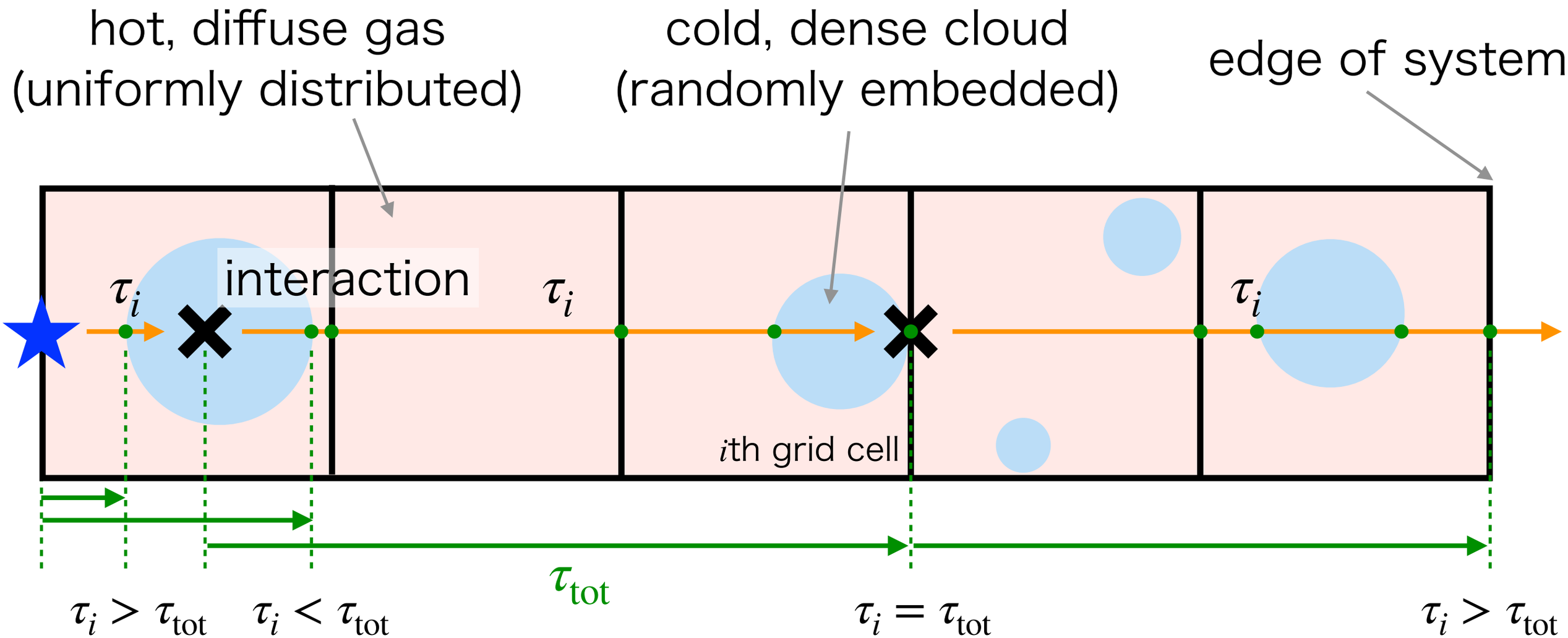

Luminosity v.s. Halo Mass

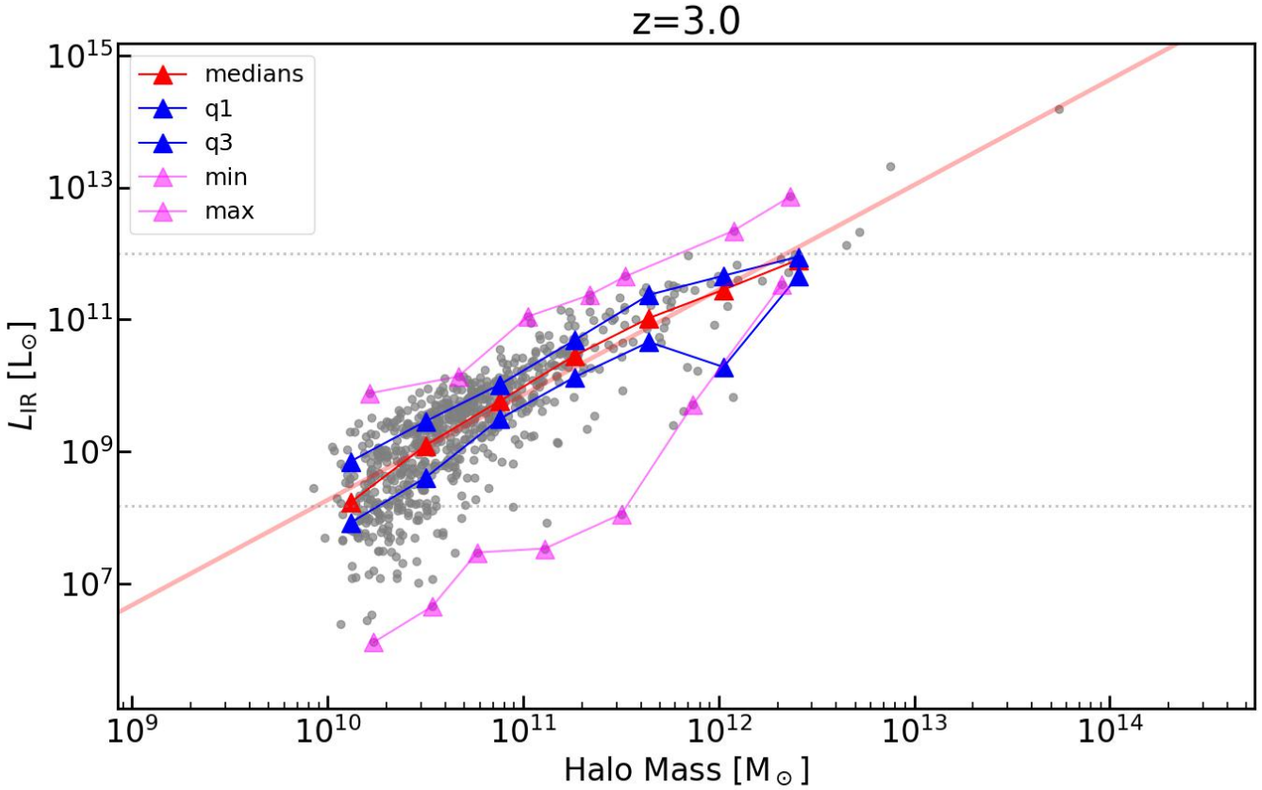

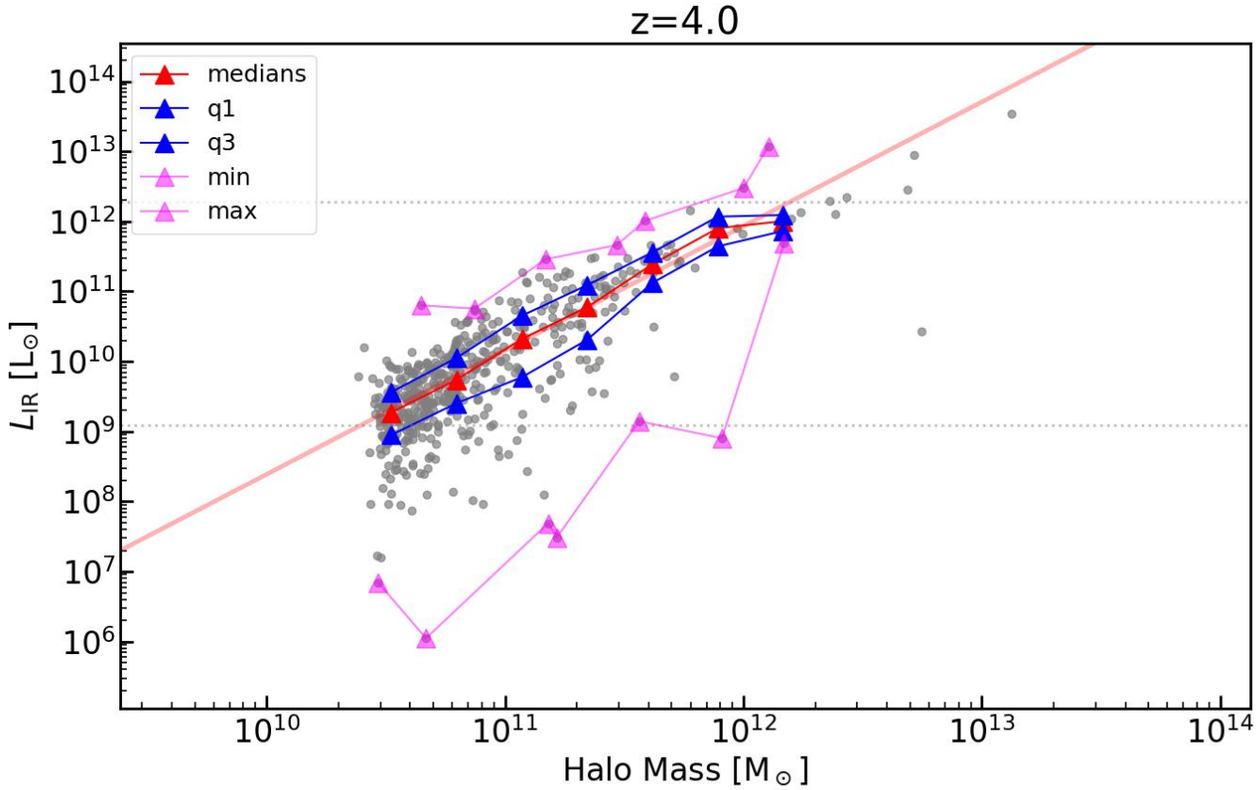

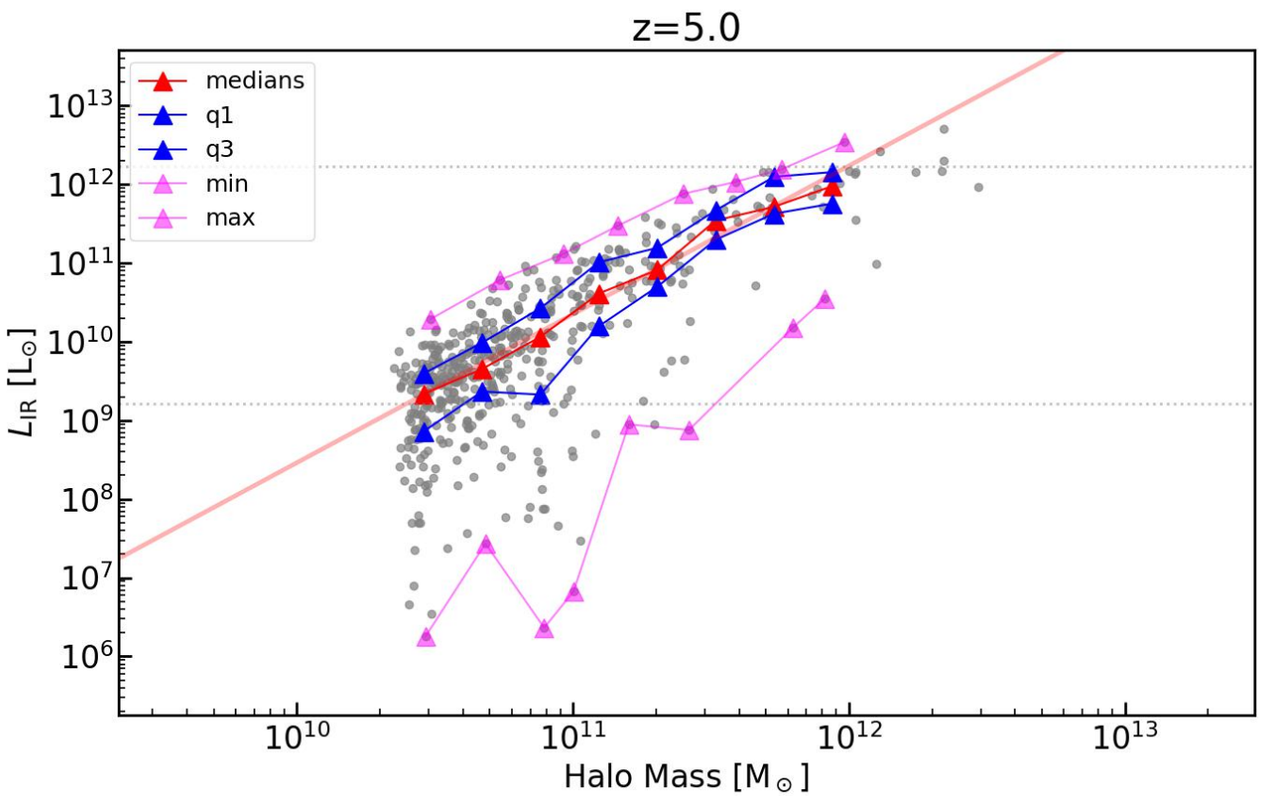

Luminosity v.s. Halo Mass

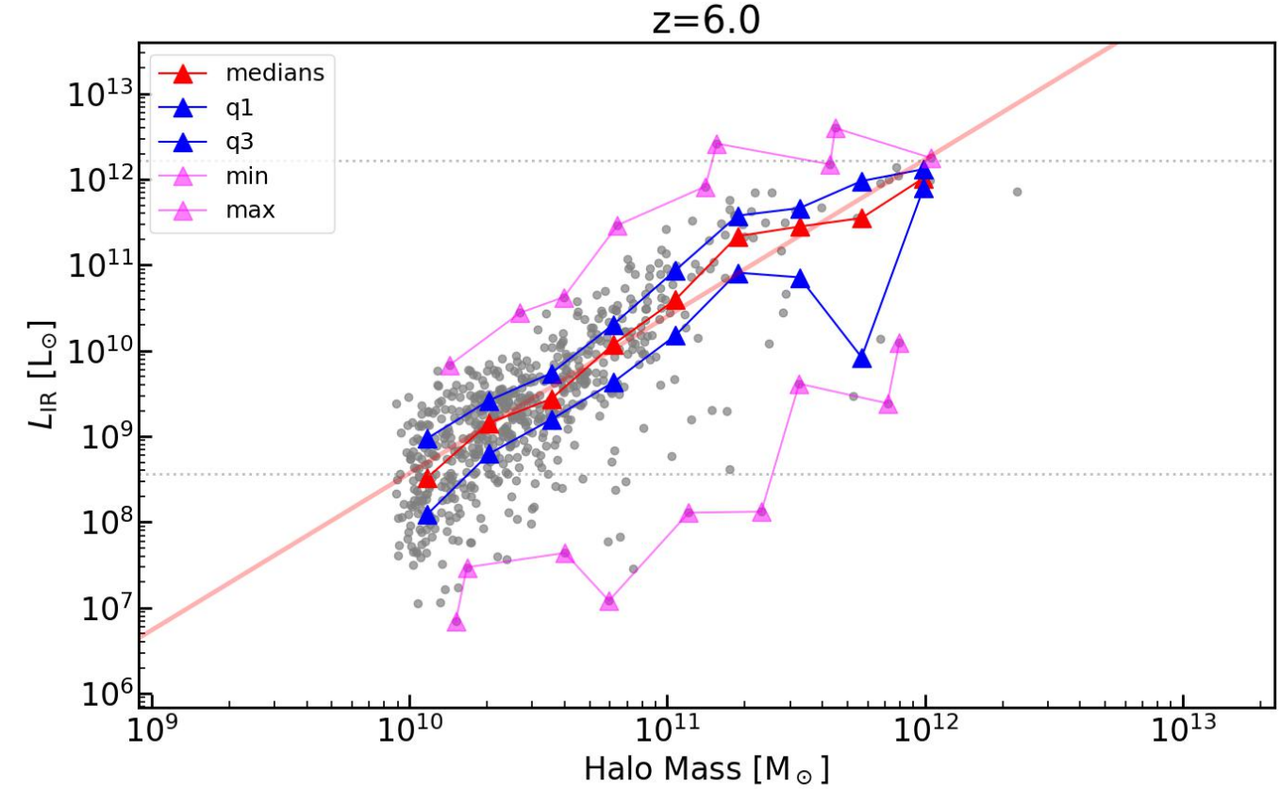

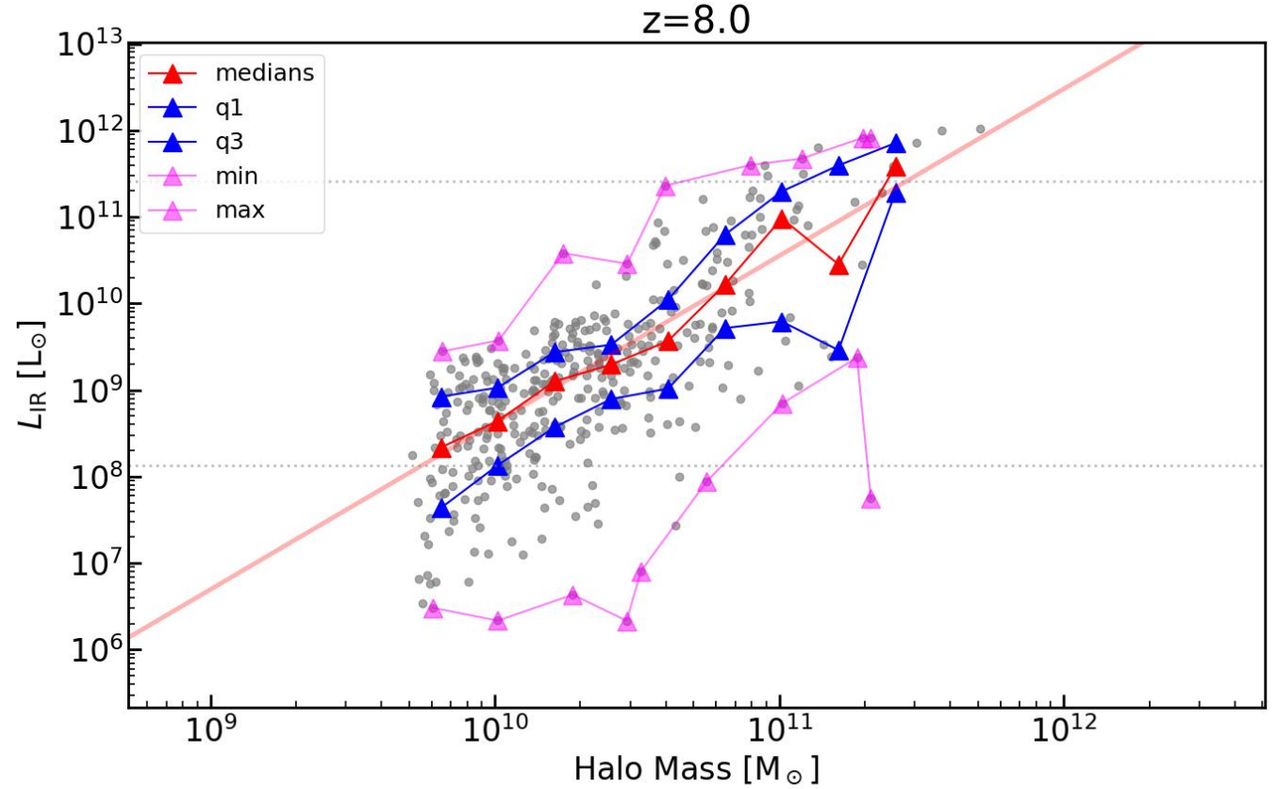

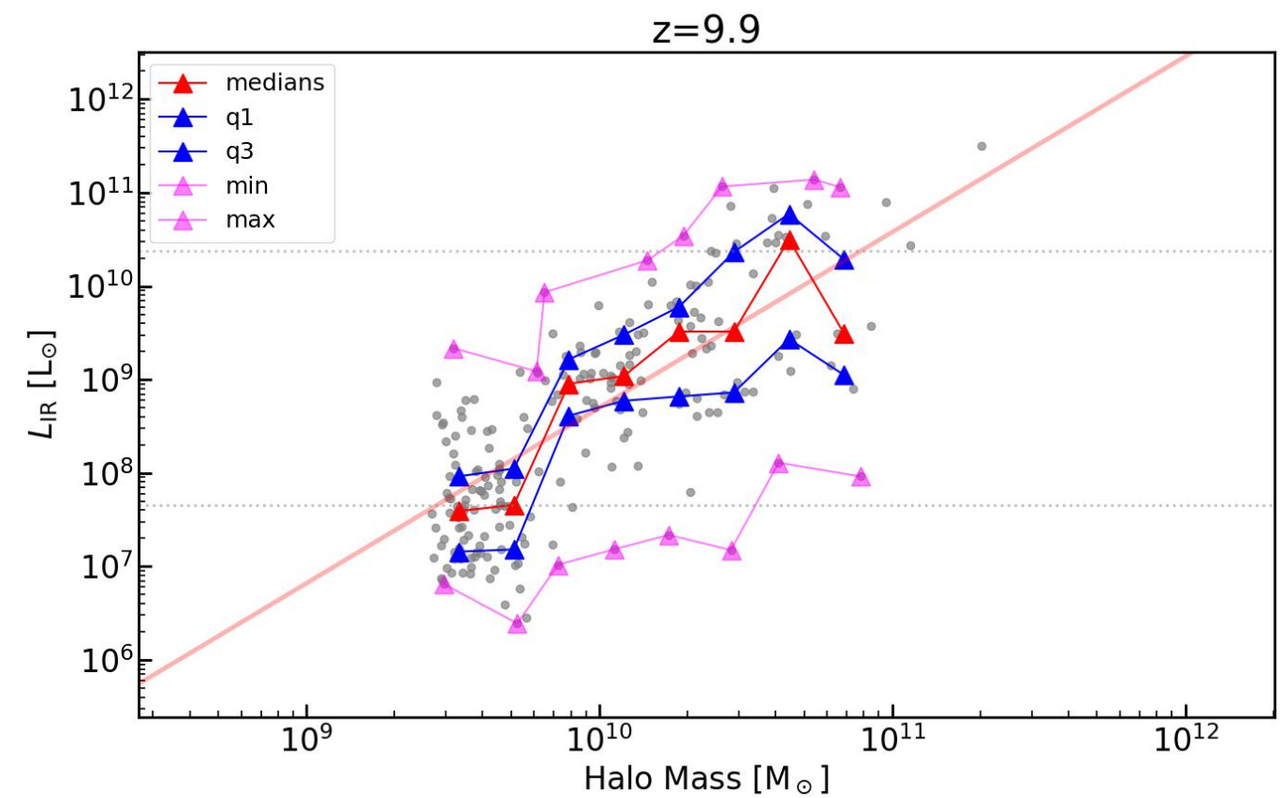

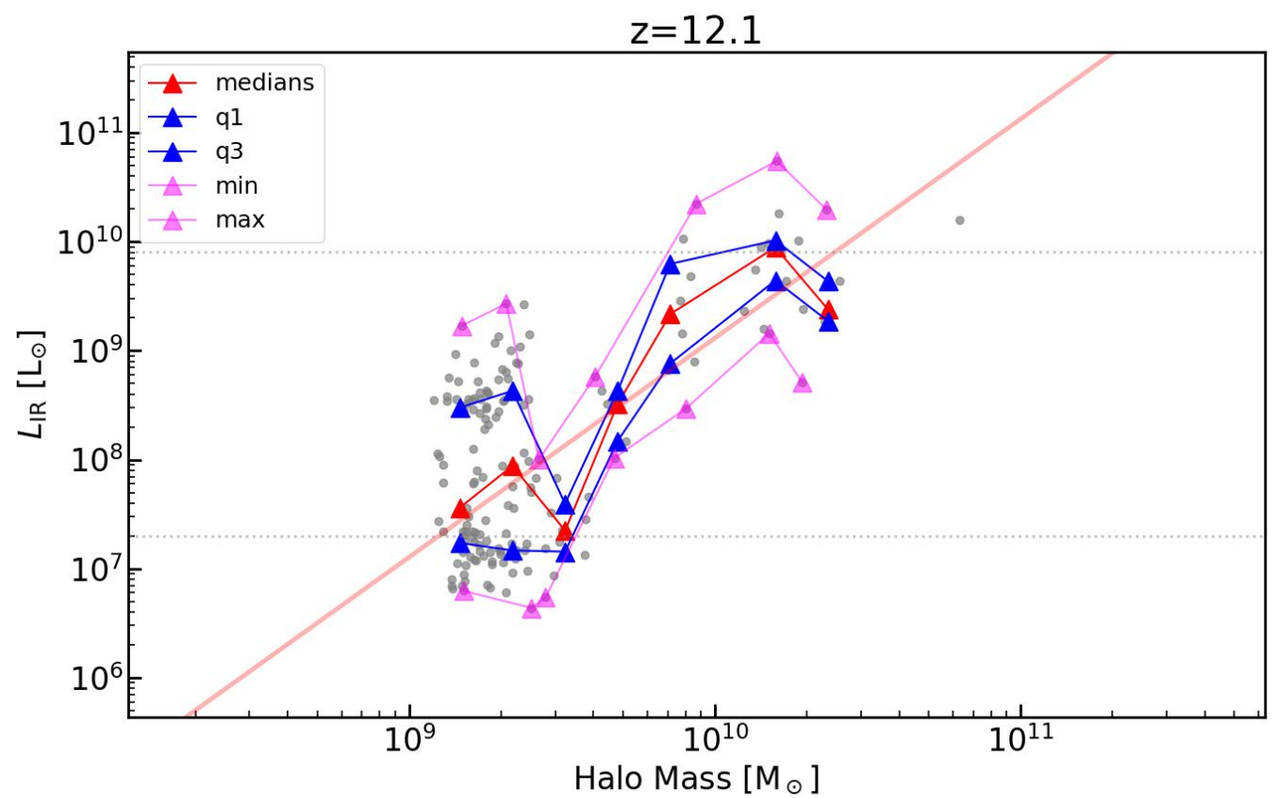

Dust Temperature v.s. IR Luminosity

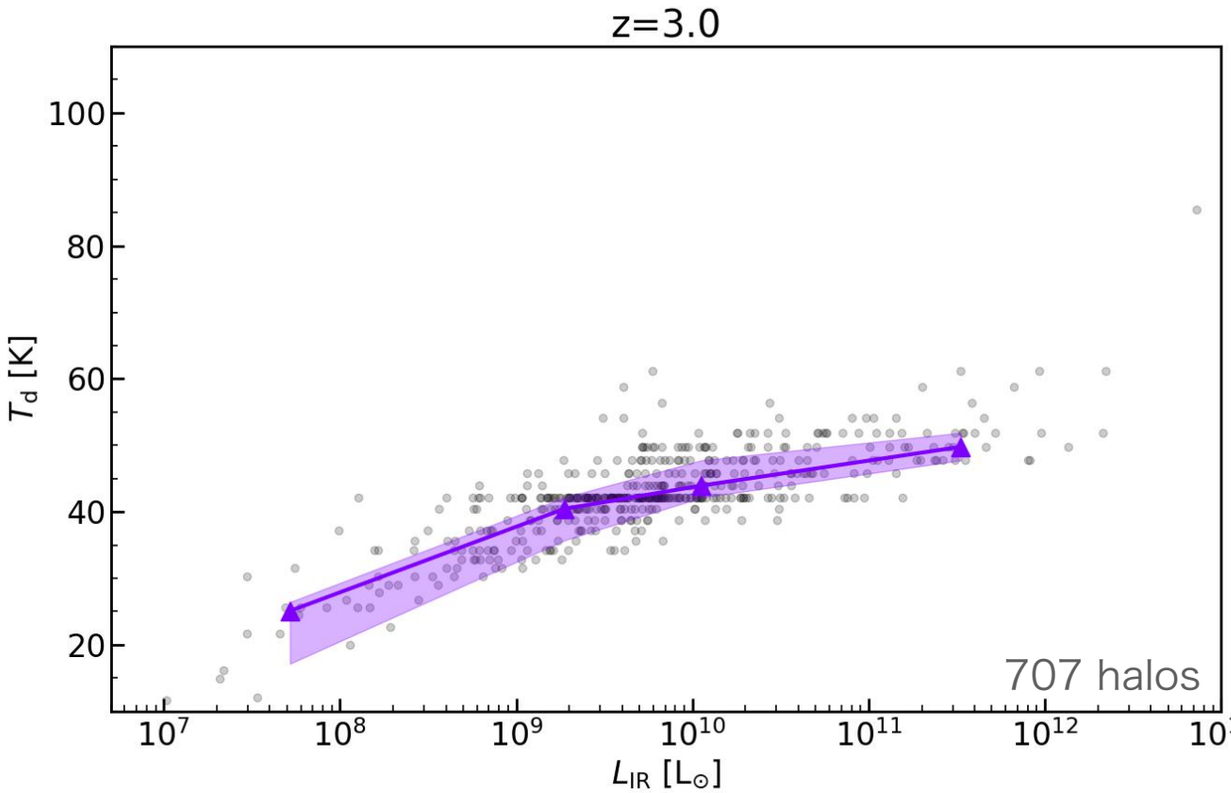

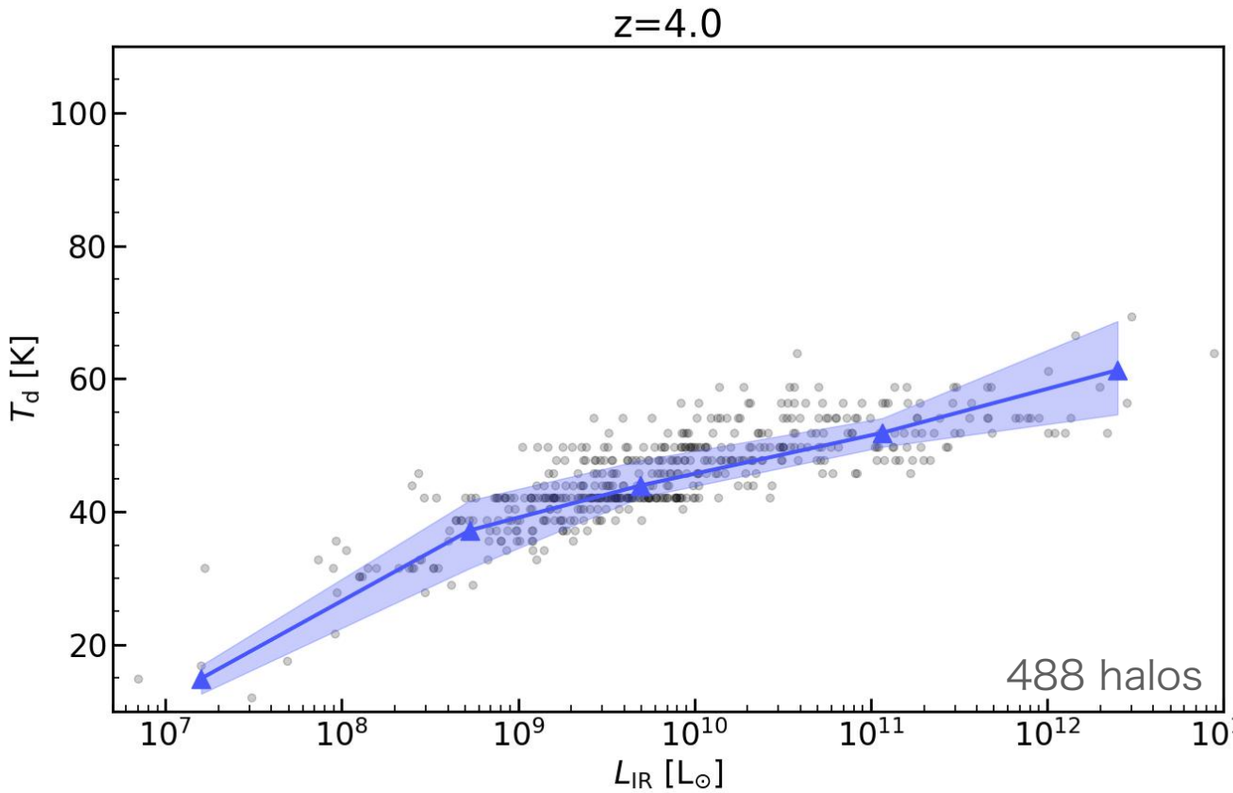

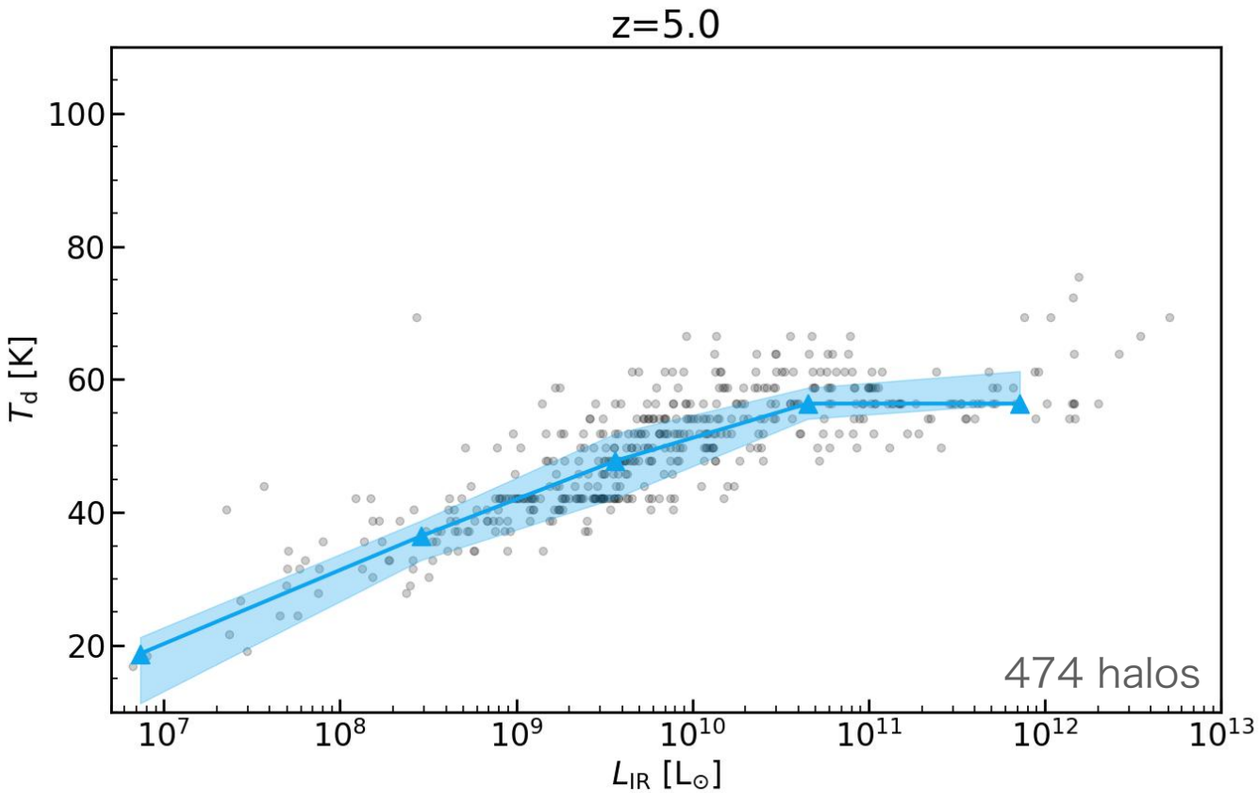

Dust Temperature v.s. IR Luminosity

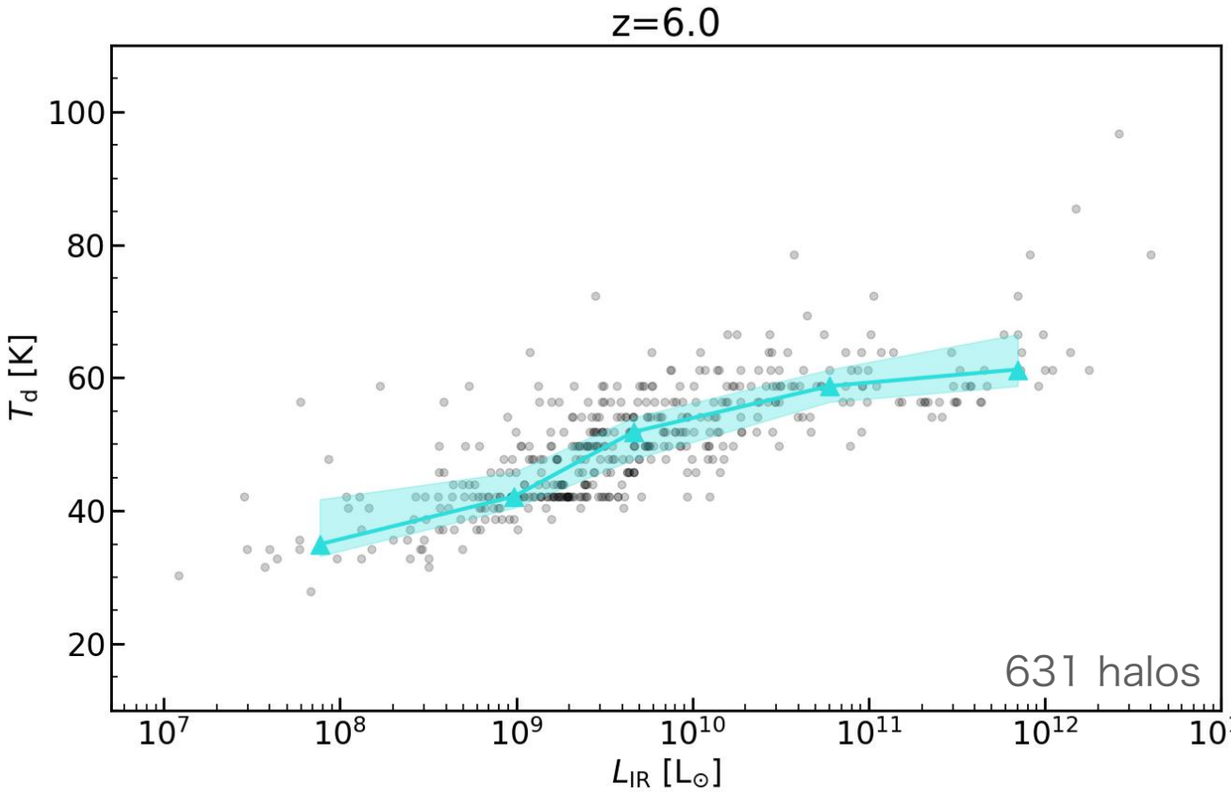

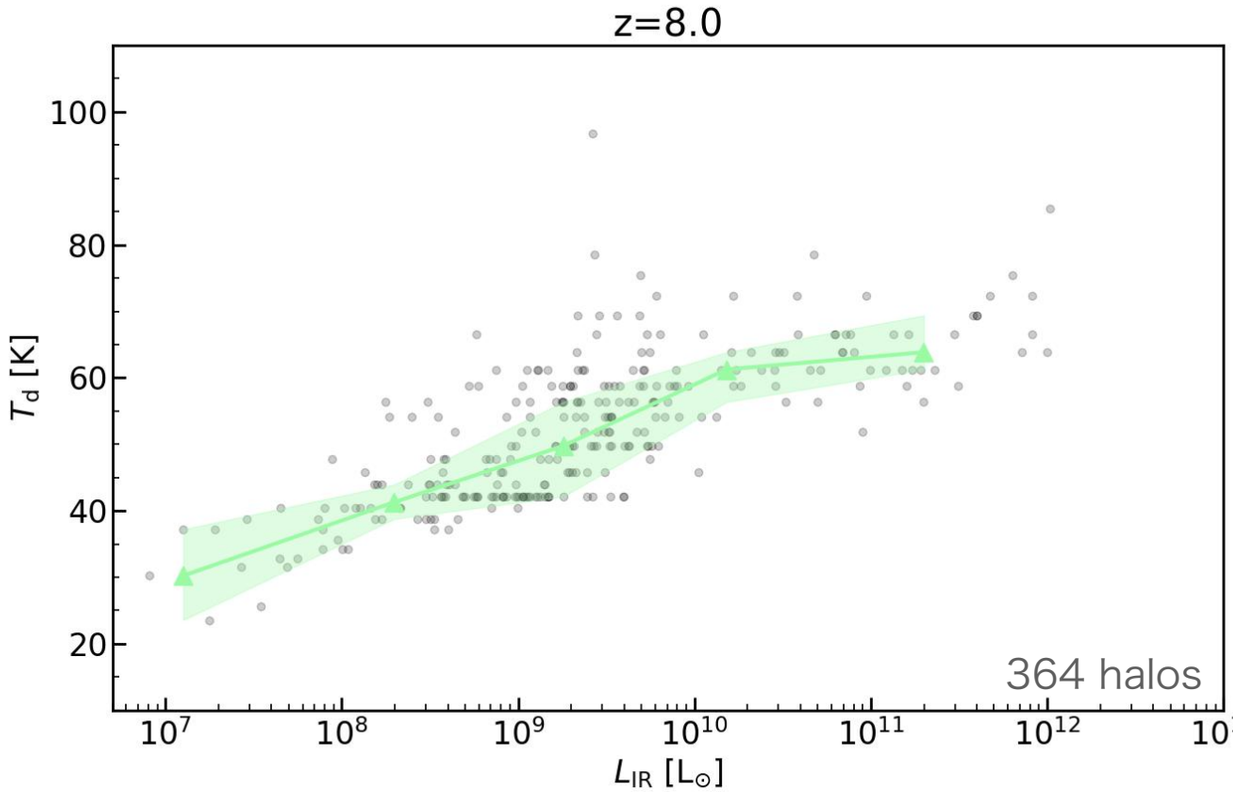

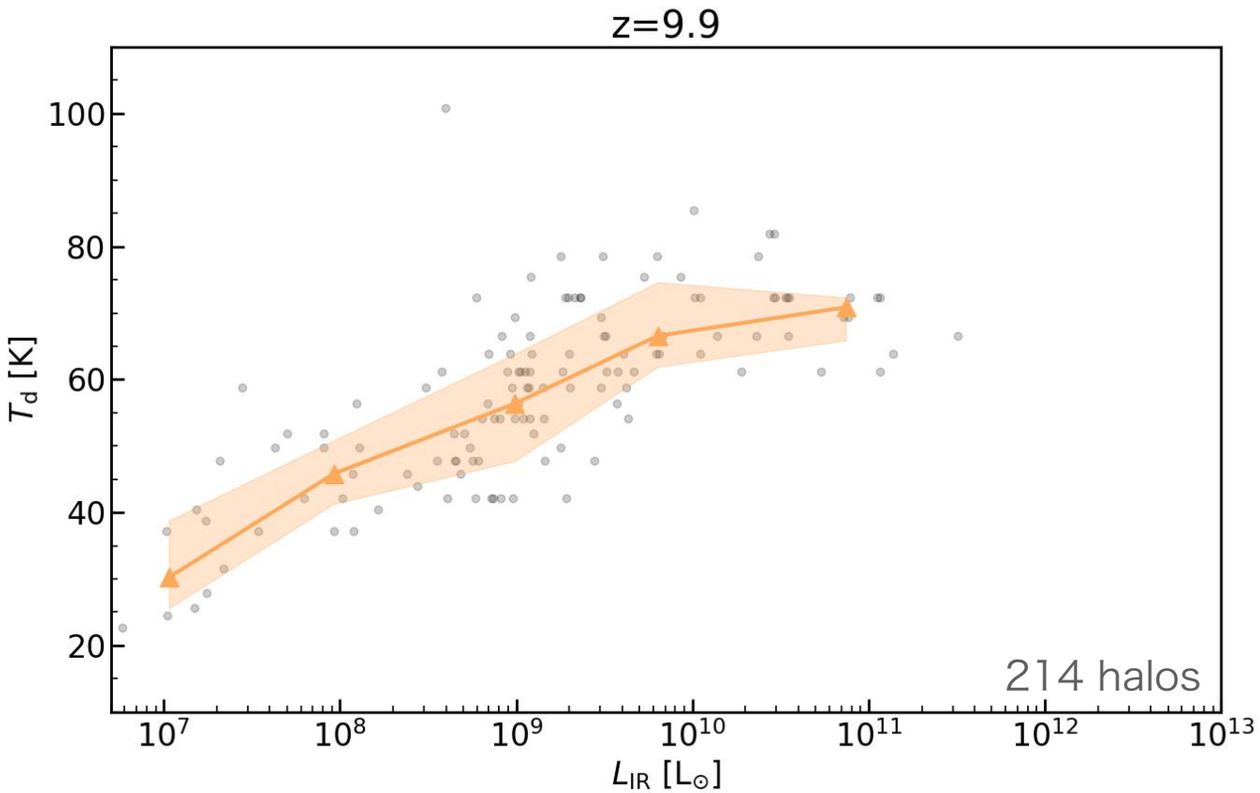

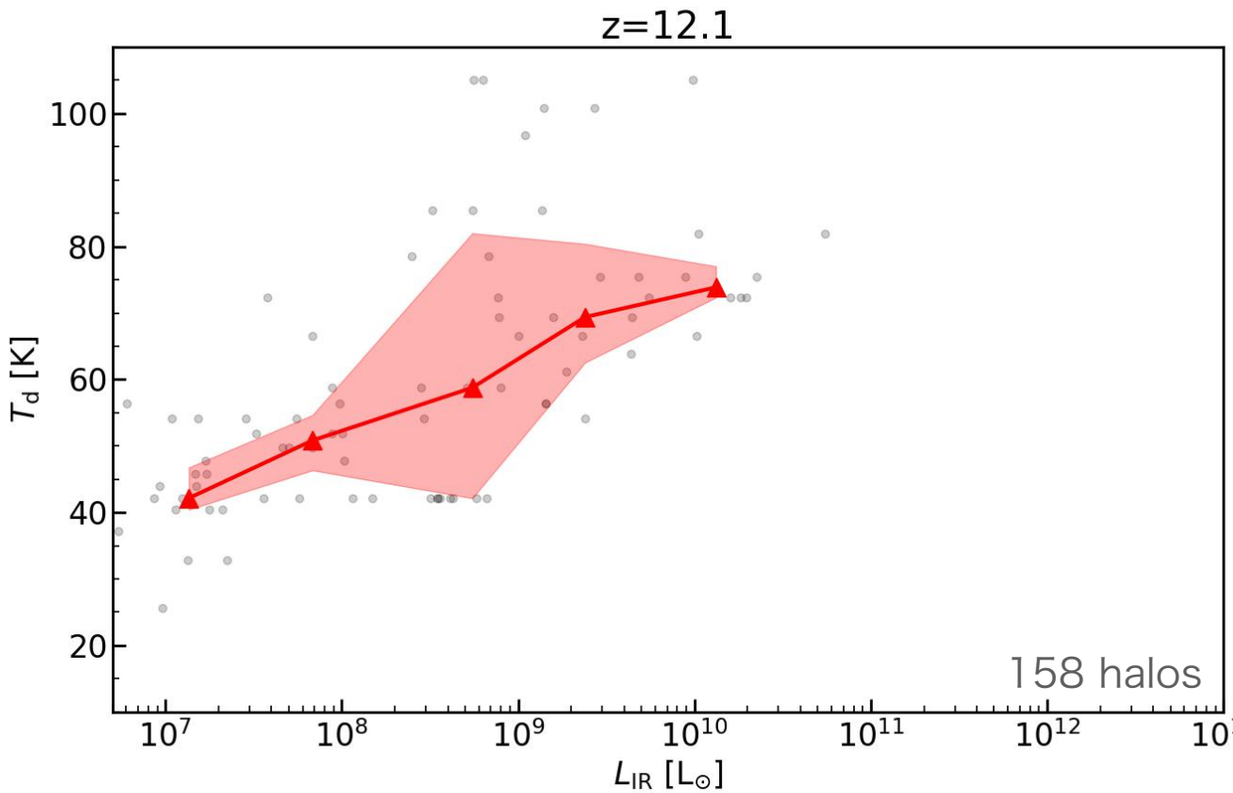

Dust Temperature v.s. SFR

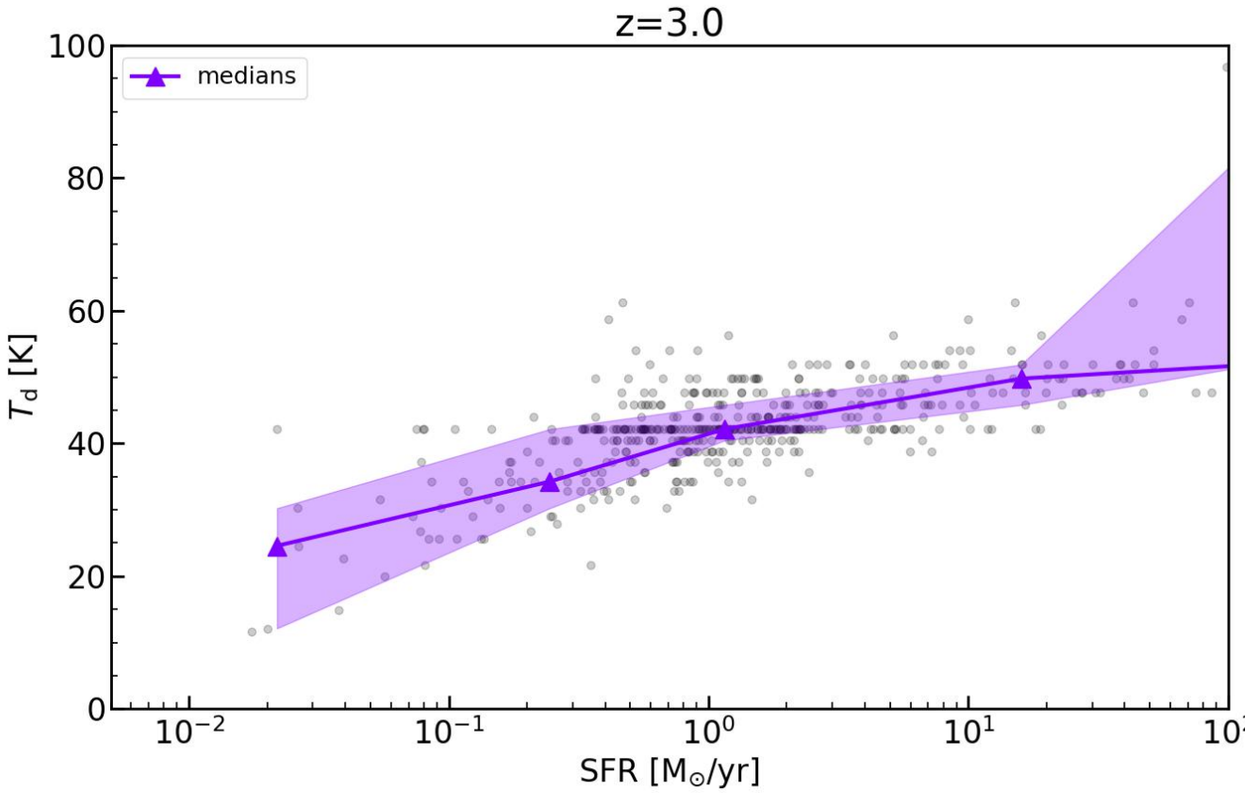

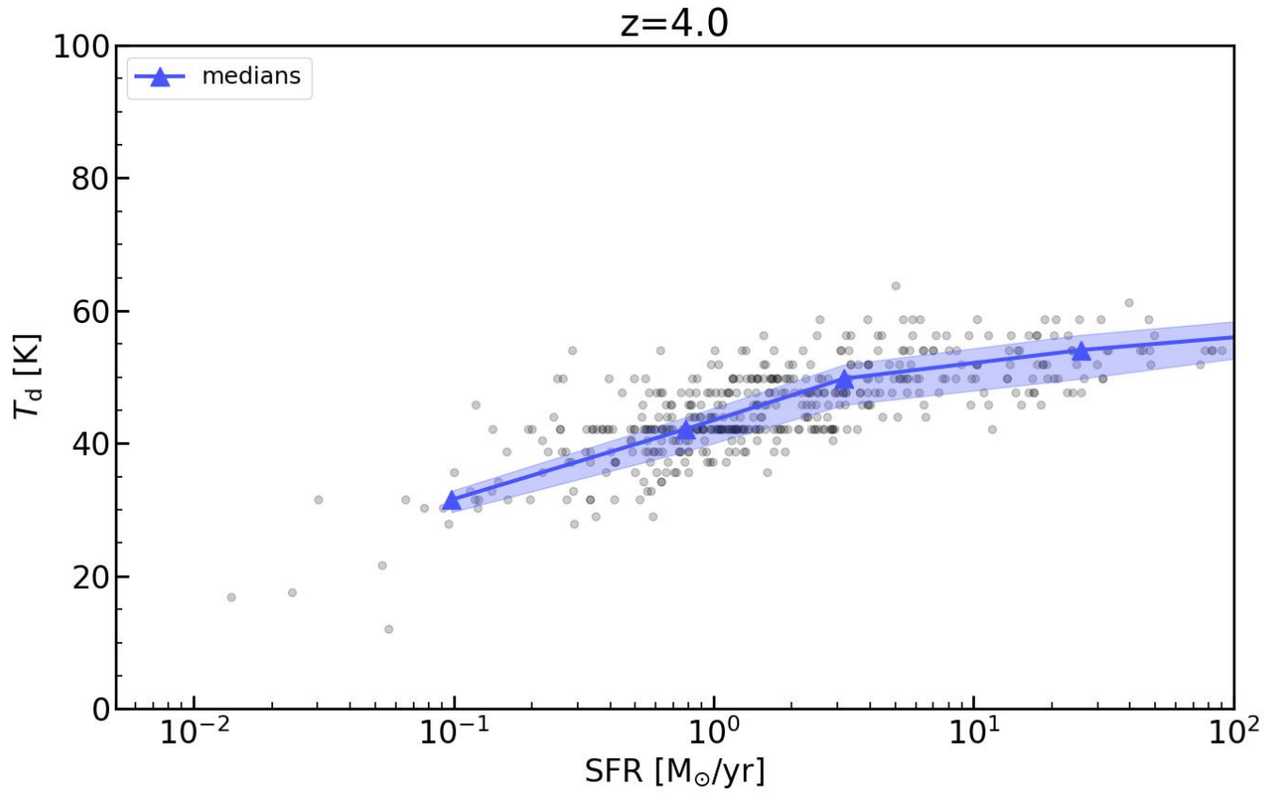

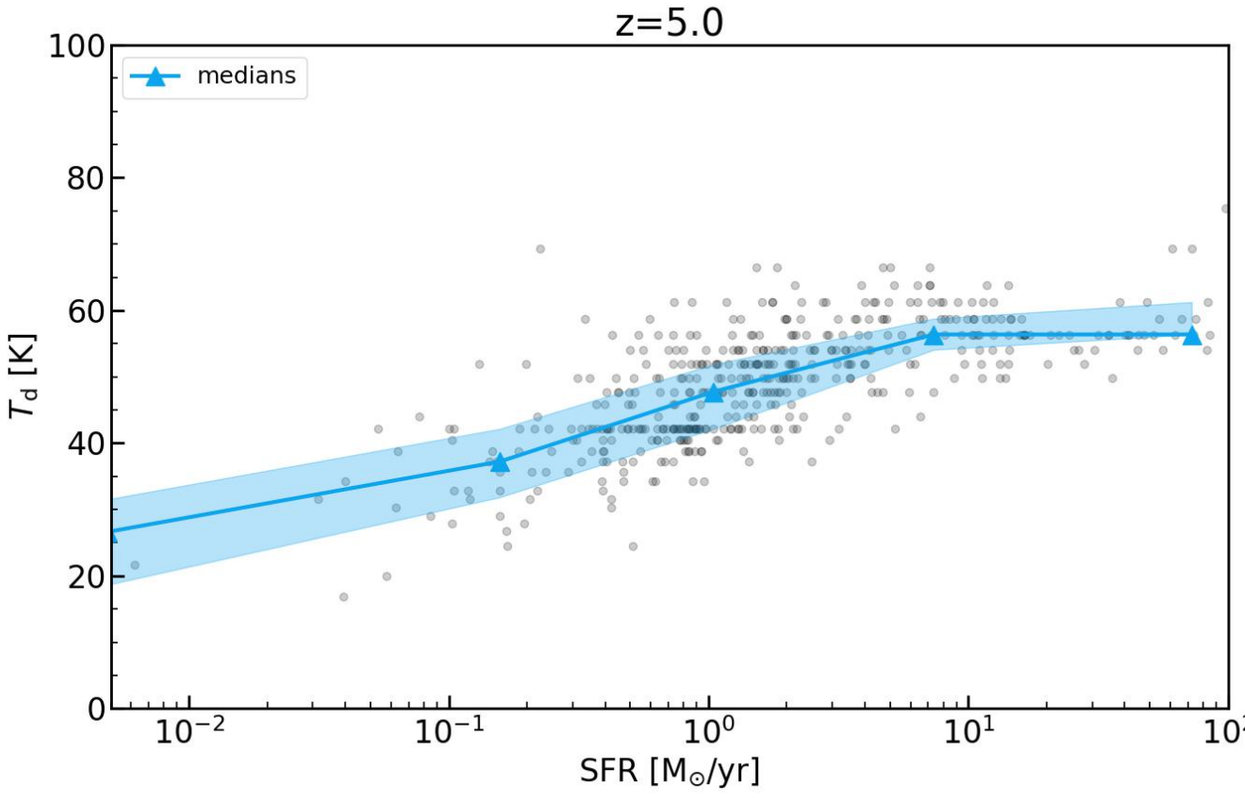

Dust Temperature v.s. SFR

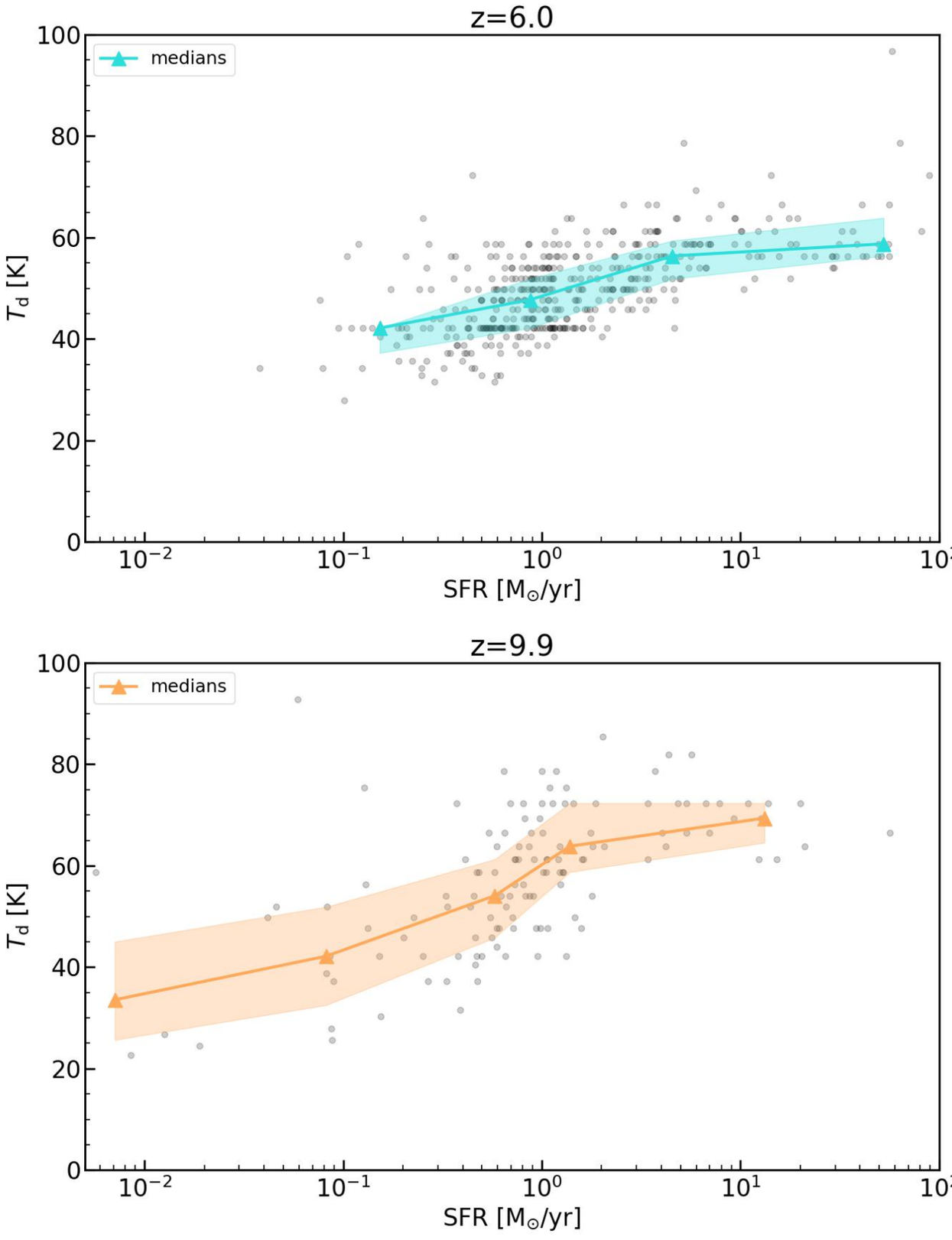

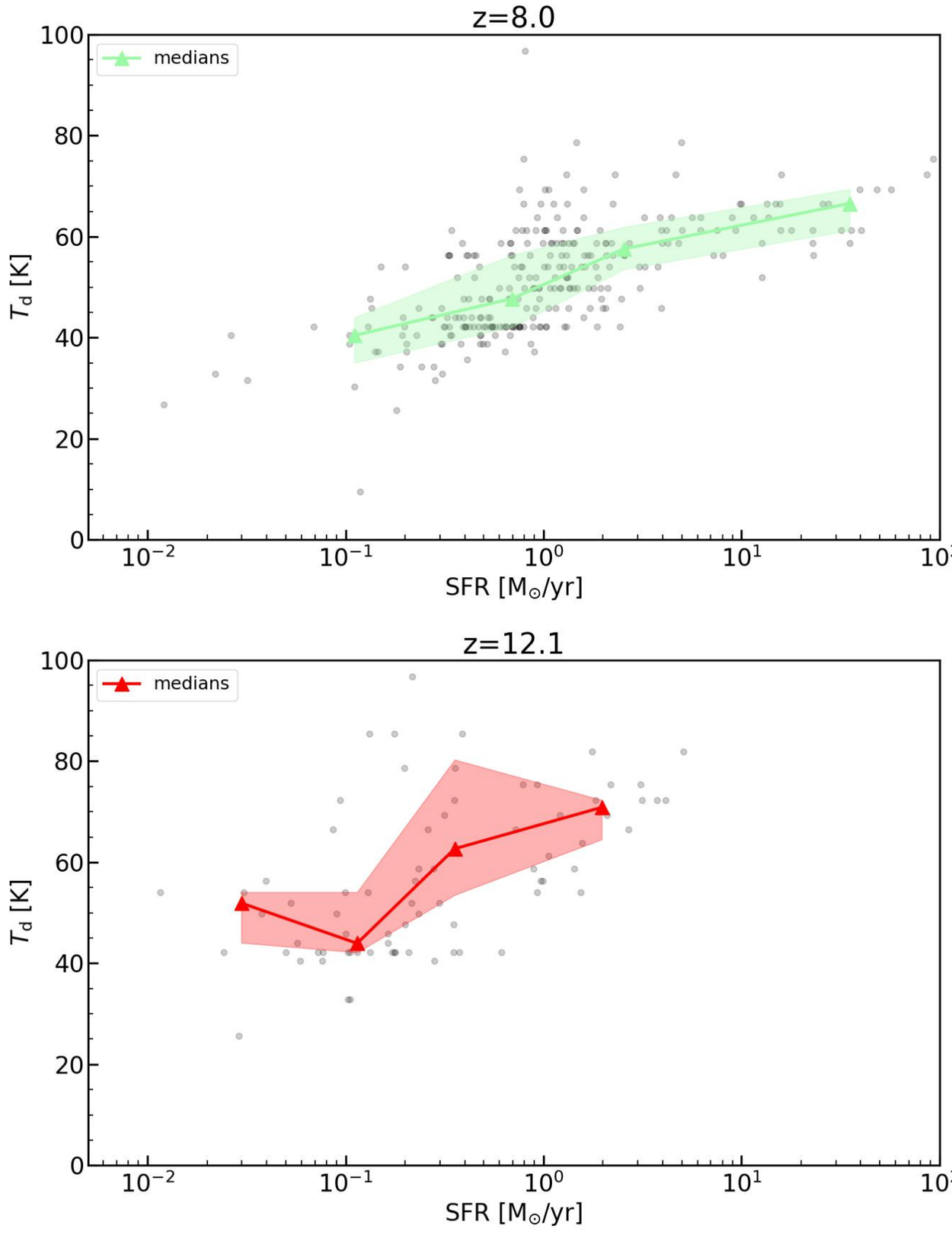

Half-light Radius

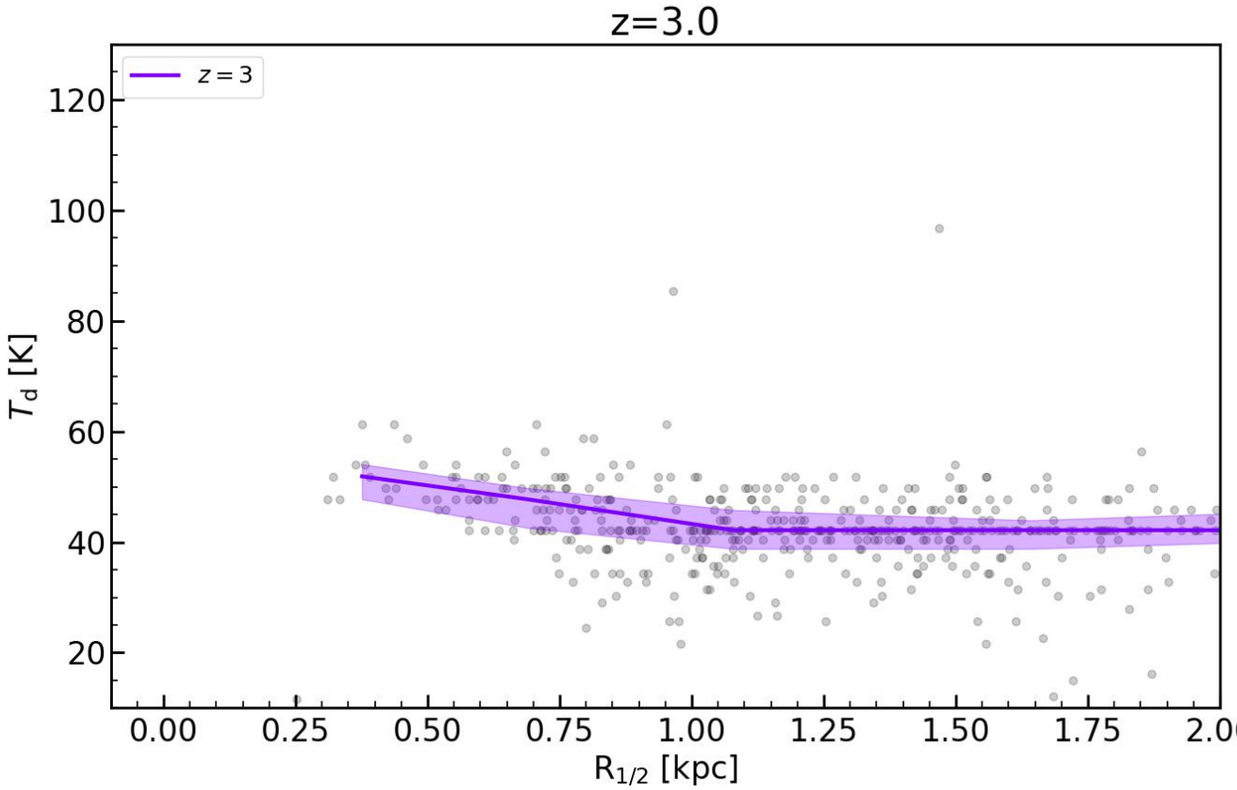

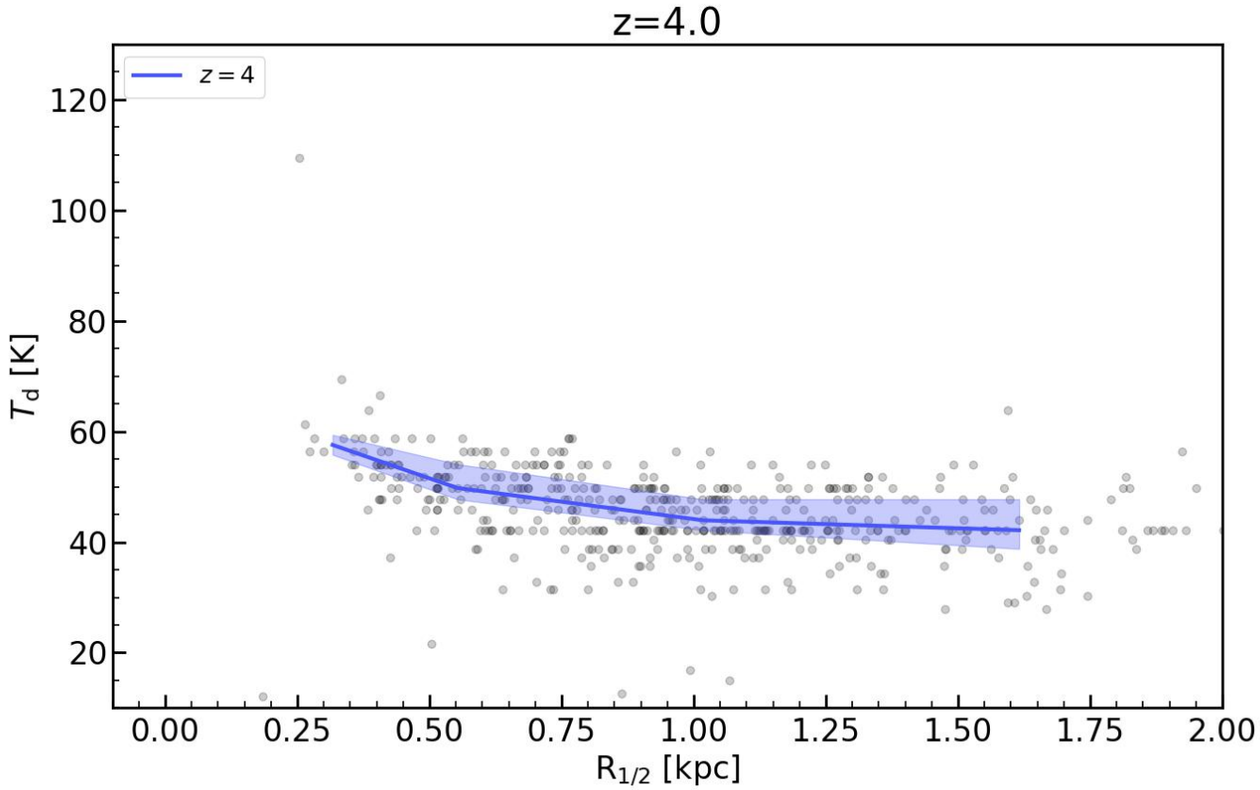

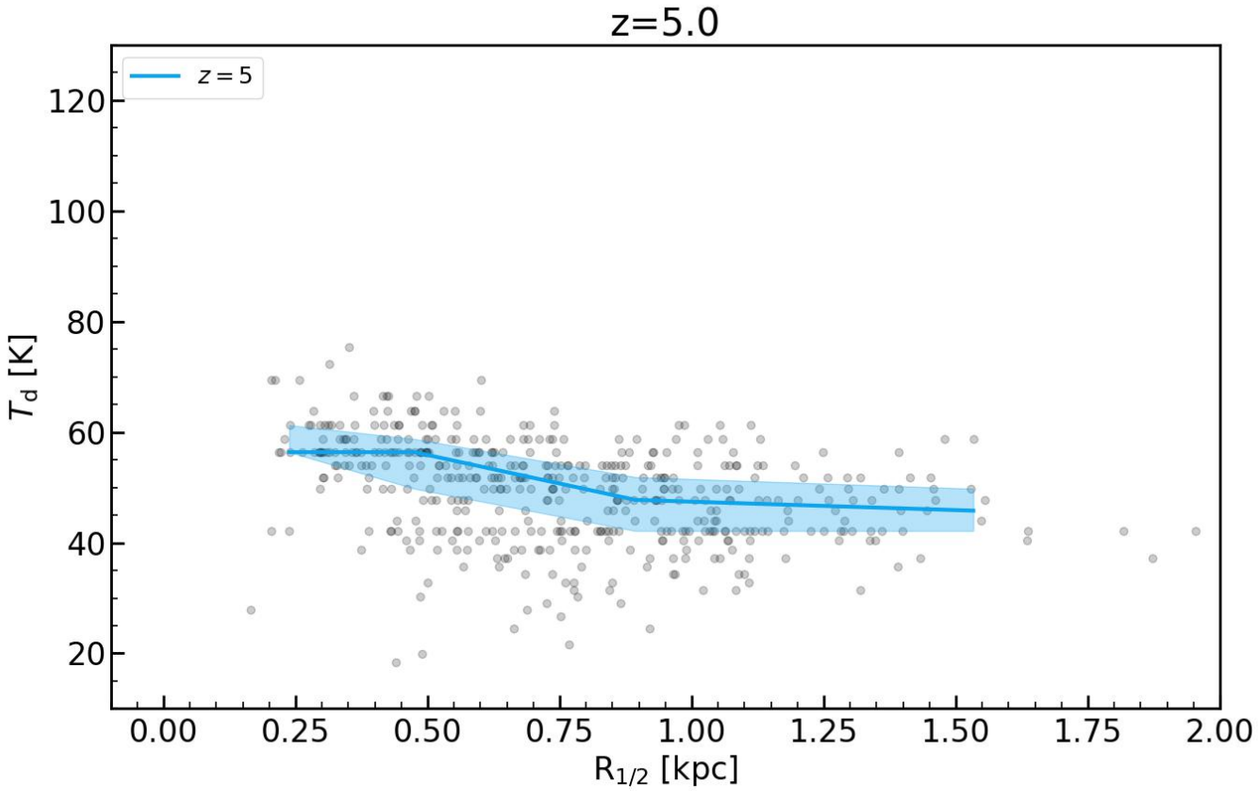

Half-light Radius

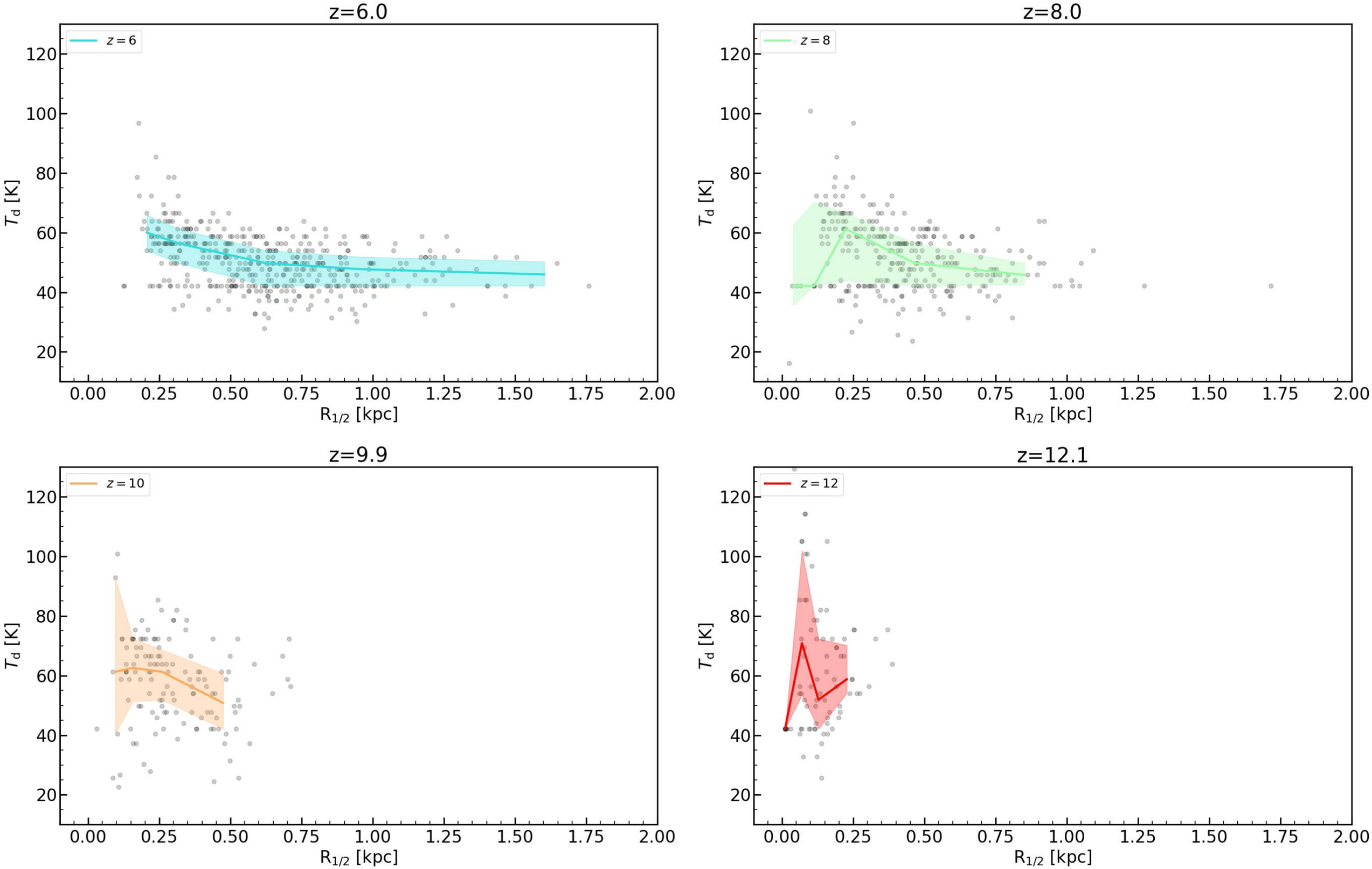

Half-light Radius

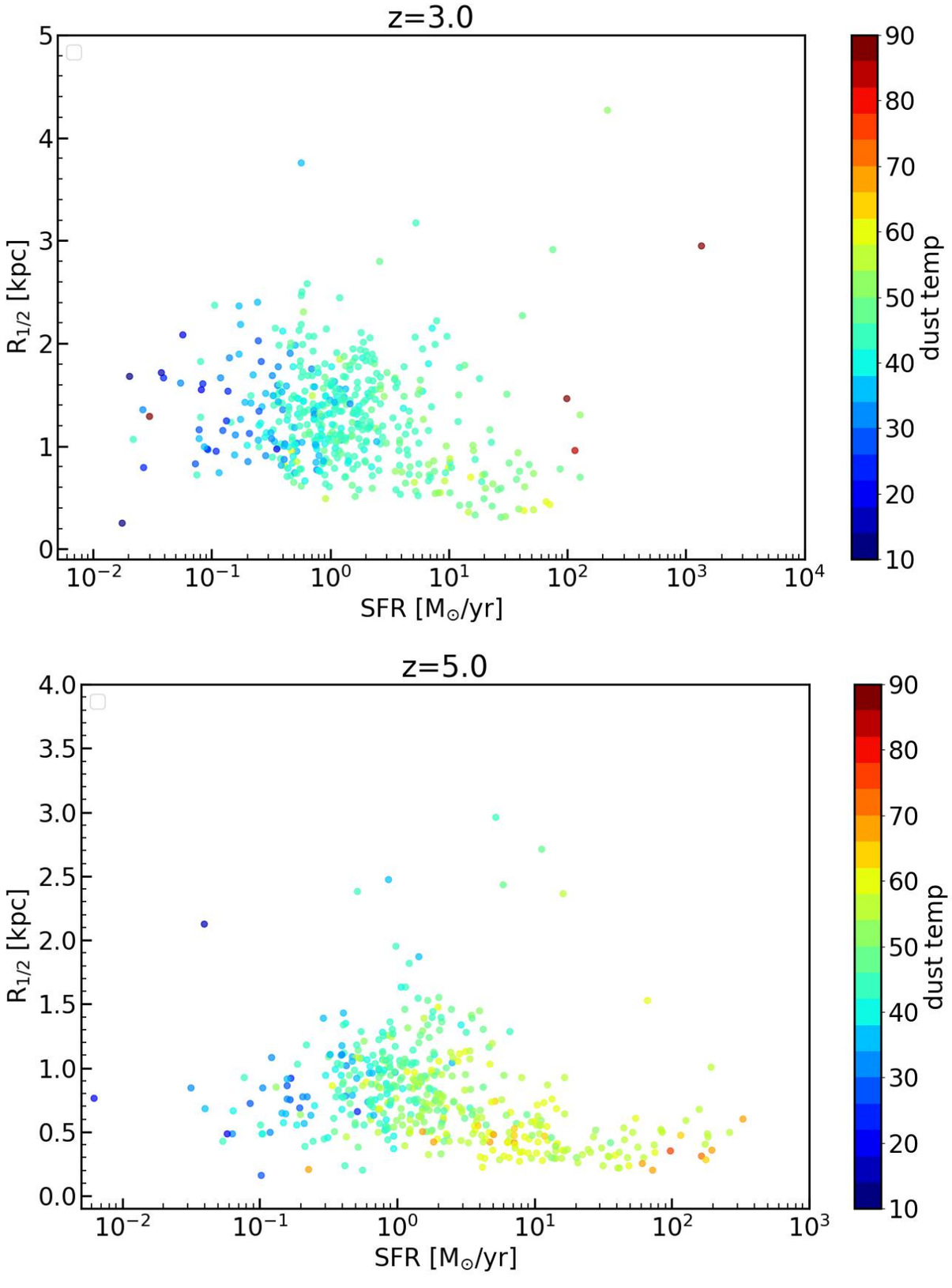

Half-light Radius

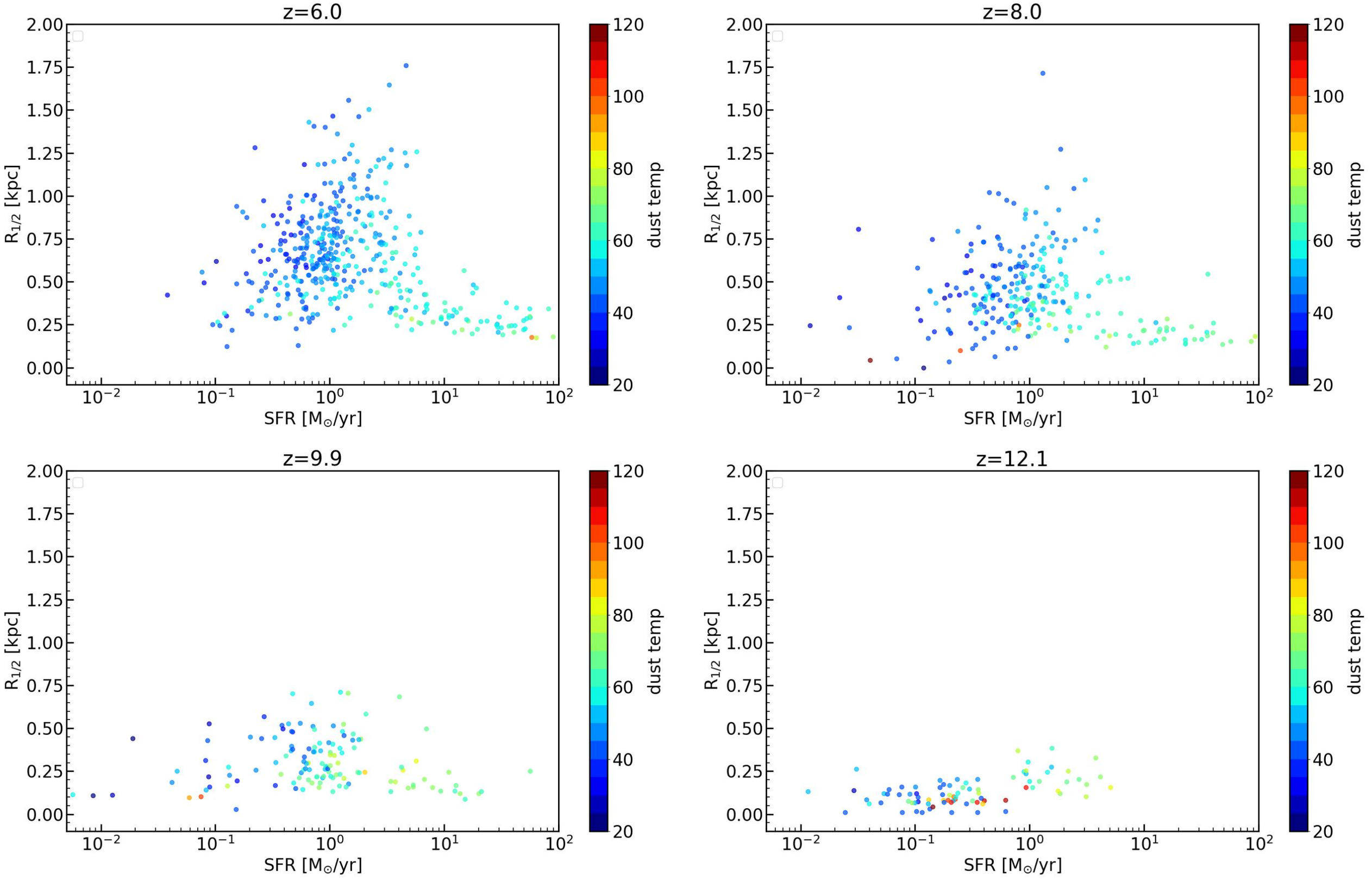

Half-light Radius

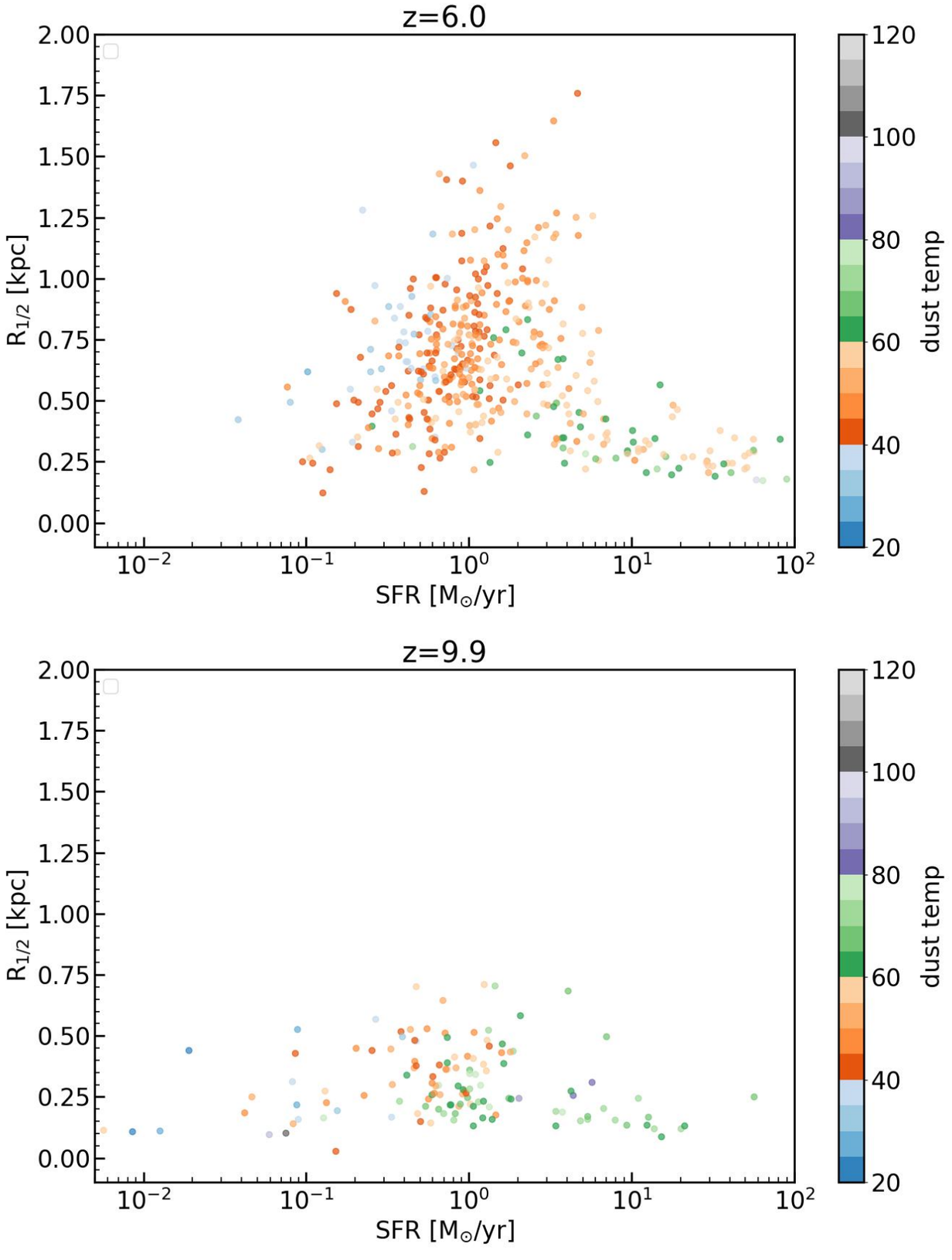

IR Luminosity v.s. SFR

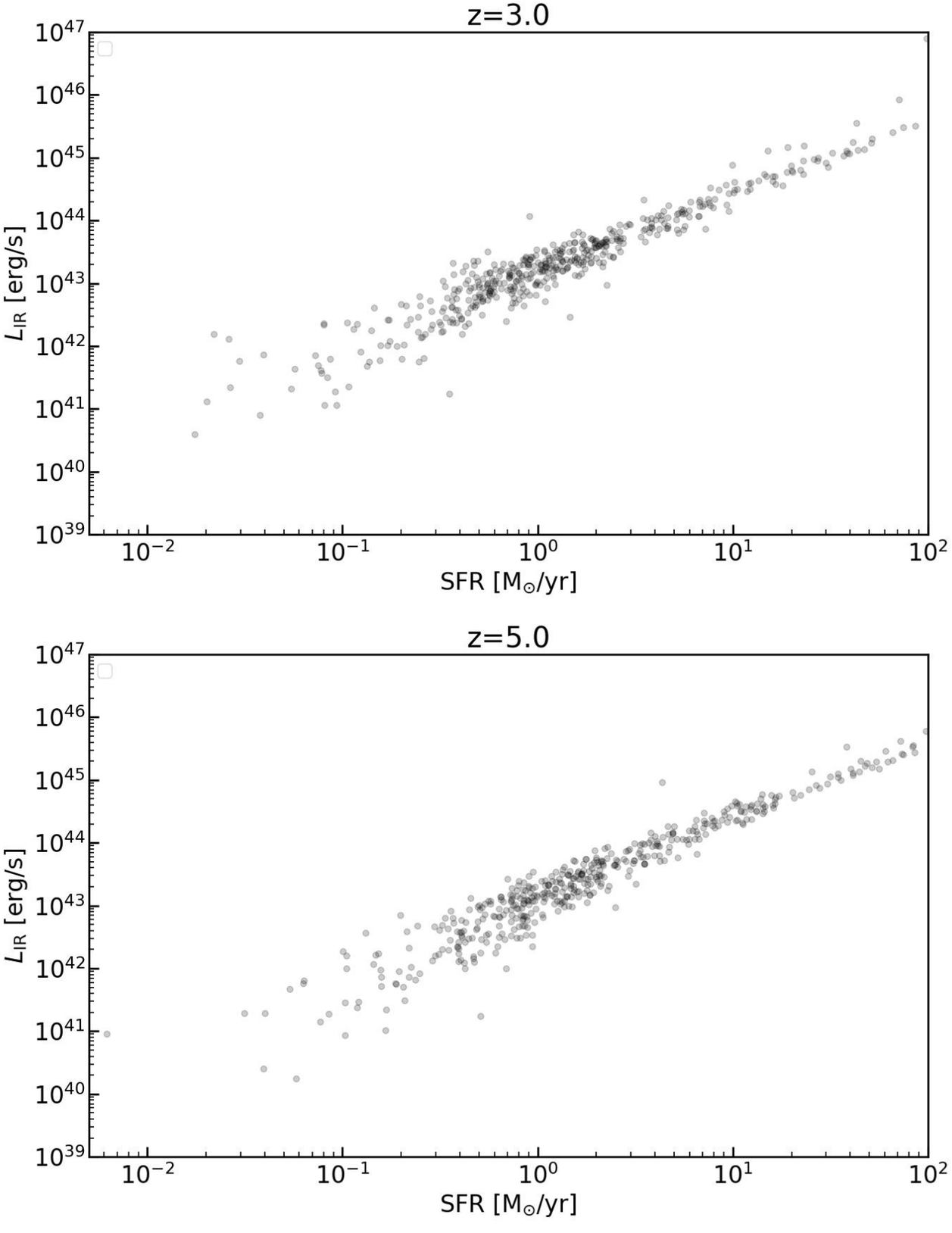

IR Luminosity v.s. SFR

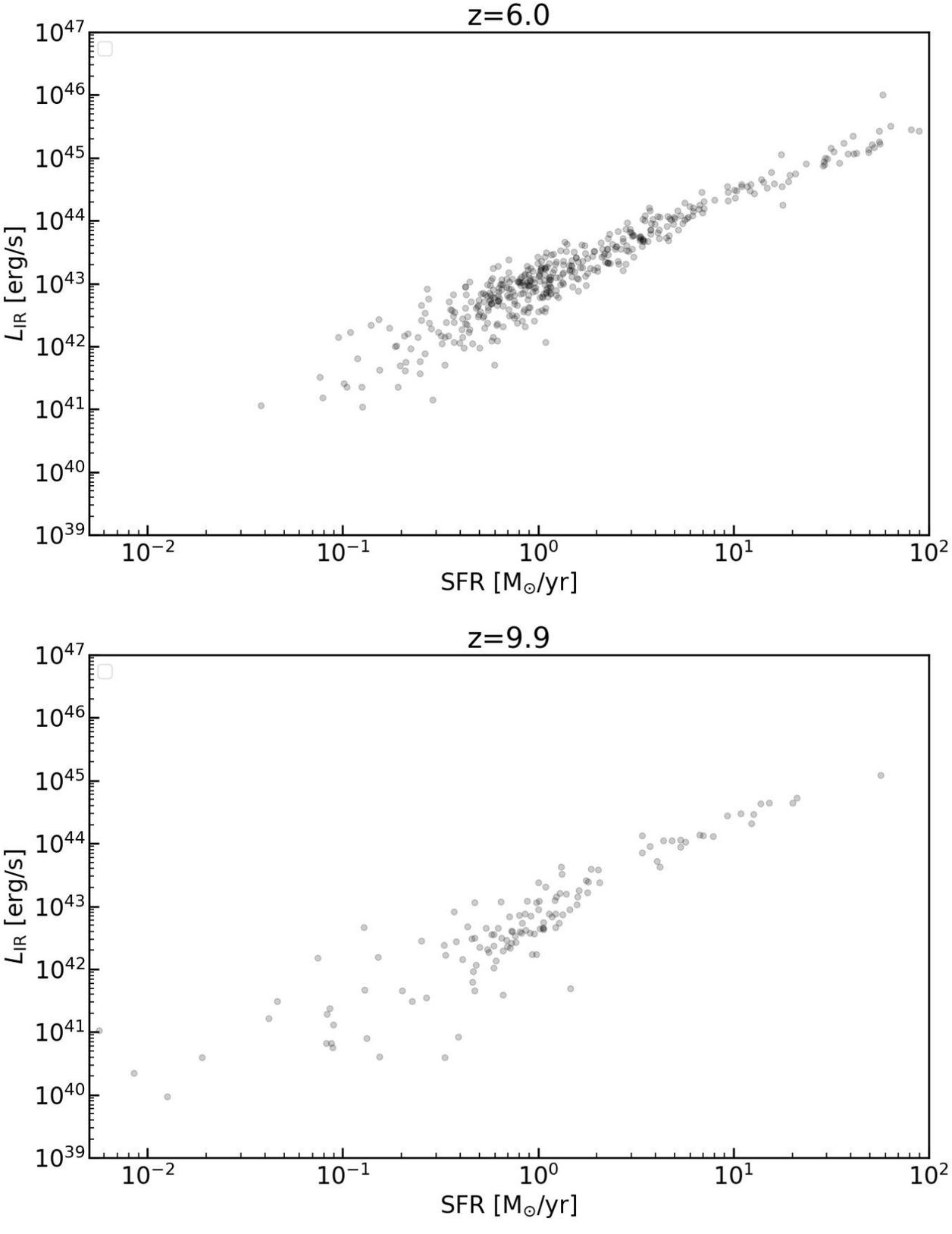

Escape Fraction

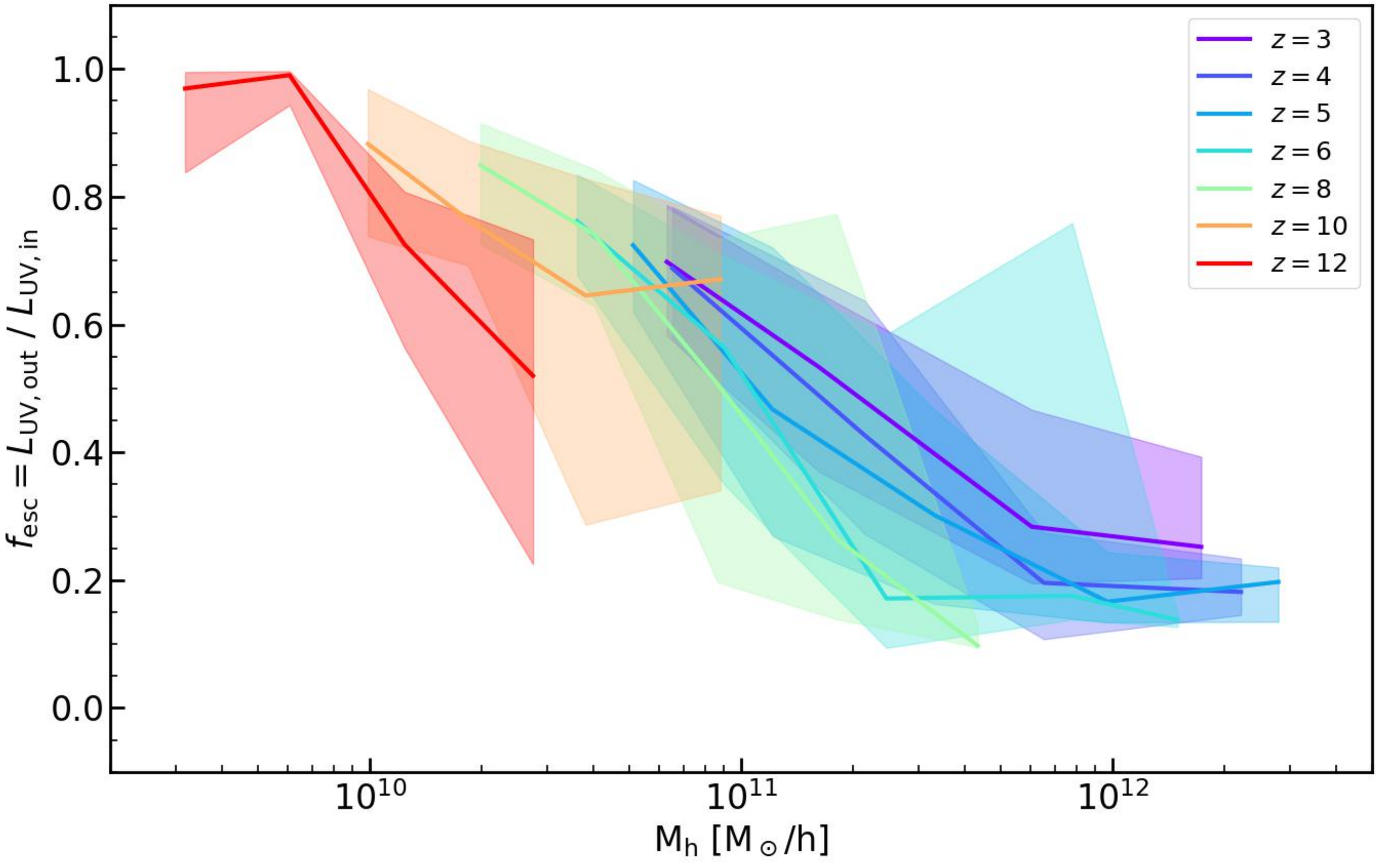

Escape Fraction v.s. Halo Mass

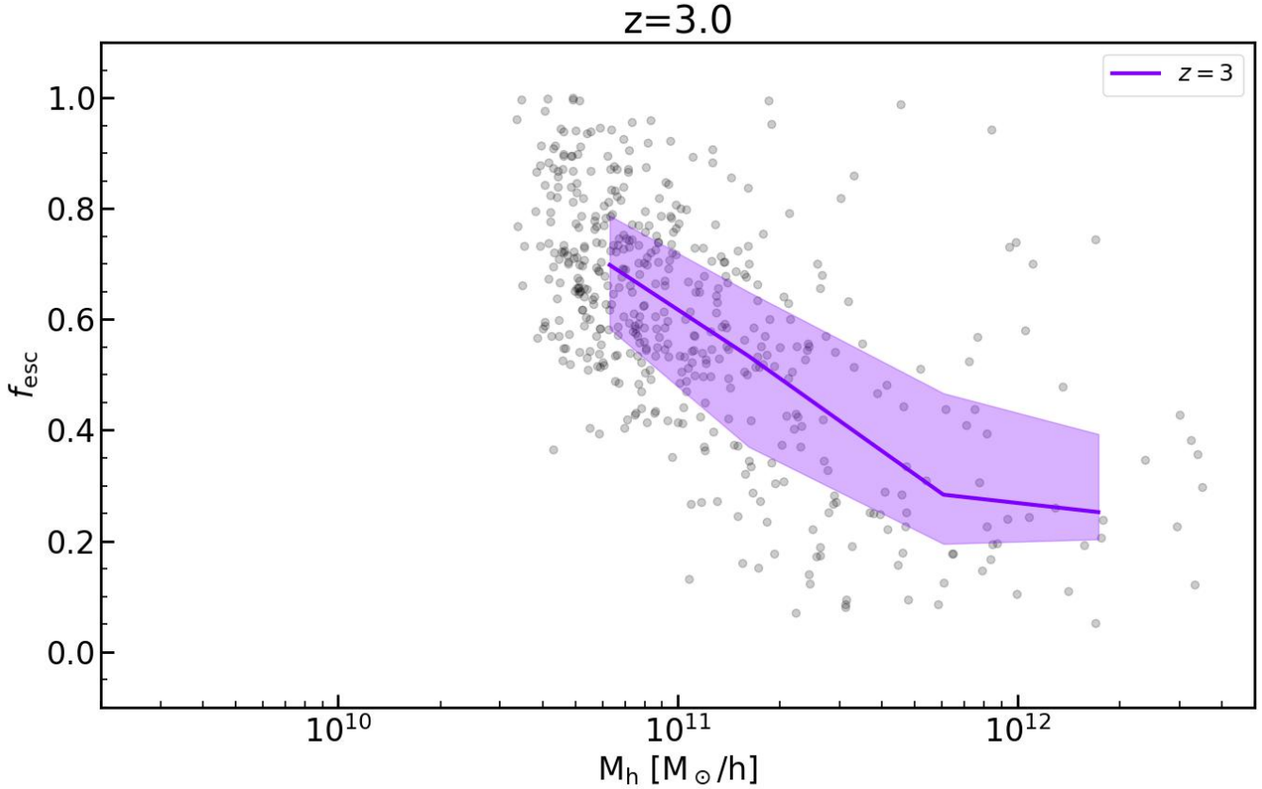

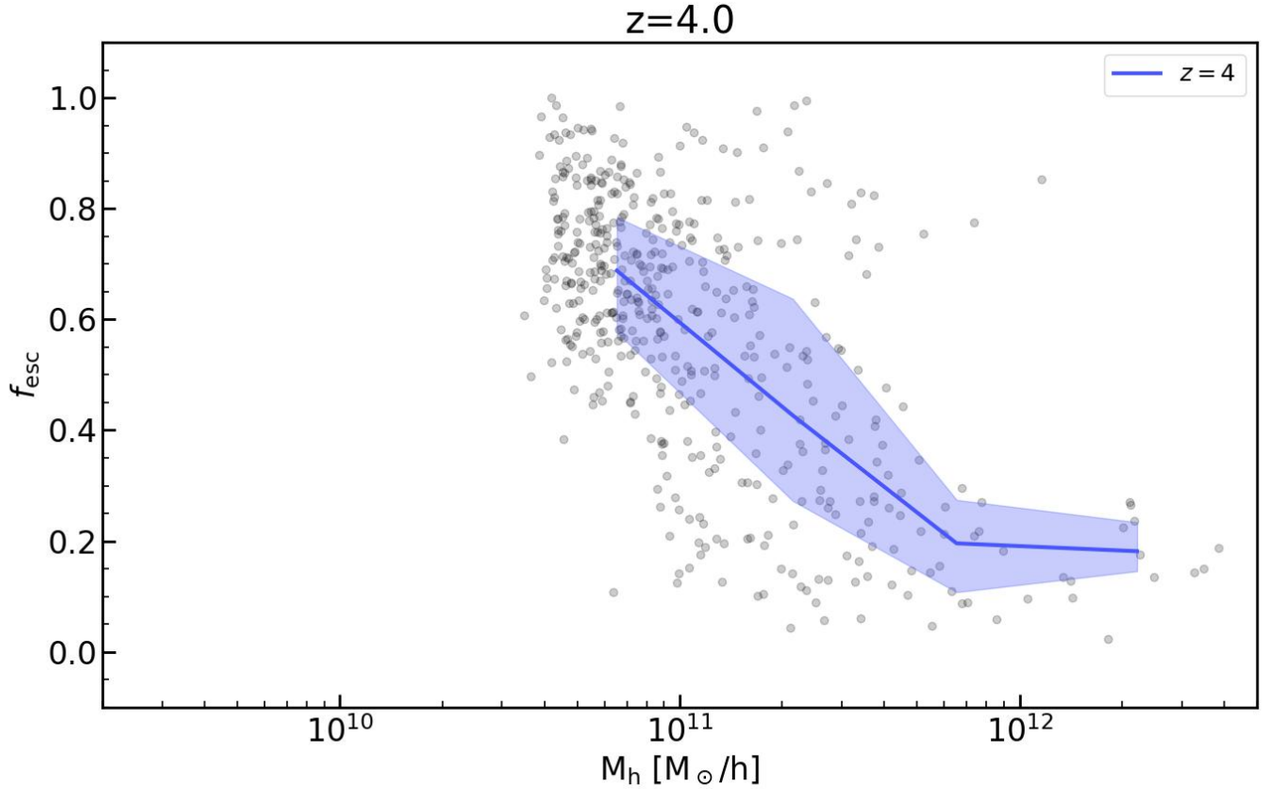

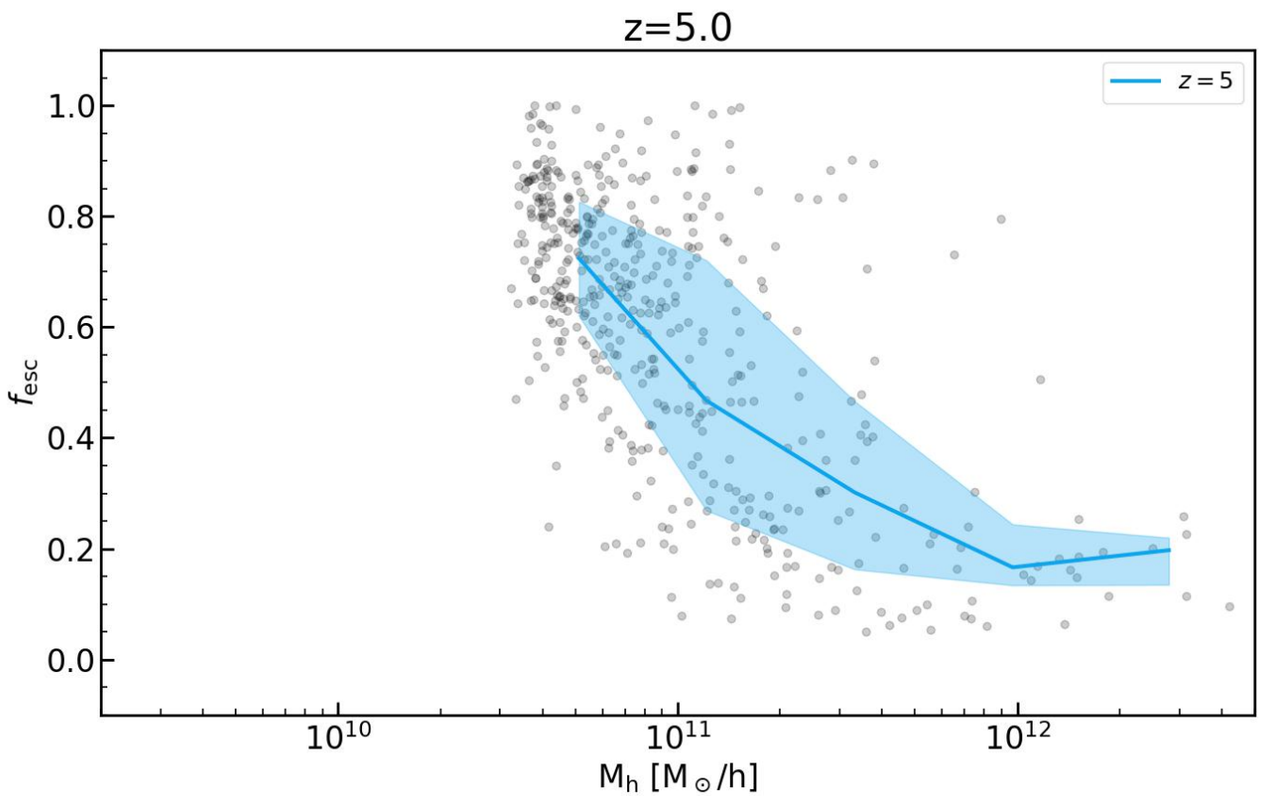

Escape Fraction v.s. Halo Mass

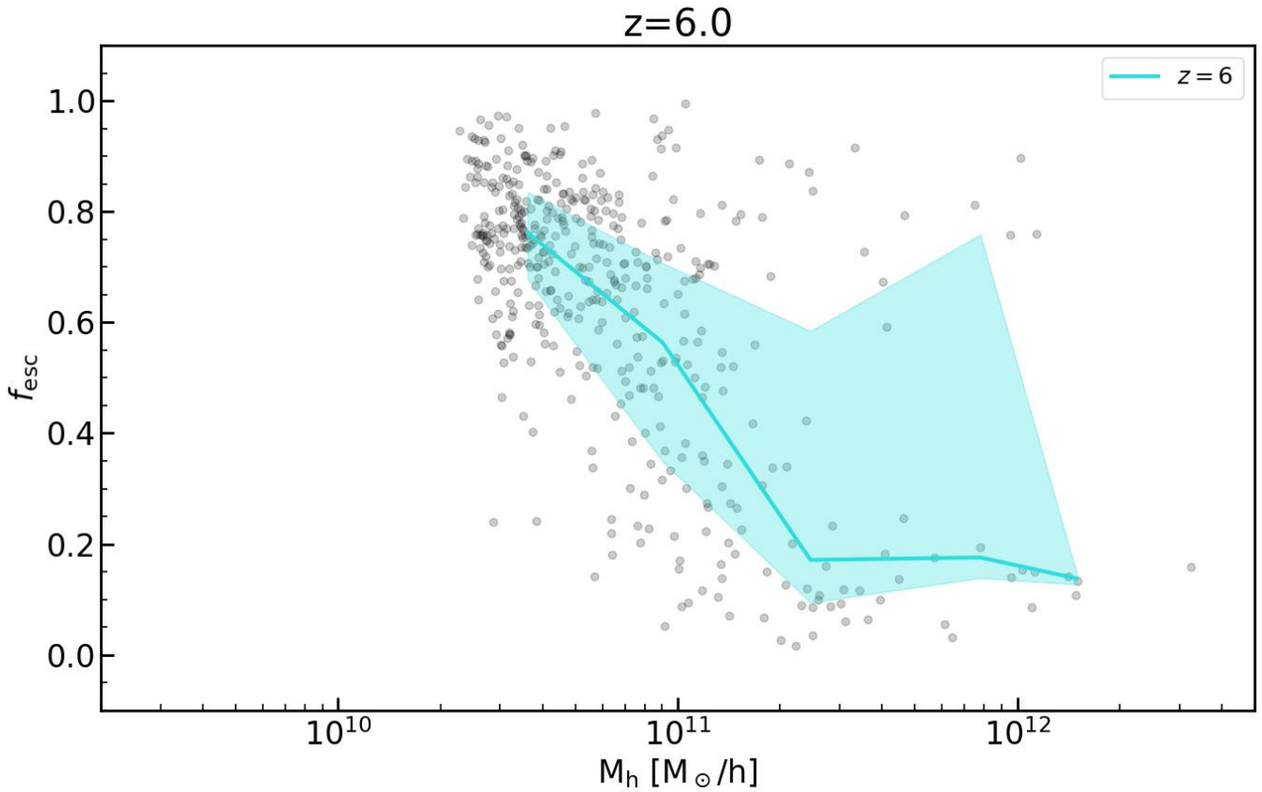

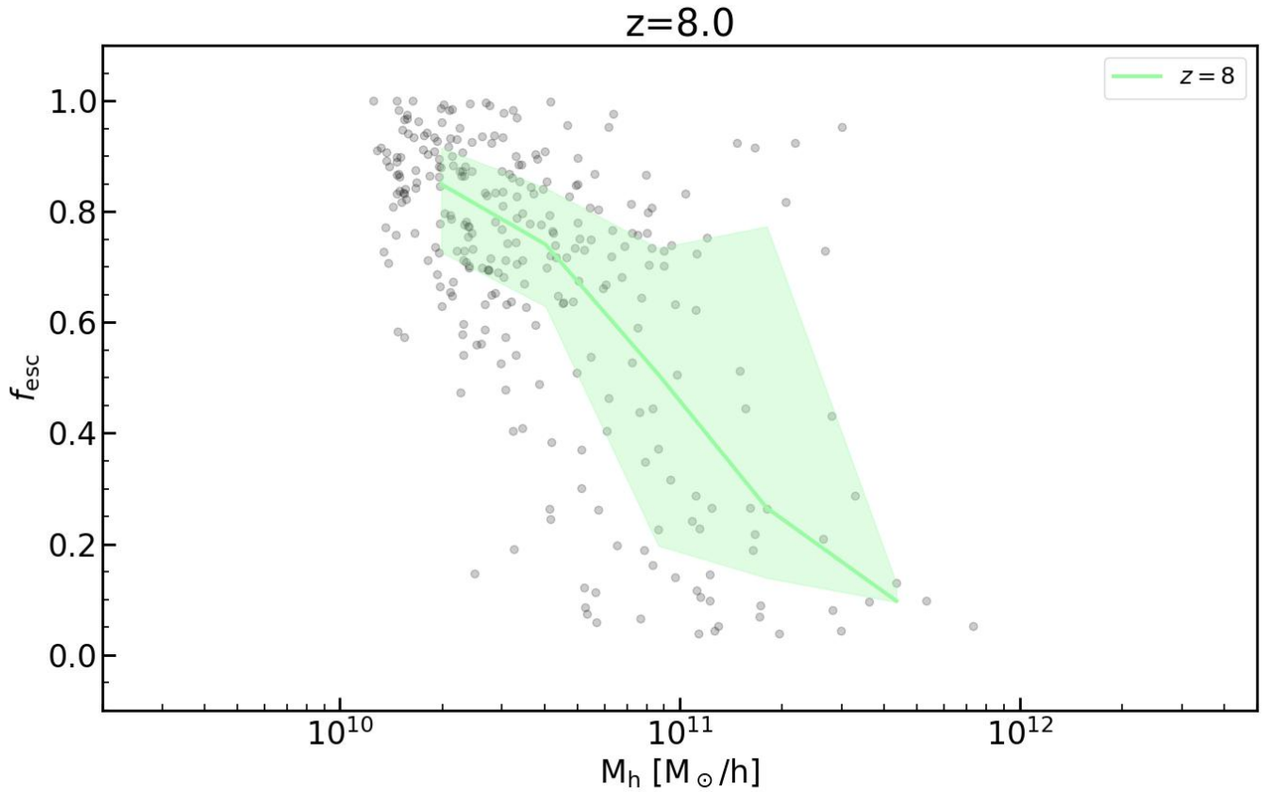

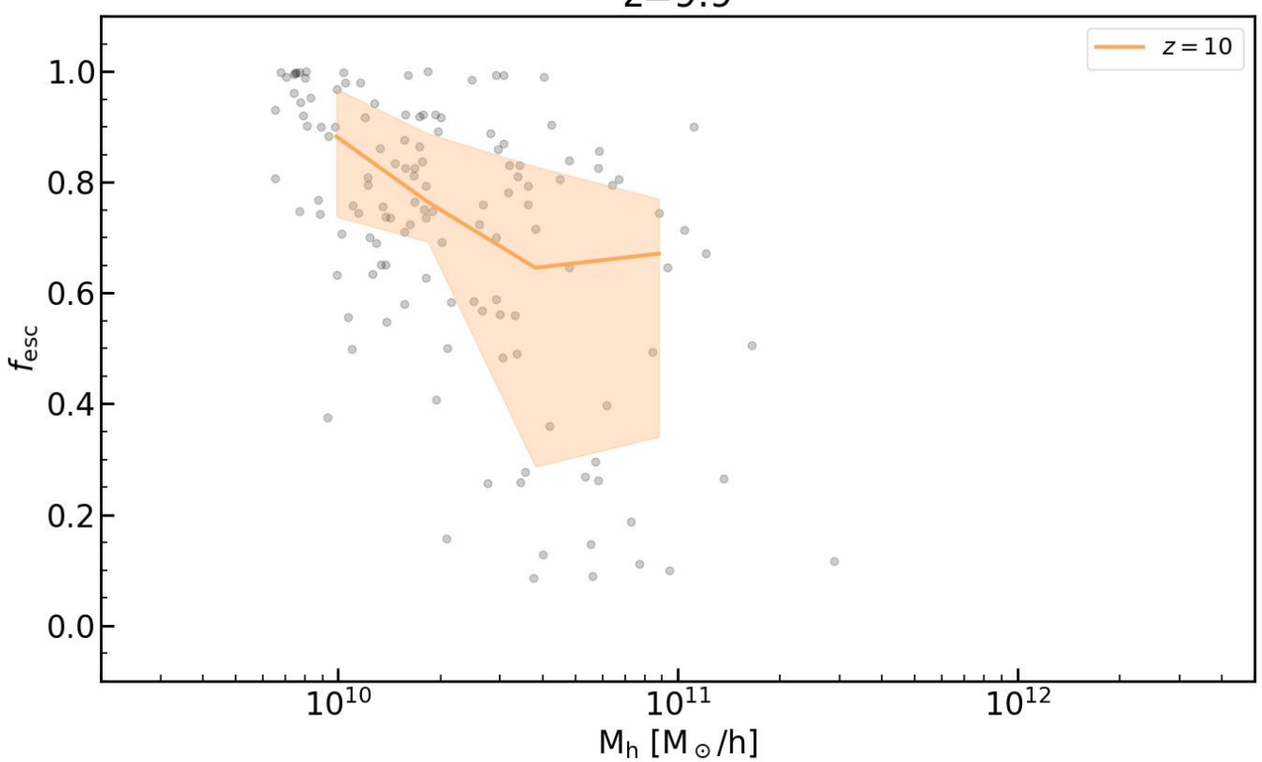

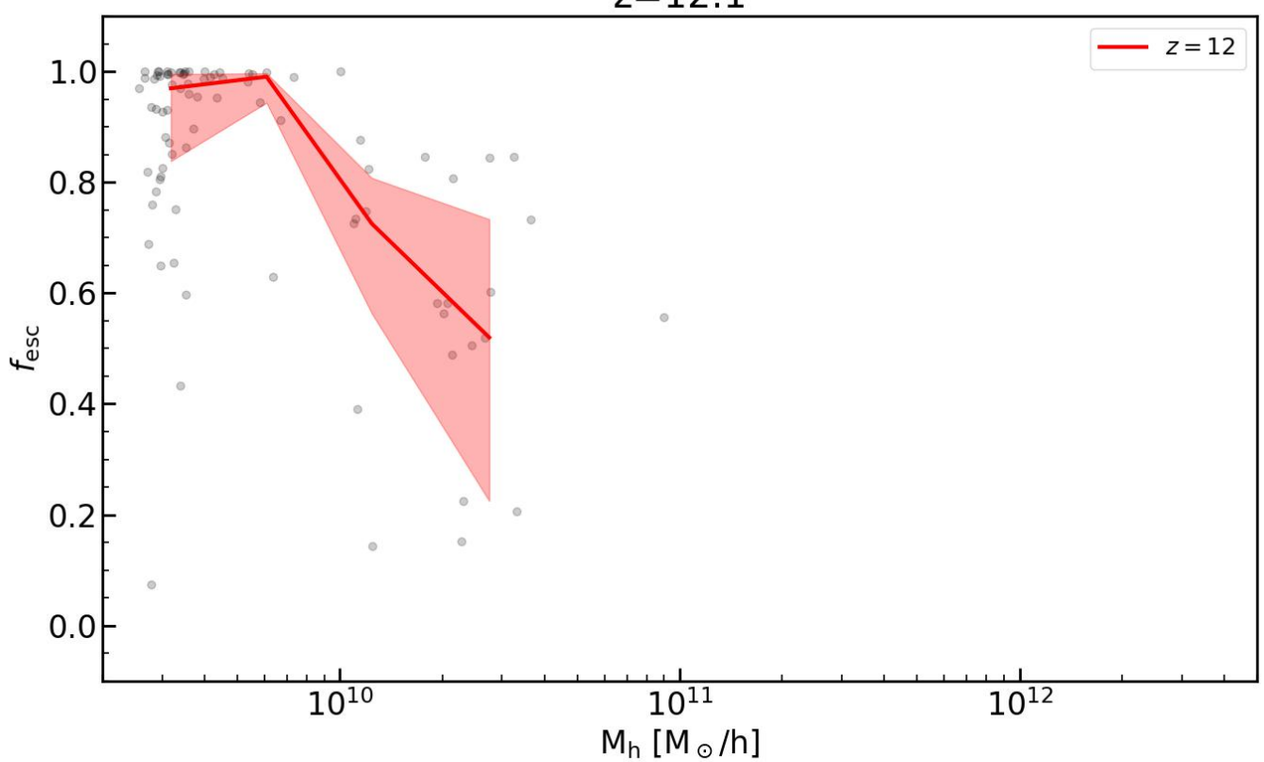

SED (z=6, 10^5 photons)

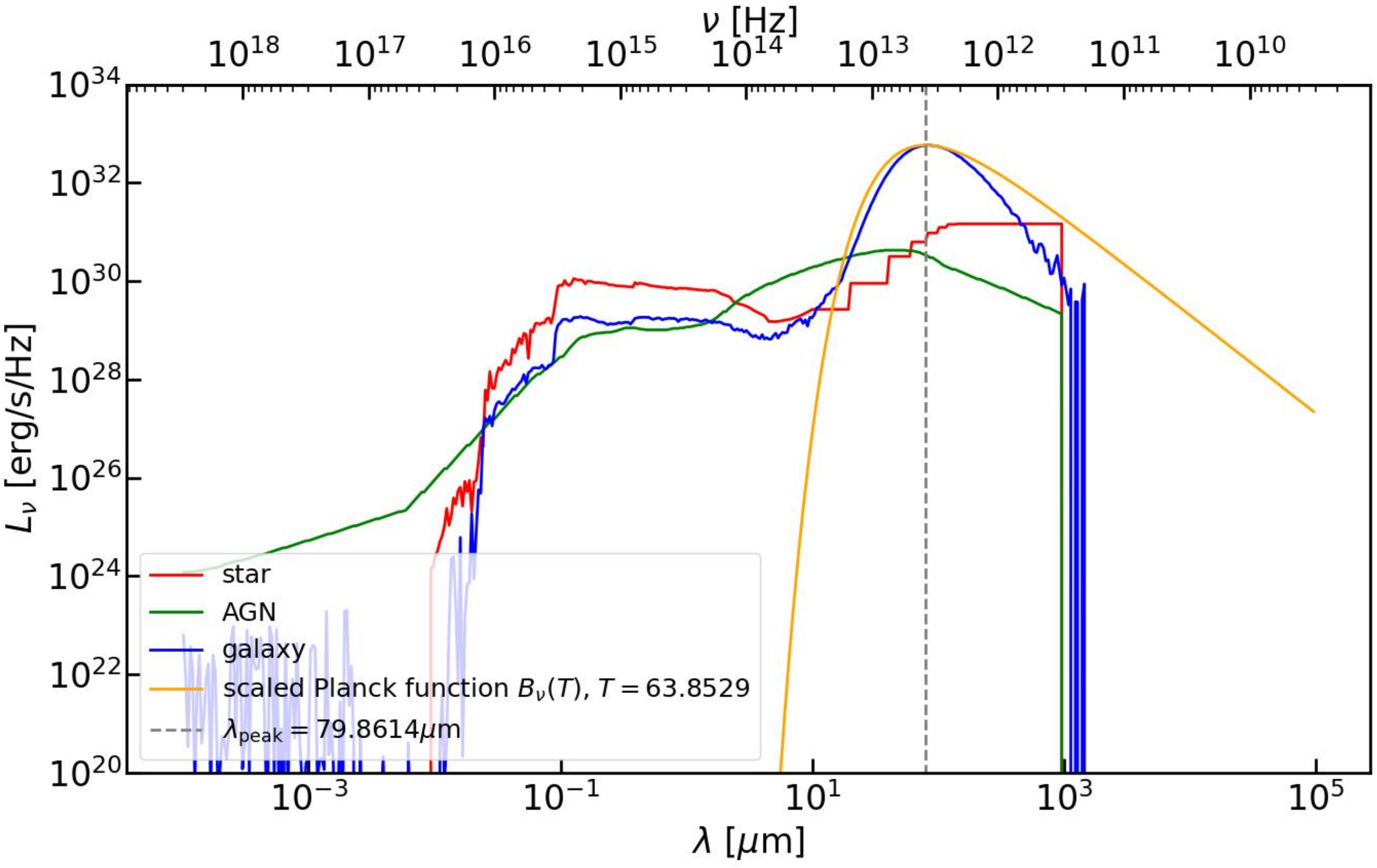

Dust Temperature v.s. Galaxy Compactness

Heating rate of dust grain by absorption of radiation:

$$\left(\frac{dE}{dt}\right)_{\text{abs}} = \int \frac{u_\nu d\nu}{h\nu} \times c \times h\nu \times Q_{\text{abs}}(\nu)\pi a^2$$

$u_\nu d\nu / h\nu$: number density of photons with frequencies in $[\nu,\ \nu + d\nu]$

$Q_{\text{abs}}(\nu)\pi a^2$: absorption cross section of dust grain

Let $\left\langle Q_{\text{abs}} \right\rangle_\star \equiv \dfrac{\int d\nu u_{\star\nu} Q_{\text{abs}}(\nu)}{u_\star}$, $u_\star \equiv \int d\nu u_{\star\nu}$ then

$$\left(\frac{dE}{dt}\right)_{\text{abs}} = \left\langle Q_{\text{abs}} \right\rangle_\star \pi a^2 u_\star c$$

Dust Temperature v.s. Galaxy Compactness

Rate of lost energy of dust grain by infrared radiation:

$$\left(\frac{dE}{dt}\right)_{\text{emiss.}} = \int d\nu\ 4\pi B_\nu(T_\text{d}) C_\text{abs}(\nu) = 4\pi a^2 \left\langle Q_\text{abs} \right\rangle_{T_\text{d}} \sigma T_\text{d}^4$$

$$\left\langle Q_\text{abs} \right\rangle_T \equiv \frac{\int d\nu B_\nu(T) Q_\text{abs}(\nu)}{\int d\nu B_\nu(T)}$$: Planck-averaged emission efficiency

Dust Temperature v.s. Galaxy Compactness

Heating rate of dust grain by absorption of radiation:

$$\left(\frac{dE}{dt}\right)_{\rm abs} = \left\langle Q_{\rm abs}\right\rangle_{\star} \pi a^2 u_{\star} c$$

Rate of lost energy of dust grain by infrared radiation:

$$\left(\frac{dE}{dt}\right)_{\rm emiss.} = \int d\nu\ 4\pi B_{\nu}(T_{\rm d}) C_{\rm abs}(\nu) = 4\pi a^2 \left\langle Q_{\rm abs}\right\rangle_{T_{\rm d}} \sigma T_{\rm d}^4$$

Dust temperature is determined by the balance between the heating and cooling:

$$\left\langle Q_{\rm abs}\right\rangle_{\star} \pi a^2 u_{\star} c = 4\pi a^2 \left\langle Q_{\rm abs}\right\rangle_{T_{\rm d}} \sigma T_{\rm d}^4$$

$$\rightarrow T_{\rm d}^4 = \frac{1}{4\sigma} \frac{\left\langle Q_{\rm abs}\right\rangle_{\star}}{\left\langle Q_{\rm abs}\right\rangle_{T_{\rm d}}} c u_{\star}$$

($u_{\star}$ is radiation energy per unit volume)

Dust Temperature v.s. Galaxy Compactness

$$T_{\rm d}^4 = \frac{1}{4\sigma} \frac{\left\langle Q_{\rm abs} \right\rangle_\star}{\left\langle Q_{\rm abs} \right\rangle_{T_{\rm d}}} c u_\star$$

Since $cu_\star$ is radiation energy per unit time and unit area,

$$cu_\star = \int d\nu \frac{L_\nu}{4\pi R^2} = \frac{L_{\rm bol}}{4\pi R^2}$$

$$\rightarrow T_{\rm d}^4 = \frac{1}{16\pi\sigma} \frac{\left\langle Q_{\rm abs} \right\rangle_\star}{\left\langle Q_{\rm abs} \right\rangle_{T_{\rm d}}} \frac{L_{\rm bol}}{R^2}$$

$$T_{\rm d} = \left(\frac{1}{16\pi\sigma} \frac{\left\langle Q_{\rm abs} \right\rangle_\star}{\left\langle Q_{\rm abs} \right\rangle_{T_{\rm d}}} \right) L_{\rm bol}^{1/4} \, R^{-1/2}$$

Observation (MACS0416_Y1)

Table 3. The fitting parameters of the tested single-temperature spectrum fits.

	$\beta = 1.5$				$\beta = 2.0$				$\beta = 2.5$		
$T_{z=0}$ (K)	μIR luminosity (10^{11} $L_\odot$)	χ^2 –	μM_{dust} (10^6 $M_\odot$)	$T_{z=0}$ (K)	μIR luminosity (10^{11} $L_\odot$)	χ^2 –	μM_{dust} (10^6 $M_\odot$)	$T_{z=0}$ (K)	μIR luminosity (10^{11} $L_\odot$)	χ^2 –	μM_{dust} (10^6 $M_\odot$)
30	0.31	18.9	11	–	0.49	15.8	5.1	–	0.76	12.2	2.28
50	1.34	10.3	3.0	–	2.21	6.79	1.2	–	3.56	3.88	0.47
70	4.53	6.15	1.6	–	8.11	3.40	0.6	–	14.4	1.51	0.22
90	12.2	4.15	1.1	–	23.8	2.00	0.4	–	46.4	0.64	0.14
110	28.5	3.07	0.8	–	59.8	1.30	0.3	–	126.8	0.23	0.10
130	59.2	2.42	0.7	–	133.4	0.90	0.2	–	310.8	0.019	0.085
121	46.0	2.7 (**90%**)	0.74	80	15.9	2.7 (**90%**)	0.5	60	8.95	2.7 (**90%**)	0.35

Notes: for each value of β, reading from the left, the columns are: Column 1 – CMB-corrected dust temperature; Column 2 – FIR luminosity, not corrected for magnification, μ; Column 3 – χ^2 value, measuring quality of fit; and Column 4 – dust mass, not corrected for magnification. The bottom row (bold text) shows the 90 per cent lower limit on the dust temperature, FIR luminosity, and dust mass for each β, found by interpolating the χ^2 to a value of 2.7 (Avni 1976).

Bakx et al. 2020

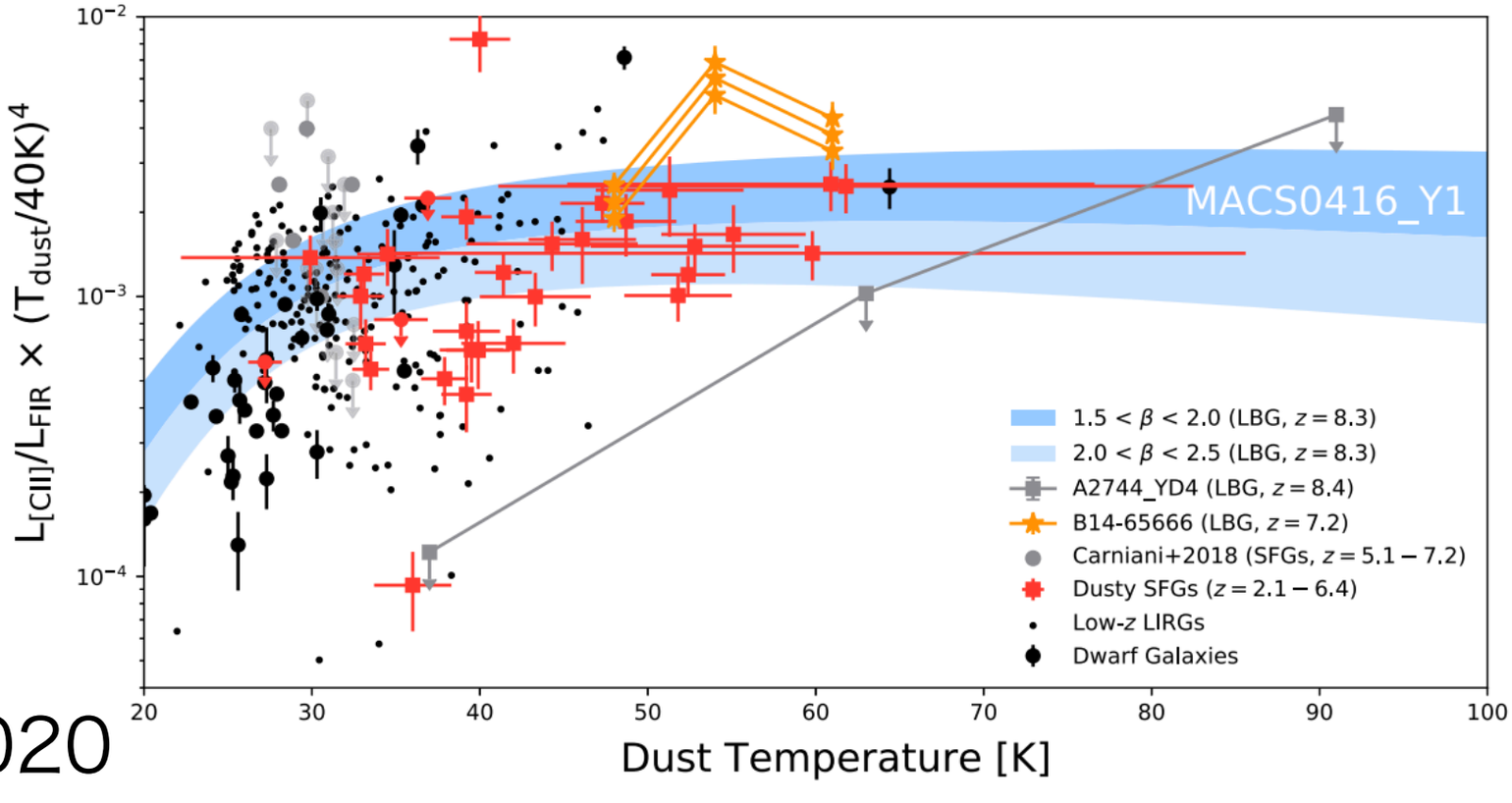

Figure 8. The temperature-corrected [C II] to FIR luminosity ratio is shown as a function of the dust temperature. We compare a range of temperatures and βs of MACS0416_Y1 against high-redshift LBGs, high-redshift DSFGs, low-redshift galaxies, and nearby dwarf galaxies. MACS0416_Y1 appears to have a similar ratio as the other sources, regardless of the dust temperature, and the ratio is only mildly dependent on β.

観測データ (Fuiimoto+2024)

Table 7
ALCS IR LFs

$\log(L_{\rm IR})[L_\odot]$	$\log(\Phi)[{\rm Mpc^{-1}\,dex^{-1}}]$					
	$0.6 \leqslant z < 1.0$	$1.0 \leqslant z < 2.0$	$2.0 \leqslant z < 3.0$	$3.0 \leqslant z < 4.0$	$4.0 \leqslant z < 6.0$	$6.0 \leqslant z < 7.5$
9.9–10.4	…	$-0.85^{+0.52}_{-0.76}$	…	…	…	$-2.49^{+0.52}_{-0.76}$
10.4–10.9	$-3.72^{+2.35}_{-99.9}$	$-1.93^{+0.3}_{-0.34}$	…	$-1.94^{+0.3}_{-0.34}$	$-3.24^{+0.52}_{-0.76}$	…
10.9–11.4	$-2.13^{+0.4}_{-1.24}$	$-2.54^{+0.2}_{-0.22}$	$-2.86^{+0.3}_{-0.34}$	$-2.96^{+0.25}_{-0.28}$	…	…
11.4–11.9	$-3.38^{+0.54}_{-0.25}$	$-2.95^{+0.13}_{-0.15}$	$-3.05^{+0.1}_{-0.12}$	$-3.98^{+0.26}_{-0.28}$	$-3.78^{+0.22}_{-0.25}$	…
11.9–12.2	$-3.59^{+0.57}_{-0.28}$	$-3.16^{+0.1}_{-0.17}$	$-3.59^{+0.12}_{-0.17}$	$-3.68^{+0.2}_{-0.22}$	$-4.3^{+0.3}_{-0.34}$	…
12.2–12.6	$-4.28^{+0.52}_{-99.9}$	$-3.62^{+0.2}_{-0.22}$	$-3.91^{+0.22}_{-0.25}$	$-3.93^{+0.25}_{-0.28}$	$-4.51^{+0.37}_{-0.45}$	…
12.6–12.9	…	$-4.59^{+0.52}_{-99.9}$	$-4.59^{+0.52}_{-99.9}$	$-4.27^{+0.37}_{-0.45}$	…	…
12.9–13.2	…	$-4.5^{+0.52}_{-0.76}$	$-4.52^{+0.52}_{-99.9}$	…	…	…

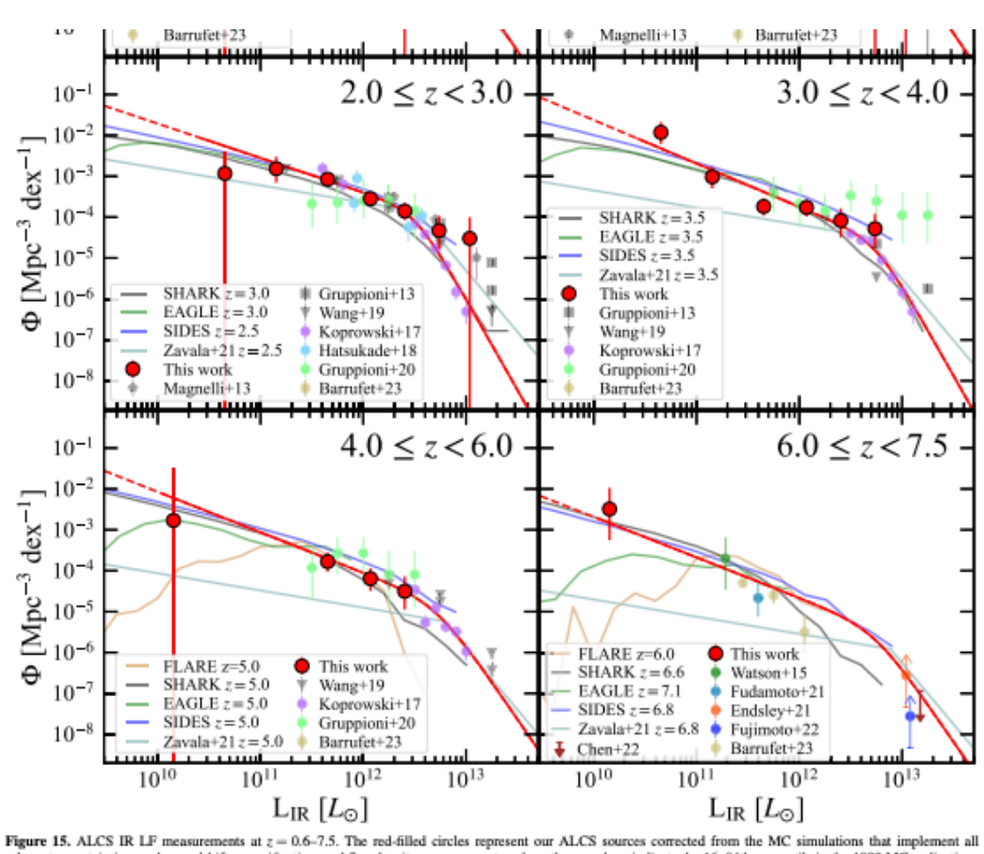

Figure 15. ALCS IR LF measurements at $z = 0.6$–7.5. The red-filled circles represent our ALCS sources corrected from the MC simulations that implement all relevant uncertainties, such as redshift, magnification, and flux density measurements, where the error bars indicate the 16–84th percentile in the 1000 MC realizations (see Section 5.1). Previous IR LF measurements with Herschel (Gruppioni et al. 2013; Magnelli et al. 2013; Wang et al. 2019a) and ALMA(+SCUBA2) are presented in gray and colored symbols, respectively. The red line presents the best-fit DPL functions, where we include our measurements and other ALMA blind survey results (Koprowski et al. 2017; Hatsukade et al. 2018) in the fitting. The other color lines show the predictions from simulations (Lagos et al. 2020; Trayford et al. 2020; Bethermin et al. 2022; Vijayan et al. 2022) and an empirically calibrated model (Zavala et al. 2021).

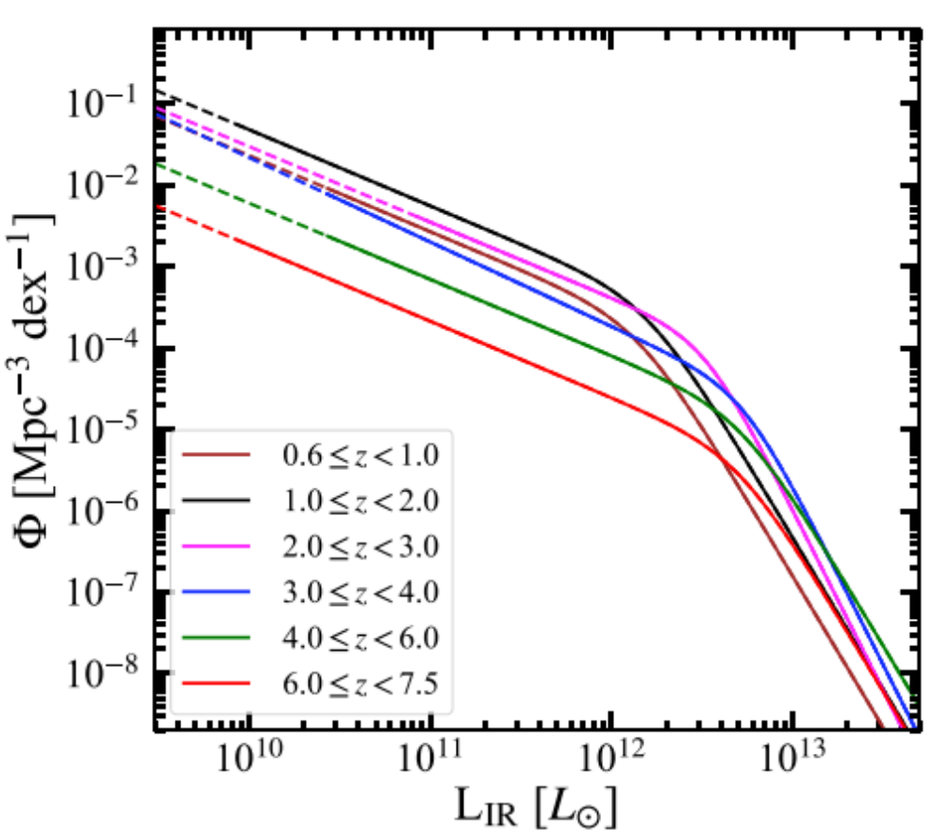

Figure 16. Evolution of IR LFs based on our best-fit DPL functions presented in Figure 15. We find the overall trends characterized by the positive luminosity evolution coupled with the negative density evolution.

観測データ (Barrufet+2023)

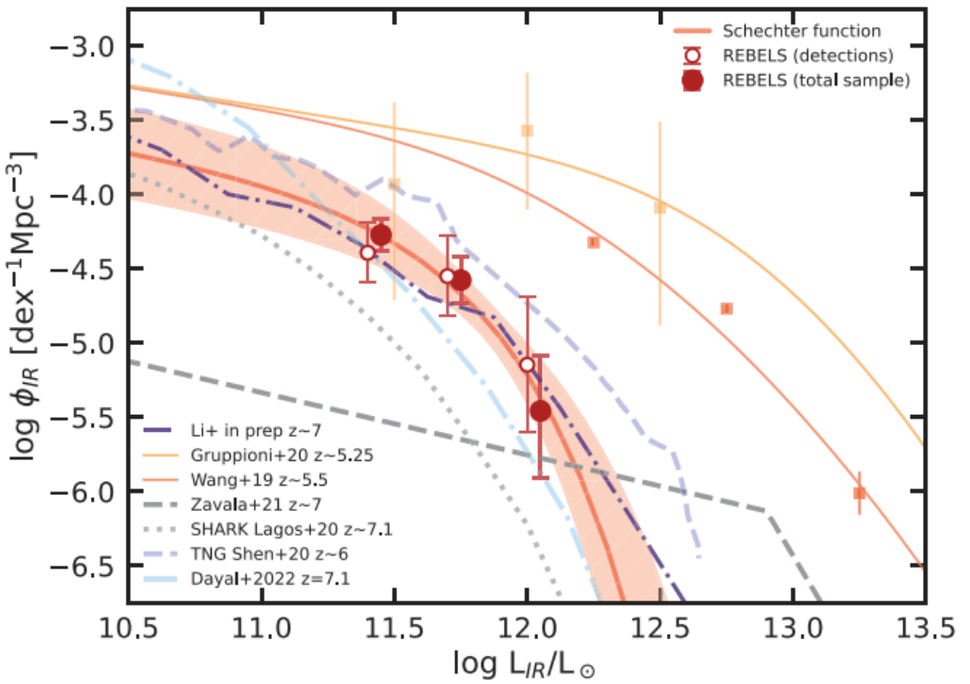

Figure 3. Infrared luminosity function (IRLF) at $z \sim 7$ for the REBELS sample (red dots and lines) compared with simulations (dashed lines) and observations (solid lines). The IRLF was calculated both only using the galaxies with dust continuum detections (16 galaxies, empty dots) and using the full sample including upper limits (42 galaxies, filled red dots). The red line shows the Schechter (1976) fit for the total sample. The shaded area shows the uncertainty of the luminosity function (LF) Schechter function fit with the total sample that is larger at the low-luminosity end due to the lack of data. The rest of the lines show both theoretical and observational IRLF studies in several fields. Our study is in agreement with Li et al. (in preparation, dark purple line) that predict a similar number of dusty galaxies in a broad range of luminosities. The dark grey line is the IRLF at $z \sim 7$ from Zavala et al. (2021) and predicts a larger number of galaxies than our study for the bright end with luminosities ($12.5 < \log(L_{IR}/L_\odot < 13$), whereas our LF does not predict a significant number of galaxies at $z \sim 7$ with $\log(L_{IR}/L_\odot > 12.5$). TNG simulations at $z \sim 6$ from Shen et al. (2022) show a systematic shift with respect to our fitting, but consistent in shape (blue dashed line). Dayal et al. (2022) and Lagos et al. (2020) simulations at $z \sim 7$ (light blue and grey line, respectively) present a 1 dex difference in the lower luminosity with our result in between them. The yellow line and dots indicate the IRLF at $z \sim 5.25$ predicted by the serendipitous galaxies found in the ALPINE survey presented in Gruppioni et al. (2020), whereas the orange symbols show Wang et al. (2019a) results at similar redshift.

α	$\log(L^*)$ ($L_\odot$)	$\log(\phi_{IR})$ ($\mathrm{dex}^{-1}\,\mathrm{Mpc}^{-3}$)	$\log(\mathrm{SFRD})$ ($M_\odot\,\mathrm{yr}^{-1}\,\mathrm{Mpc}^{-3}$)
		Schechter function fit	
-1.3 (fix)	$11.60^{+0.23}_{-0.13}$	$-4.38^{+0.38}_{-0.35}$	$-2.66^{+0.17}_{-0.14}$
Total sample	11.45	$-4.3^{+0.1}_{-0.1}$	-2.93 ± 0.20
	11.75	$-4.6^{+0.2}_{-0.2}$	
	12.05	$-5.5^{+0.4}_{-0.5}$	
Detections	11.45	$-4.4^{+0.2}_{-0.2}$	-3.21 ± 0.18
	11.75	$-4.6^{+0.3}_{-0.3}$	
	12.05	$-5.1^{+0.2}_{-0.5}$	

観測データ (Gruppioni+2020)

A&A 643, A8 (2020)

Table 4. ALPINE total IR LF.

$\log(L_{IR}/L_\odot)$	$\log(\phi/\mathrm{Mpc^{-3}\,dex^{-1}})$ [N_{obj}]					
	$0.5 < z < 1.5$	$1.5 < z < 2.5$	$2.5 < z < 3.5$	$3.5 < z < 4.5$	$4.5 < z < 6.0$	
					No [C II] emitters	All
(1)	(2)	(3)	(4)	(5)	(6)	(7)
10.75 – 11.25		**($-3.96^{+0.66}_{-0.76}$ [1])**				
11.00 – 11.50	*($-3.60^{+0.56}_{-0.68}$ [2])*	*($-3.64^{+0.53}_{-0.59}$ [2])*			*($-3.93^{+0.55}_{-0.78}$ [1])*	*($-3.96^{+0.55}_{-0.78}$ [1])*
11.25 – 11.75	**$-3.50^{+0.49}_{-0.57}$ [3]**	**$-3.67^{+0.53}_{-0.59}$ [2]**	**($-3.66^{+0.37}_{-0.75}$ [2])**		**$-3.93^{+0.55}_{-0.78}$ [1]**	**$-3.96^{+0.55}_{-0.78}$ [1]**
11.50 – 12.00	*$-3.46^{+0.40}_{-0.42}$ [4]*	*$-3.64^{+0.64}_{-0.52}$ [3]*	*$-3.43^{+0.43}_{-0.47}$ [4]*	*$-3.37^{+0.40}_{-0.82}$ [2]*	*$-3.57^{+0.39}_{-0.53}$ [2]*	*$-3.60^{+0.41}_{-0.52}$ [2]*
11.75 – 12.25	**$-3.54^{+0.45}_{-0.46}$ [3]**	**$-3.60^{+0.52}_{-0.44}$ [5]**	**$-3.68^{+0.45}_{-0.55}$ [4]**	**$-3.37^{+0.40}_{-0.58}$ [2]**	**$-3.57^{+0.39}_{-0.53}$ [2]**	**$-3.60^{+0.41}_{-0.52}$ [2]**
12.00 – 12.50	*$-4.41^{+0.66}_{-0.76}$ [1]*	*$-3.59^{+0.36}_{-0.37}$ [7]*	*$-3.84^{+0.39}_{-0.52}$ [5]*	*$-4.10^{+0.59}_{-0.78}$ [1]*	*$-4.09^{+0.58}_{-0.79}$ [1]*	*$-4.12^{+0.59}_{-0.78}$ [1]*
12.25 – 12.75	**$-3.99^{+0.53}_{-0.97}$ [2]**	**$-3.84^{+0.42}_{-0.67}$ [4]**	**$-3.47^{+0.36}_{-0.39}$ [9]**	**$-4.10^{+0.52}_{-0.78}$ [1]**	**$-4.09^{+0.58}_{-0.79}$ [1]**	**$-4.12^{+0.59}_{-0.78}$ [1]**
12.50 – 13.00	*$-3.97^{+0.53}_{-0.99}$ [2]*		*$-3.61^{+0.41}_{-0.46}$ [6]*			*$-4.17^{+0.59}_{-0.78}$ [1]*
12.75 – 13.25	**$-4.36^{+0.83}_{-0.76}$ [1]**		**$-3.95^{+0.56}_{-0.69}$ [2]**			**$-3.87^{+0.43}_{-0.62}$ [2]**
13.00 – 13.50			*$-3.95^{+0.56}_{-0.69}$ [2]*			*$-4.17^{+0.59}_{-0.76}$ [1]*

Notes. The bold (or alternatively italic) fonts denote independent luminosity bins. Values in parentheses correspond to luminosity bins that might be affected by incompleteness due to survey limits.

観測データ (Koprowski+2017)

Table 2. Rest-frame 250-μm LFs.

$\log(L_{250}/\mathrm{W\,Hz^{-1}})$	$\log(\Phi/\mathrm{Mpc^{-3}\,dex^{-1}})$			
	$0.5 < z < 1.5$	$1.5 < z < 2.5$	$2.5 < z < 3.5$	$3.5 < z < 4.5$
24.8	...	-2.81 ± 0.16	...	...
25.0	...	-3.20 ± 0.23	...	...
25.6	-4.23 ± 0.08	-3.86 ± 0.05	...	...
25.7	-4.68 ± 0.11	-4.17 ± 0.05	-4.40 ± 0.08	-4.47 ± 0.12
25.8	-5.14 ± 0.13	-4.42 ± 0.06	-4.56 ± 0.08	-5.27 ± 0.18
25.9	-5.42 ± 0.16	-4.76 ± 0.07	-4.58 ± 0.07	-4.93 ± 0.11
26.0	-6.11 ± 0.30	-5.18 ± 0.11	-5.05 ± 0.09	-5.37 ± 0.14
26.1	...	-5.83 ± 0.20	-5.46 ± 0.14	-5.49 ± 0.15
26.2	...	-6.31 ± 0.30	-5.83 ± 0.20	-5.97 ± 0.23
26.3	...	...	-6.31 ± 0.30	...

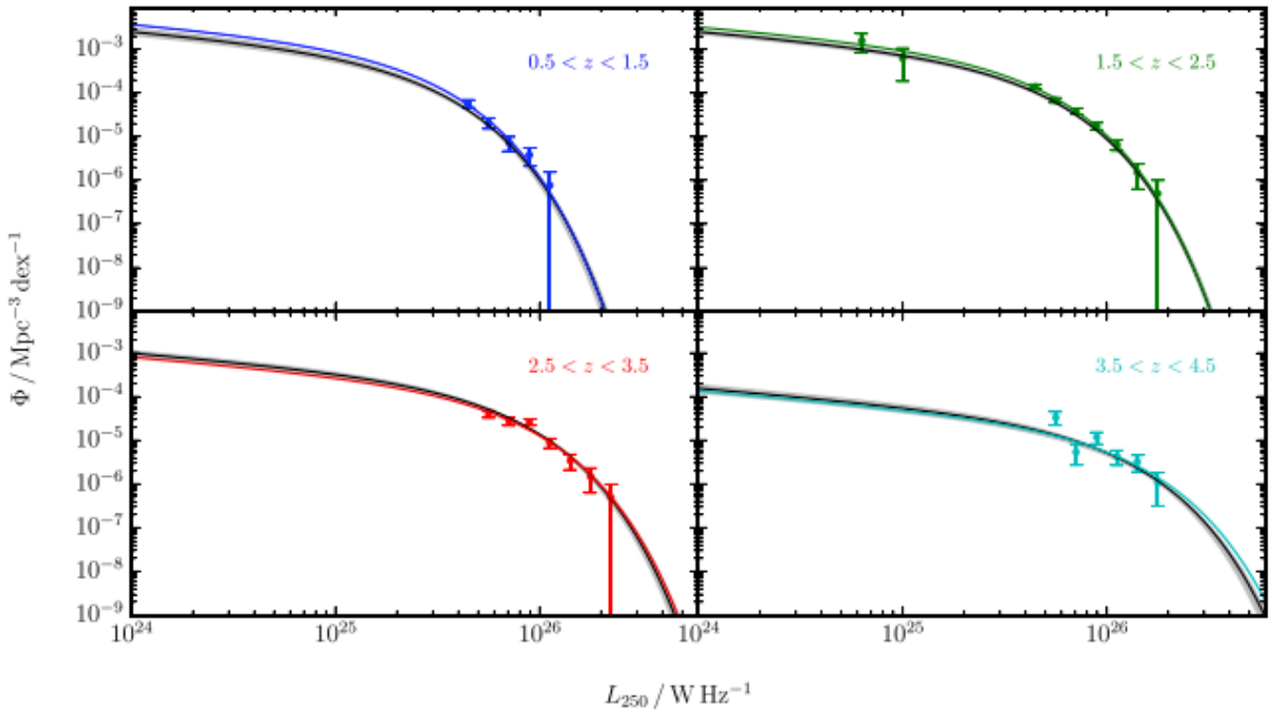

Figure 3. The far-IR (rest-frame 250-μm) galaxy LFs for the four redshift bins studied in this work. The points with error bars show the LF values determined using the $1/V_{\mathrm{max}}$ method. The two faintest points in the $1.5 < z < 2.5$ redshift bin depict the LF values found using the ALMA data. These allowed us to determine the faint-end slope $\alpha = -0.4$, which was then adopted for the other redshift bins. The coloured solid lines show the best-fitting Schechter functions to these data points. The black solid lines (almost perfectly aligned with the coloured solid lines) depict the results of the maximum-likelihood method, with the derived uncertainty indicated by the shaded grey region.

観測データ (Hatsukade+2018)

Table 6. IR luminosity functions.

$\log(L_{\rm IR}/L_\odot)^*$	N	$\log(\Phi/{\rm Mpc^{-3}\,dex^{-1}})$
	$1.0 < z < 2.0$	
11.86	4	$-3.89^{+0.25}_{-0.28}$
12.46	2	$-4.34^{+0.37}_{-0.45}$
	$1.5 < z < 2.5$	
11.91	6	$-3.66^{+0.20}_{-0.22}$
12.44	3	$-4.25^{+0.30}_{-0.34}$
	$2.0 < z < 3.0$	
11.94	7	$-3.05^{+0.19}_{-0.20}$
12.57	6	$-3.97^{+0.20}_{-0.22}$

*Weighted-mean luminosity in each bin.

Publications of the Astronomical Society of Japan (2018), Vol. 70, No. 6 **105-17**

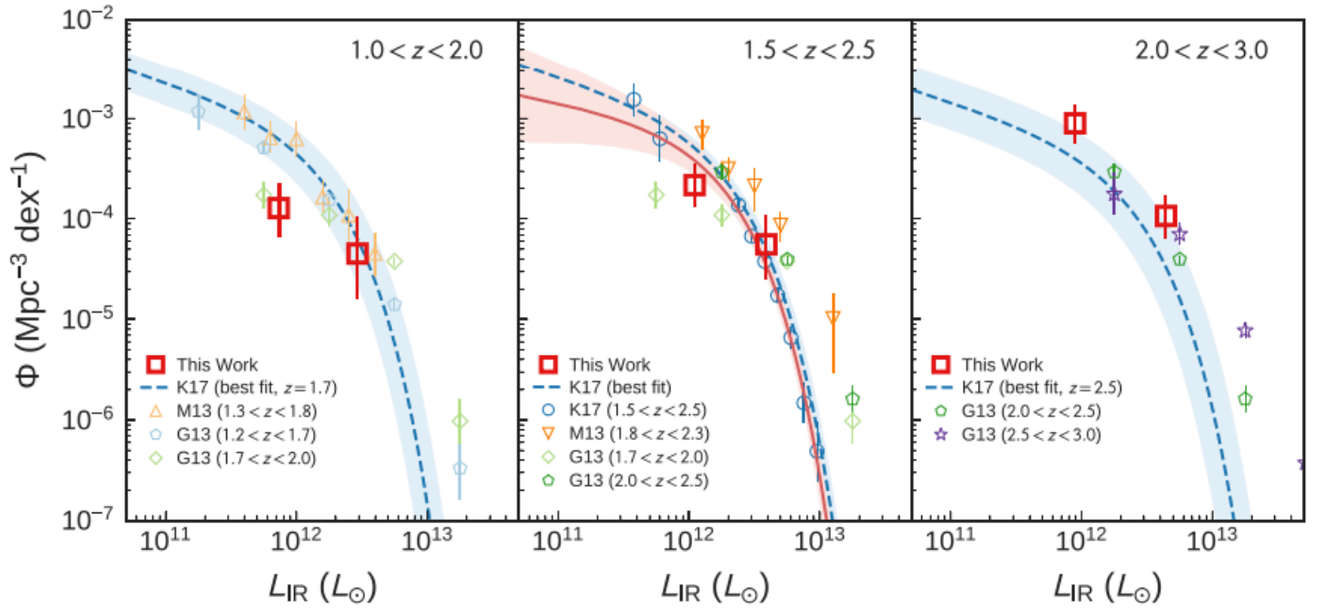

Fig. 18. IR luminosity functions constructed from the ASAGAO sources at $1.0 < z < 2.0$ (left), $1.5 < z < 2.5$ (middle), and $2.0 < z < 3.0$ (right). We plot luminosity functions obtained in Koprowski et al. (2017) (K17) by using 1.3 mm sources from the ALMA HUDF survey and 850 μm sources from the SCUBA-2 Cosmology Legacy Survey. The dashed curve and shaded area represent the best-fitting functions and $1\,\sigma$ error of Koprowski et al. (2017). At $1.5 < z < 2.5$, we plot their data points derived from the $V_{\rm max}$ method and the best-fitting function. At $1.0 < z < 2.0$ and $2.0 < z < 3.0$, we plot their functional form of the redshift evolution of the LF derived from the maximum-likelihood method, adopting the mean redshifts of the ASAGAO sources in each redshift bin ($z = 1.55$ and $z = 2.49$, respectively). The results of Herschel observations by Magnelli et al. (2013) (M13) and Gruppioni et al. (2013) (G13) are also compared. The solid curve and shaded area represent the the best-fitting Schechter function and $1\,\sigma$ error fitted to the results of ASAGAO and Koprowski et al. (2017) at $1.5 < z < 2.5$. (Color online)

$\Delta L = 10\ \mathrm{L}_\odot$のluminosity function

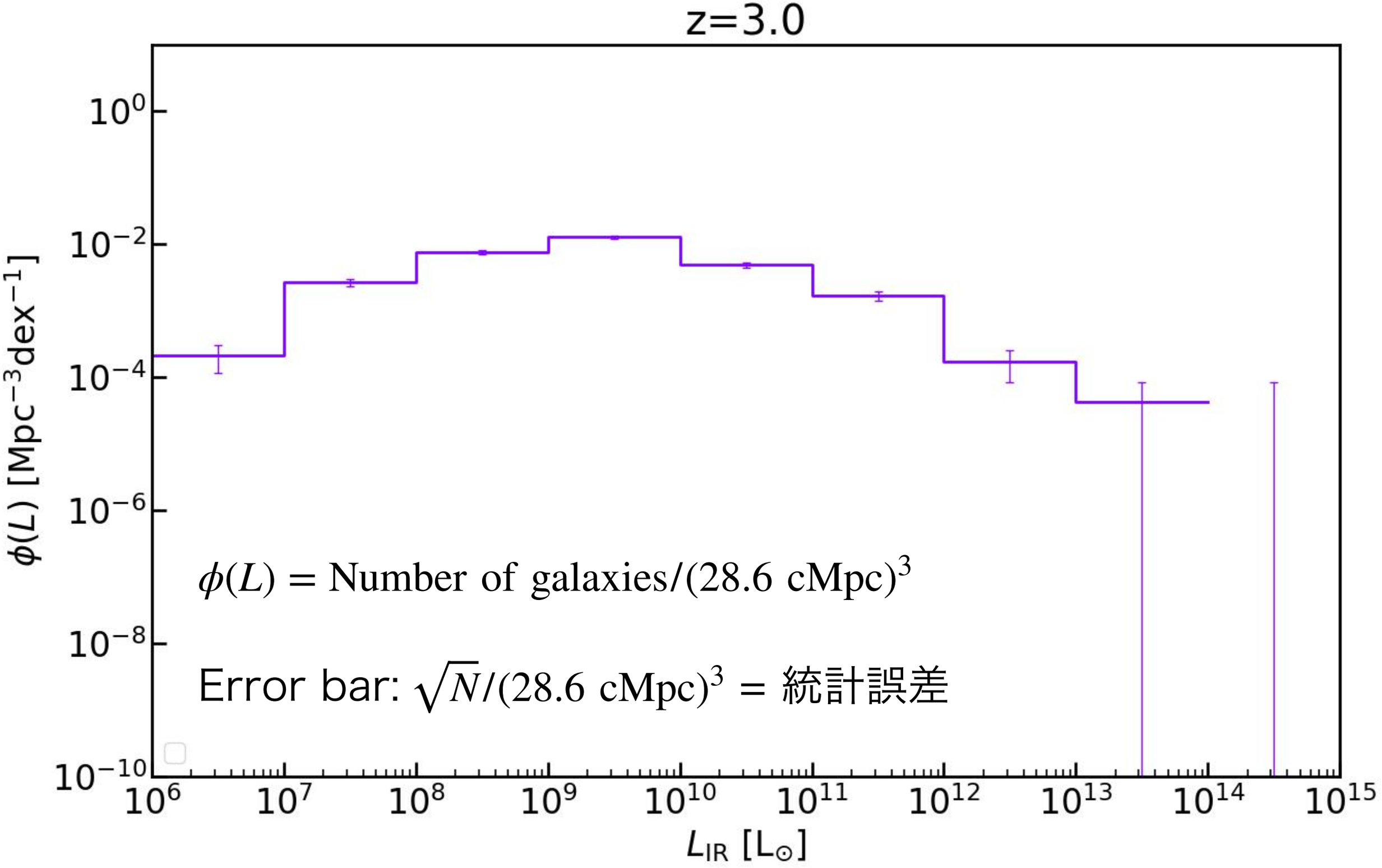

SED (z=6, 10^5 photons)

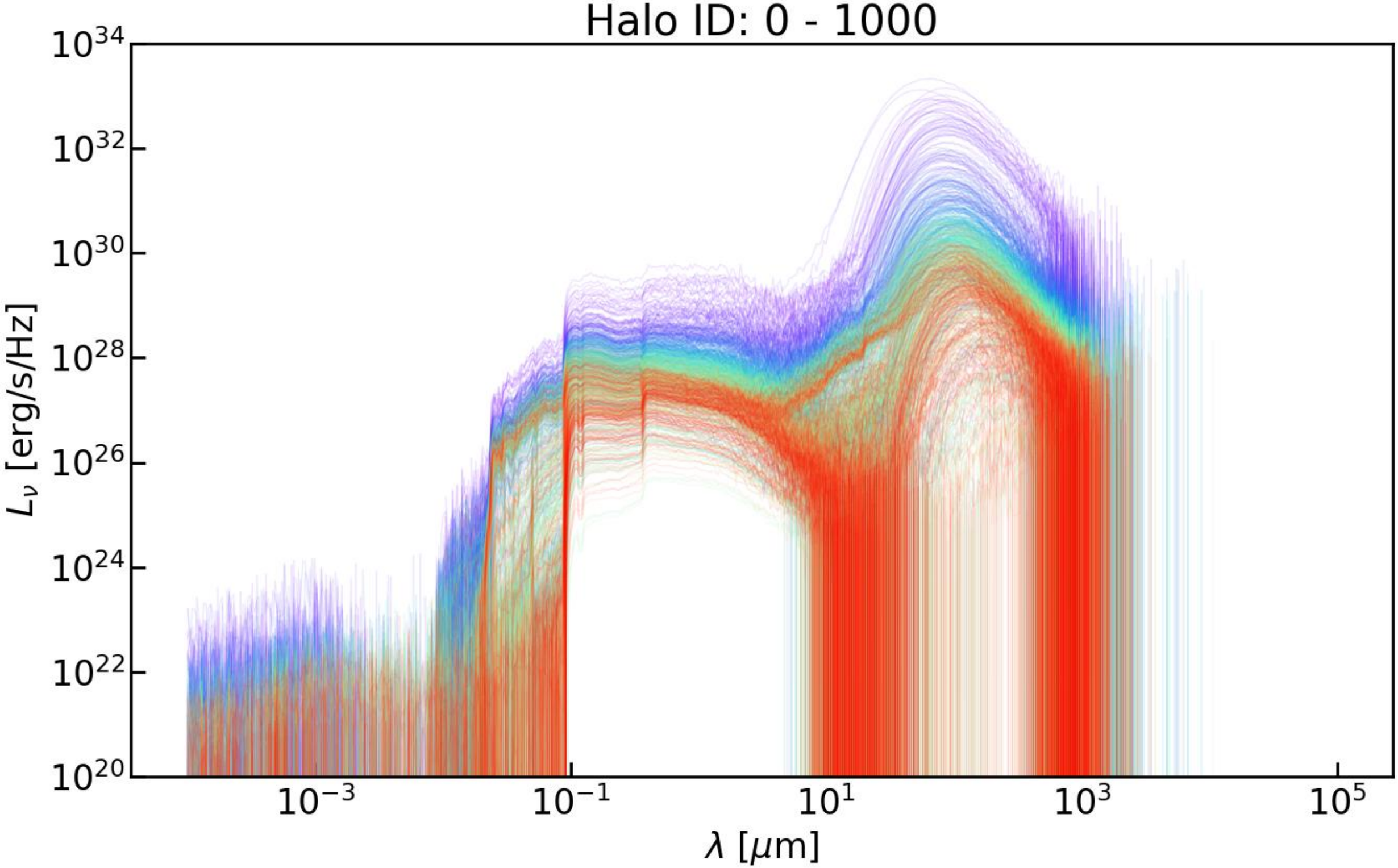

SED (z=8, 10^5 photons)

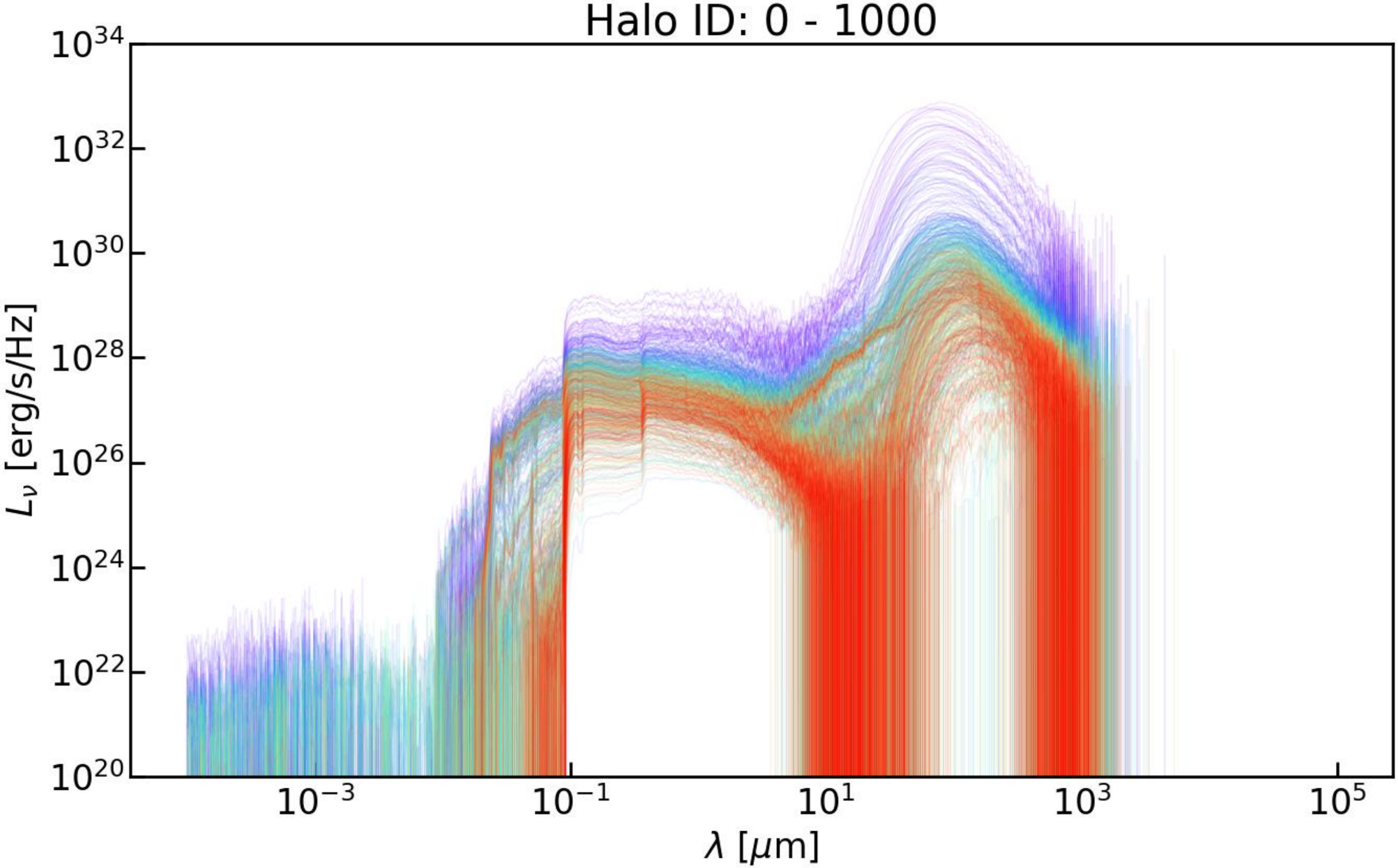

SED (z=10, 10^5 photons)

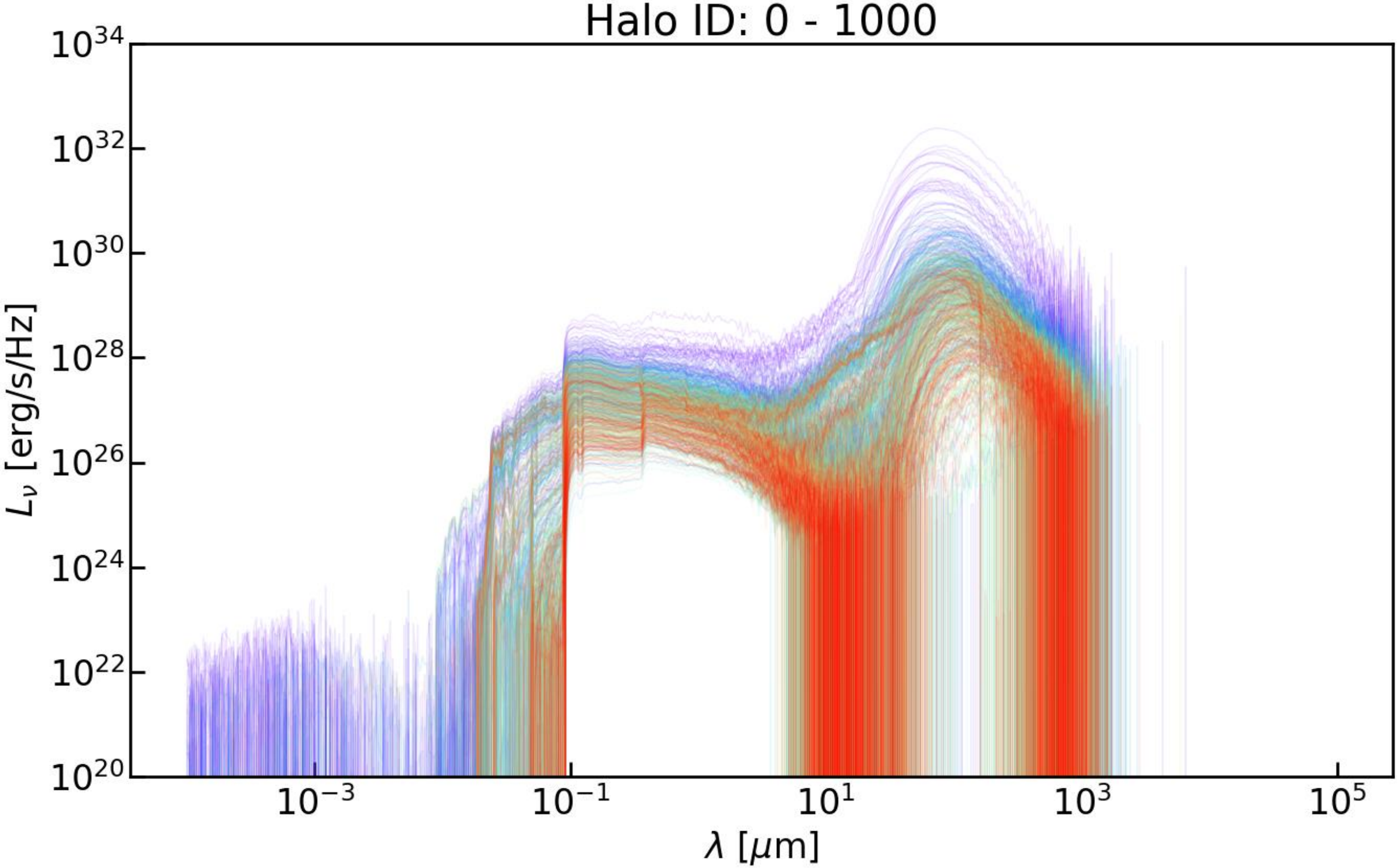

SED (z=12, 10^5 photons)

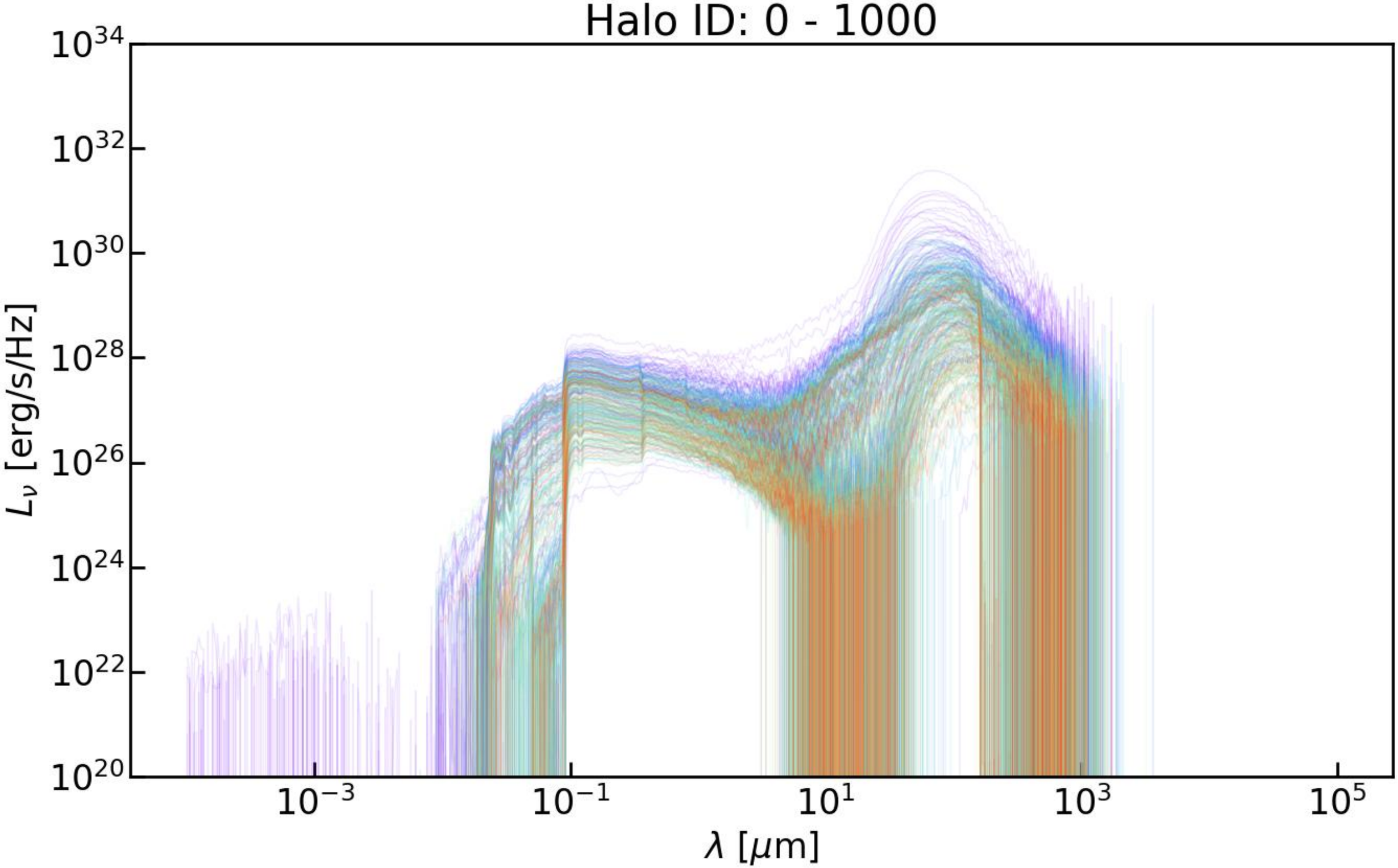

SED (z=14, 10^5 photons)

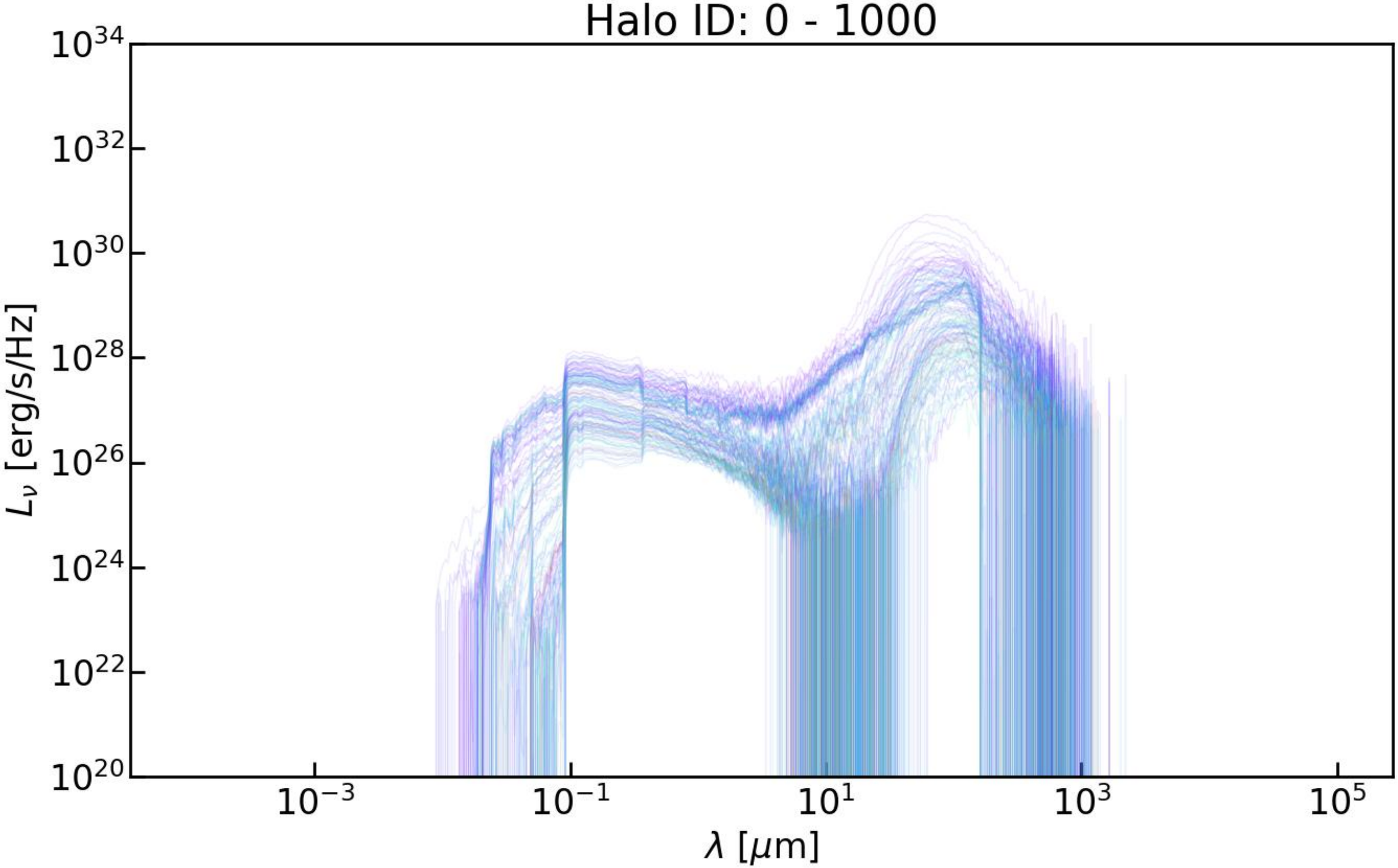

Half-Light Radius (z=6)

ID=0
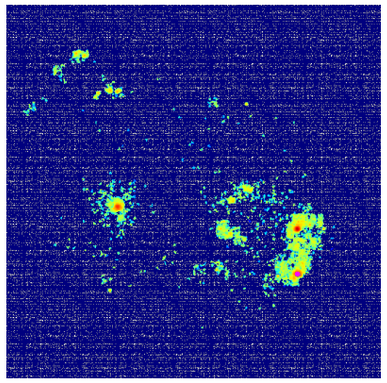

ID=1
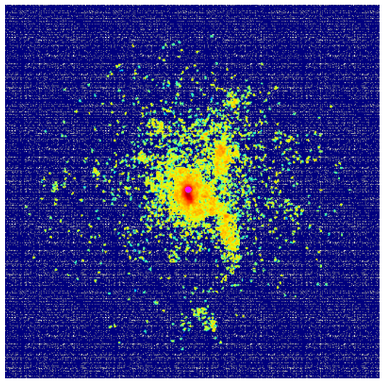

ID=2
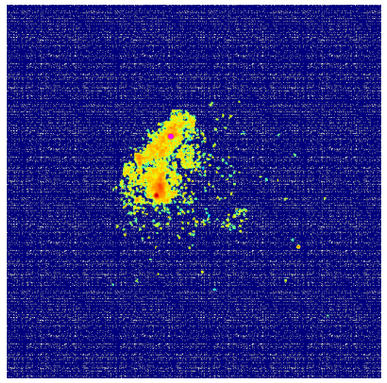

ID=3
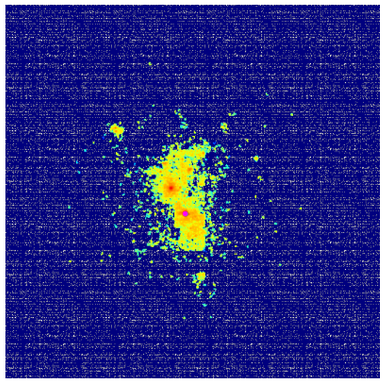

ID=4
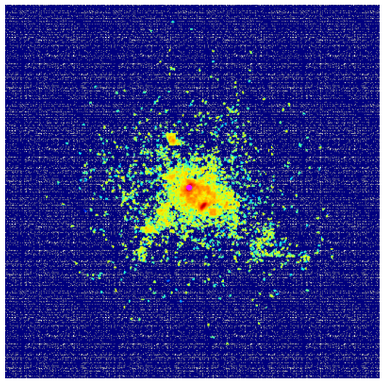

ID=5
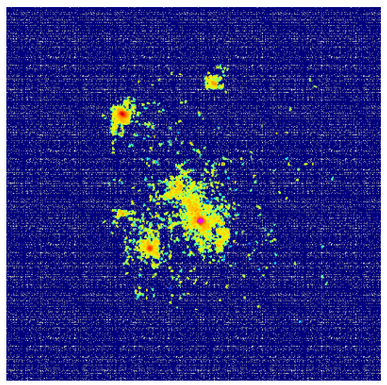

ID=6
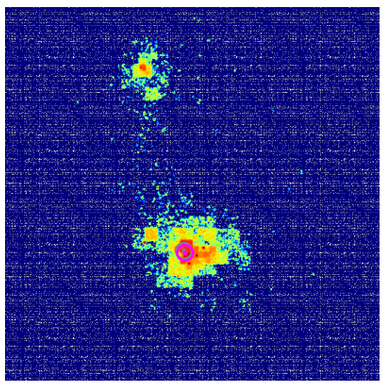

ID=7
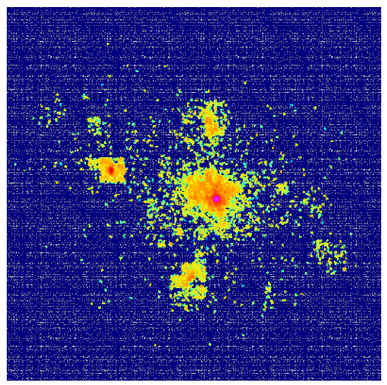

ID=8
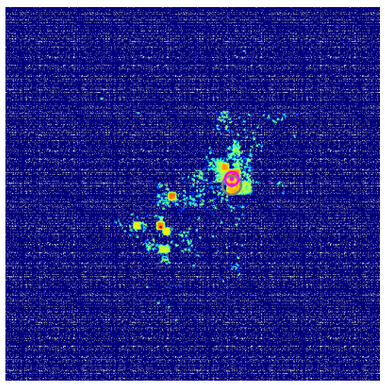

ID=9
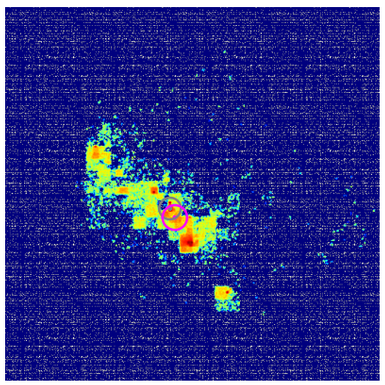

ID=10
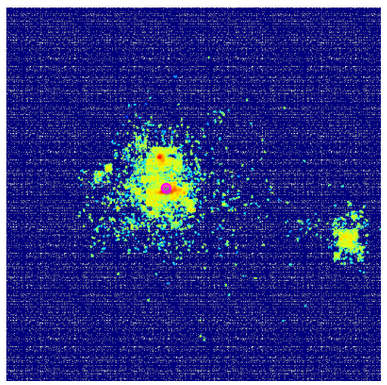

ID=11
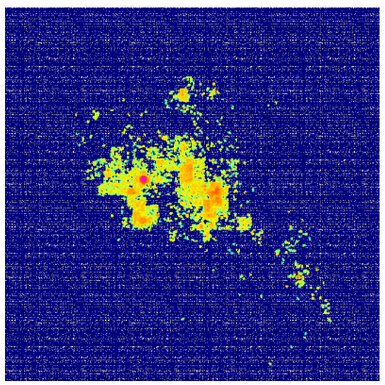

ID=12
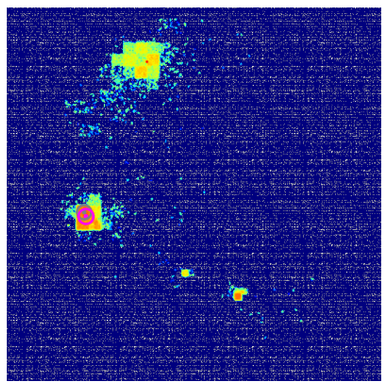

ID=13
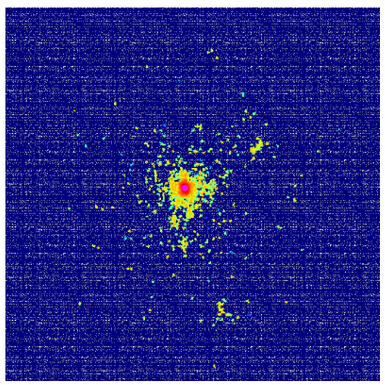

ID=14
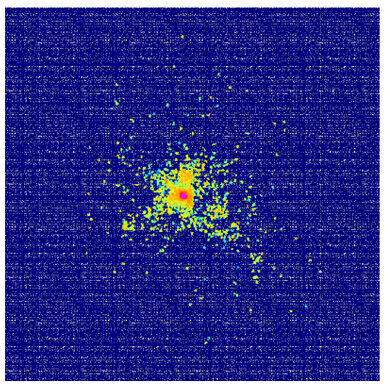

ID=15
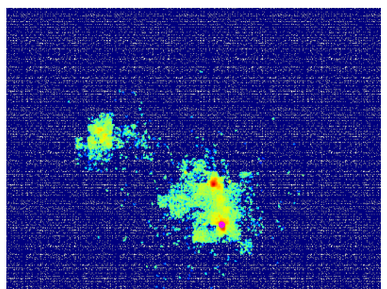

ID=17
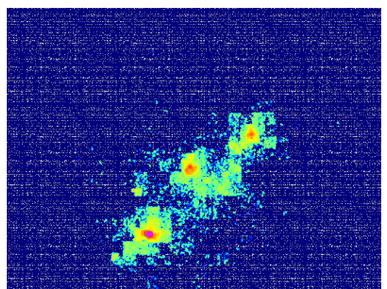

ID=18
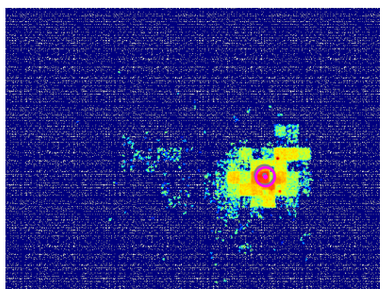

ID=19
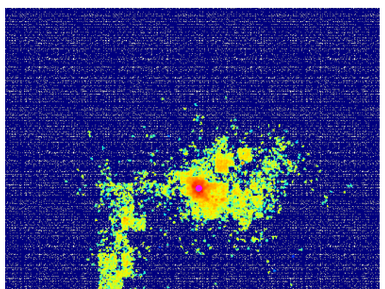

Half-Light Radius (z=8)

Half-Light Radius (z=10)

ID=0

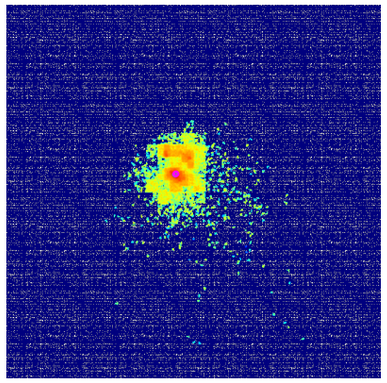

ID=1

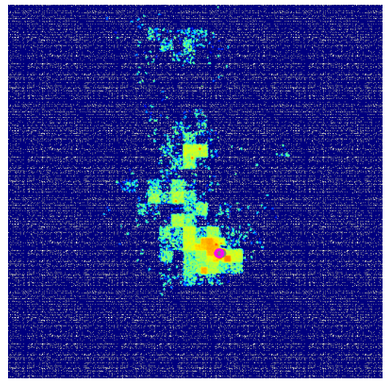

ID=2

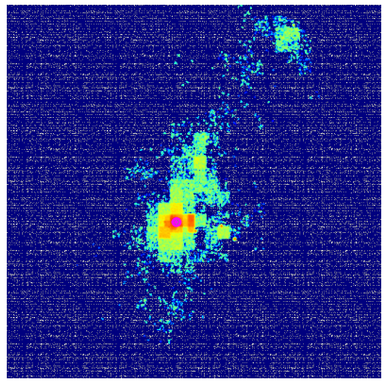

ID=3

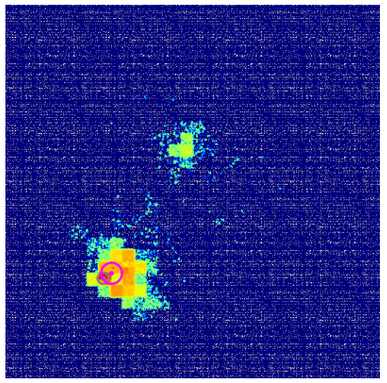

ID=4

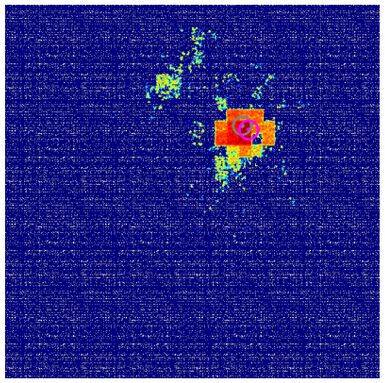

ID=5

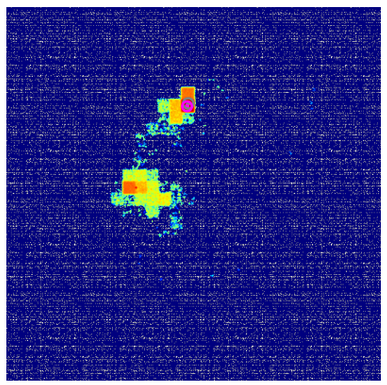

ID=6

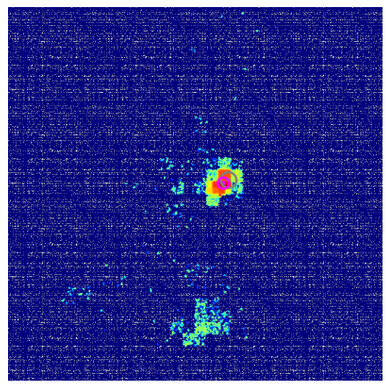

ID=7

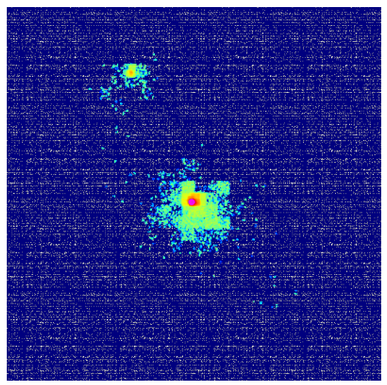

ID=8

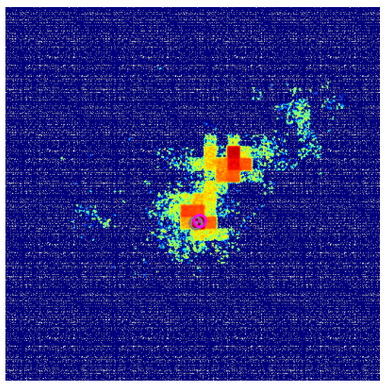

ID=9

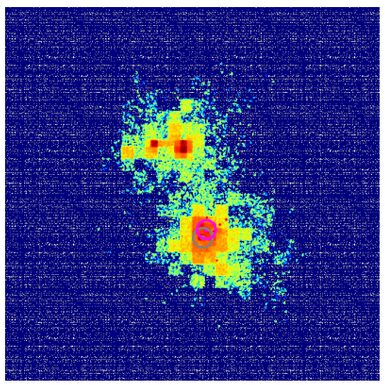

ID=10

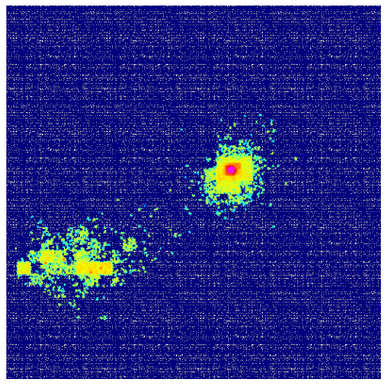

ID=12

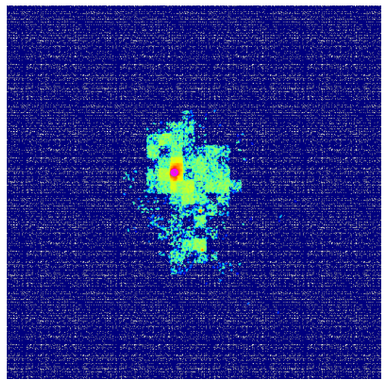

ID=13

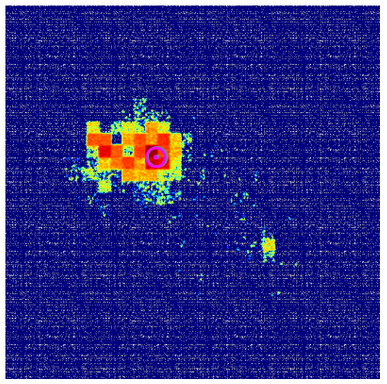

ID=14

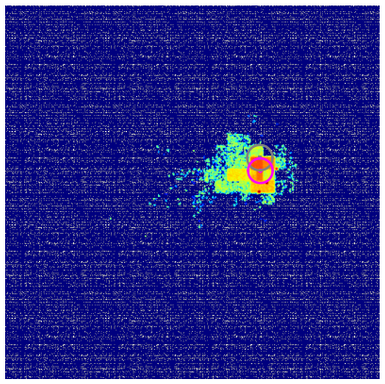

ID=15

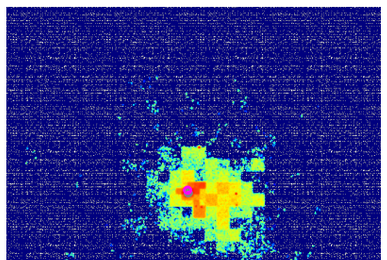

ID=16

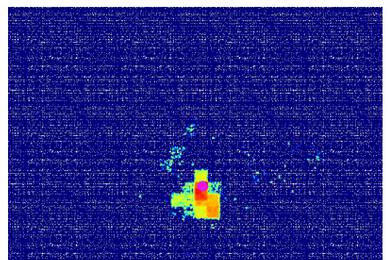

ID=17

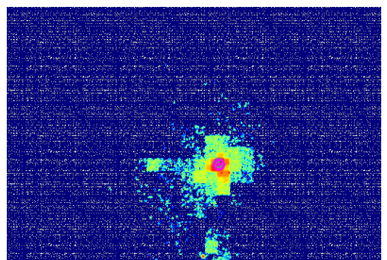

ID=18

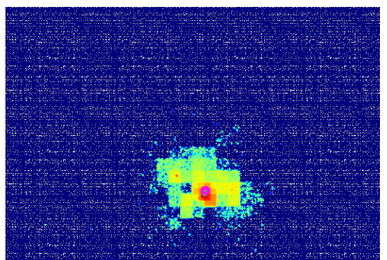

ID=19

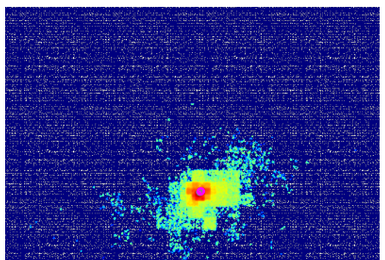

Half-Light Radius (z=12)

ID=0

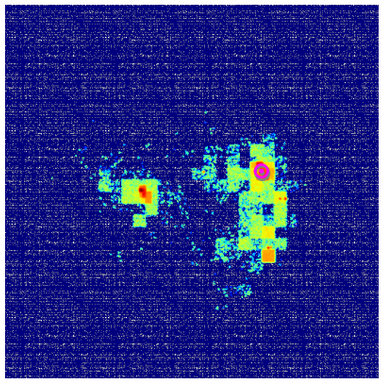

ID=1

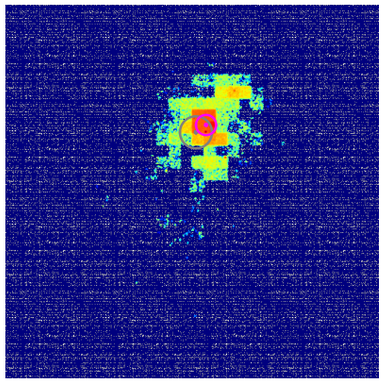

ID=2

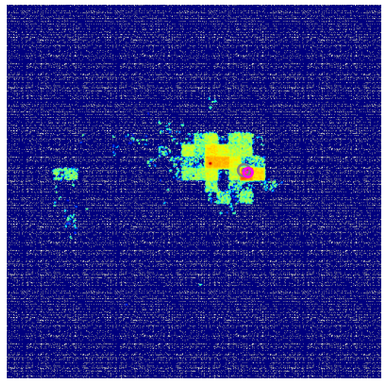

ID=3

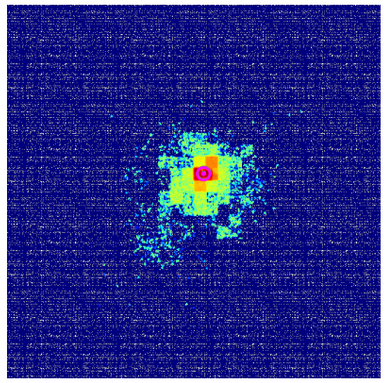

ID=4

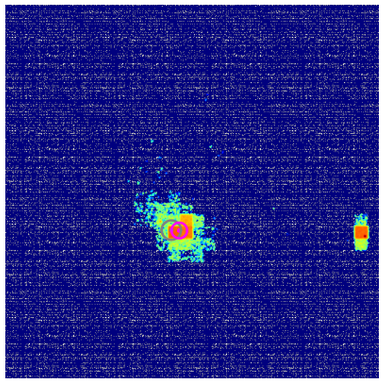

ID=6

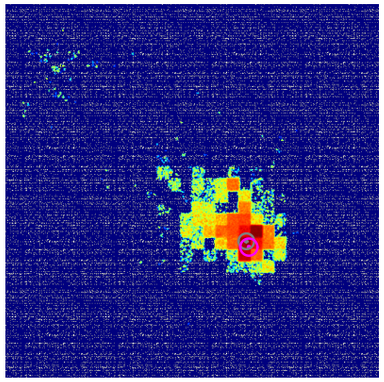

ID=7

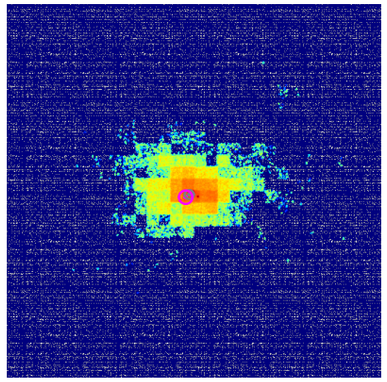

ID=9

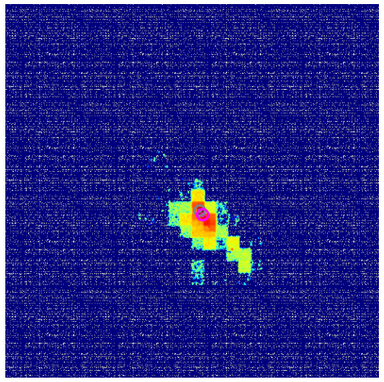

ID=10

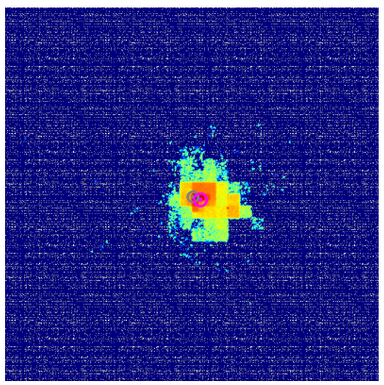

ID=11

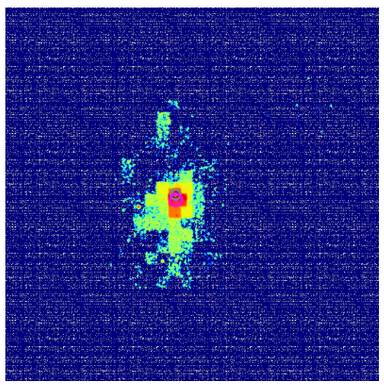

ID=12

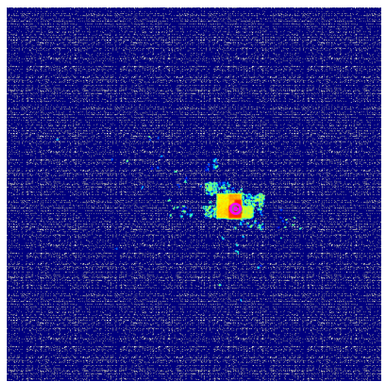

ID=13

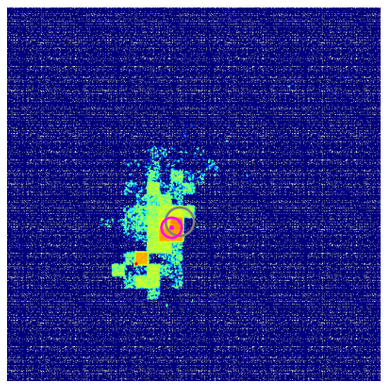

ID=14

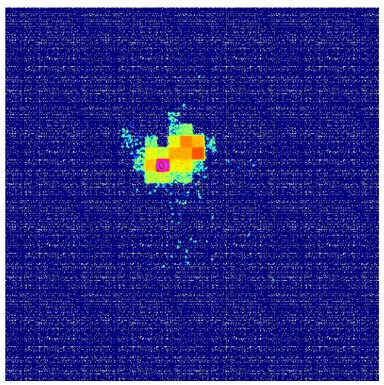

ID=15

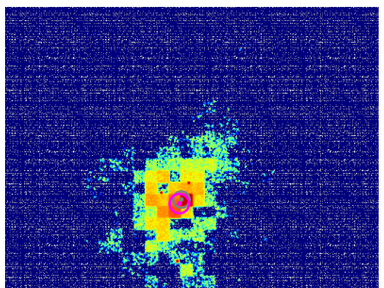

ID=16

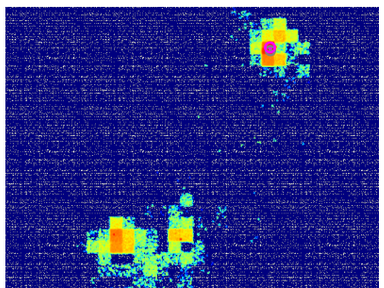

ID=18

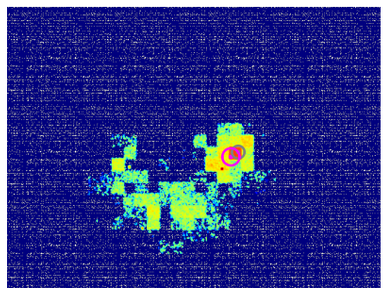

Previous Study

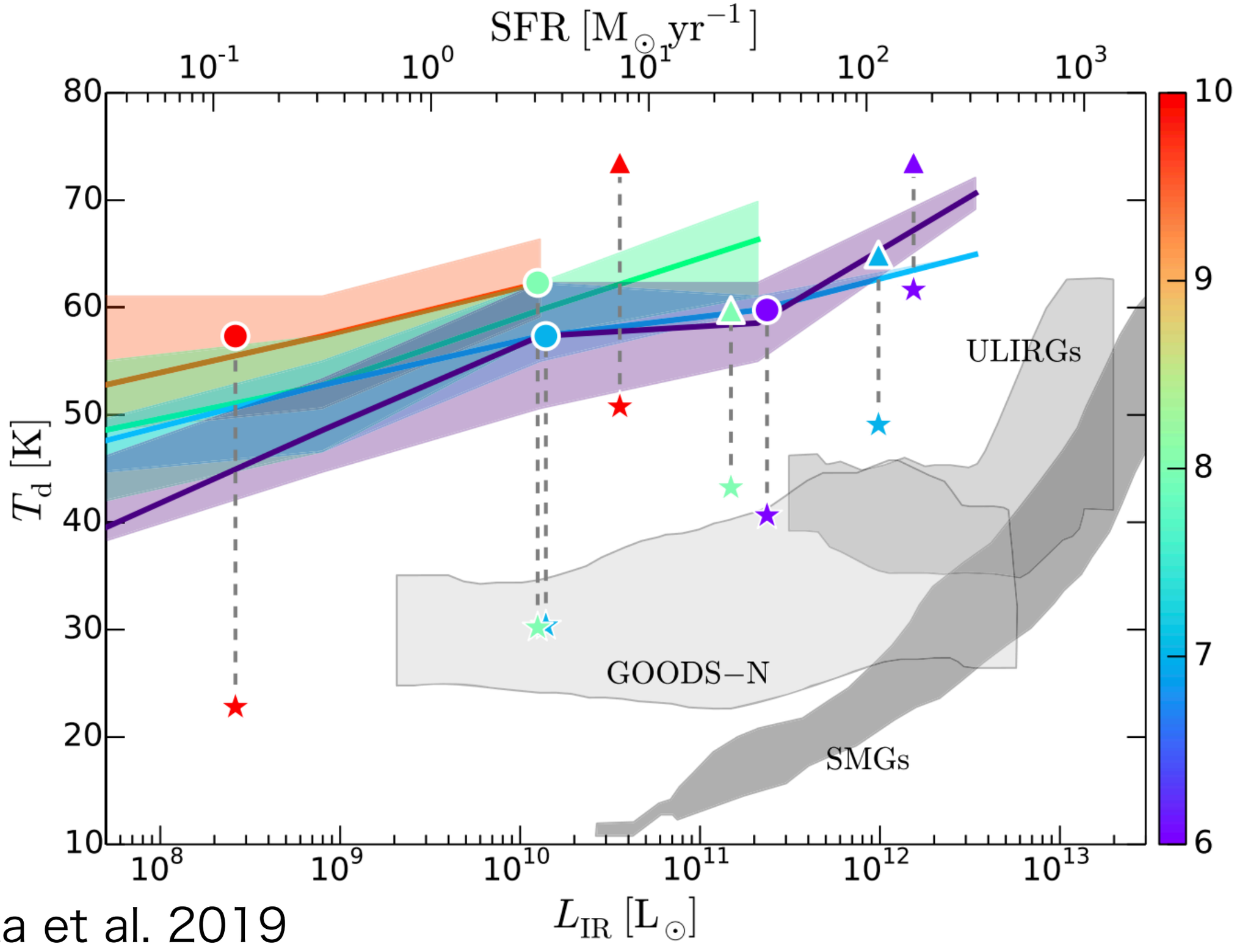

Arata et al. 2019